Investigation of the Global Escarpment, including the Fretted Terrain, in the Martian Northern Hemisphere

by

Benjamin Chad Harrold

A thesis submitted to the Graduate Faculty of
Auburn University
in partial fulfillment of the
requirements for the Degree of
Master of Science

Auburn, Alabama
August 9, 2010

Approved by

David T. King Jr., Co-Chair, Professor of Geology
Luke J. Marzen, Co-Chair, Associate Professor of Geography
Lorraine W. Wolf, Professor of Geology

Abstract

The global escarpment and associated fretted terrain are located in the Martian northern hemisphere. Two competing hypothesis presently in play explain the origin of Mars' global escarpment. These hypotheses involve endogenic and exogenic processes and both could help explain the extreme topographic difference between the southern highlands and the northern lowlands. The focus of this study, the fretted terrain area of the global escarpment, is a transition zone of mesa-like features located directly north of the global escarpment. With the use of digital imagery analysis, georeferencing of existing maps, and the interpretation of current models, the most plausible origin of the escarpment proposed herein would be an exogenic process, namely a single, mega-scale impact shortly after formation of the planet. The main lines of evidence supporting this favored hypothesis are the modeled elliptical shaped basin, similarities between crustal thickness and topographic elevations, mineralogy, and the orientation and size distribution of the northern fretted terrain.

Acknowledgments

The author would like to thank the members of his thesis committee, Drs. David King, Luke Marzen, and Lorraine Wolf for their unequivocal support and guidance during this project. The author is particularly grateful to Dr. King for “originally suggesting this line of inquiry.” The author is also grateful to Dr. Marzen, whose grant proposal and expertise in GIS helped initiate this project.

The author acknowledges the extensive use of multiple publicly accessible imagery databases including Arizona State University <http://www.mars.asu.edu/data/>, NASA <http://mars.jpl.nasa.gov/mgs/sci/mola/mola-may99.html>, Planetary Data System (PDS) <http://pds.jpl.nasa.gov>, U.S.G.S Planetary GIS Web Server http://webgis.wr.usgs.gov/pigwad/maps/index.html, http://www.ian-ko.com/ ET GeoTools for ArcGIS and Google Earth 5.0.

The author would like to dedicate this thesis to his family and friends for their moral and intellectual support over these past two years: “Pops and Mammy, thanks for instilling me with the courage, intelligence, wisdom, and strength to pursue any dream in life. Josh, thank you for always putting a smile on my face and teaching me to be a better sibling. Bart, thanks for the endless quest for patience with computer software. And finally, to my wife Joy, who replanted the seed of discovery and taught me what love, compassion, and unselfishness are all about.”

Table of Contents

List of Tables

List of Figures

INTRODUCTION

The geomorphic evolution of the Martian surface has been an ongoing process since the planet's formation about 4.6 billion years ago. These changes are apparent when the topography is examined. Mars has many striking surface features including some of the highest peaks (e.g., Olympus Mons) and deepest canyons (e.g., Valles Marineris) in the solar system. Another less studied but equally significant feature is the global escarpment located in the northern hemisphere (Fig. 1).

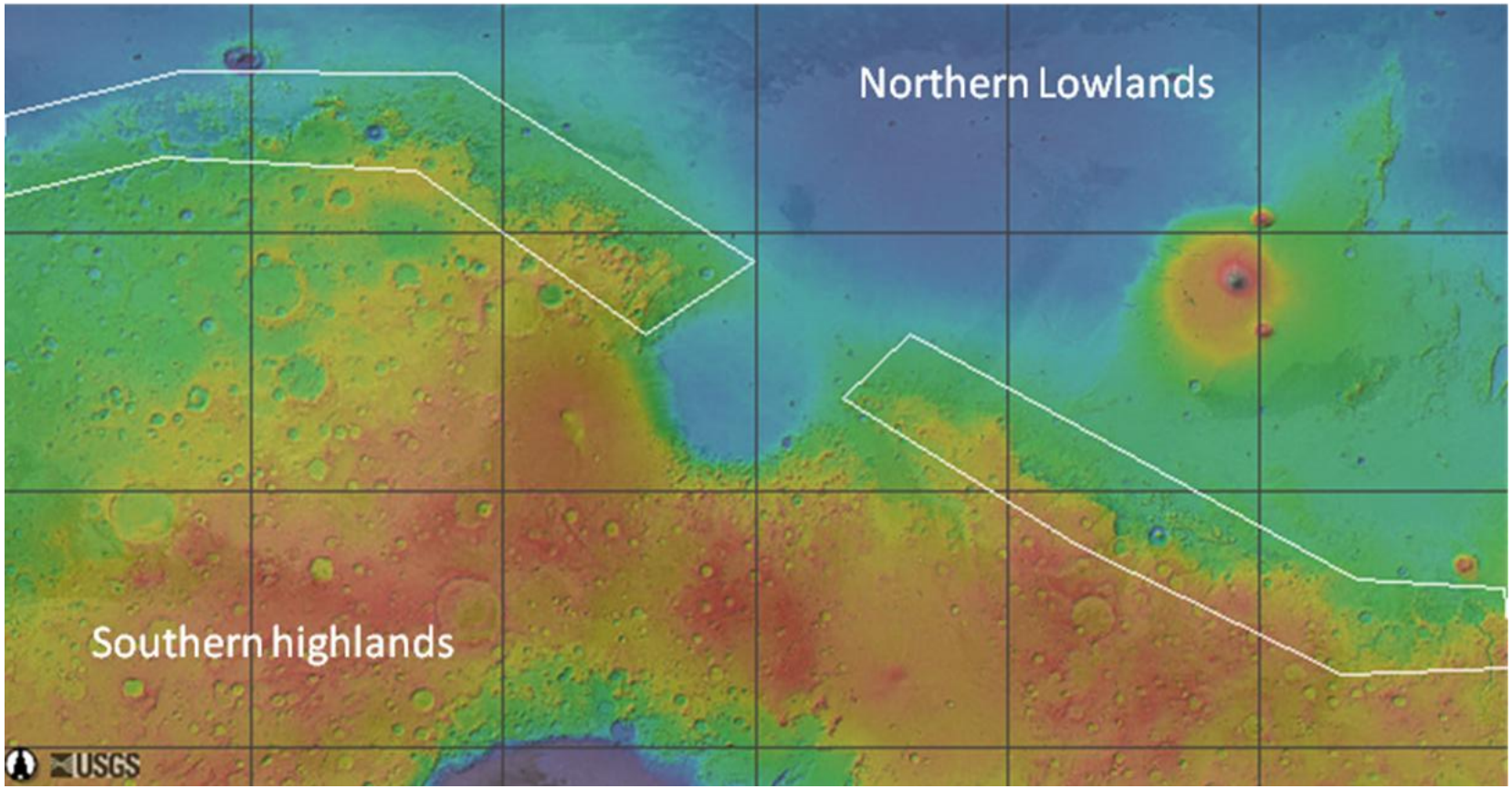

Figure 1. Outlined study area of the global escarpment of Mars. Each quadrangle is 30 x 30 degrees. Modified from http://webgis.wr.usgs.gov/website/mars_html/viewer.htm including the current USGS PIGWAD map, MOLA layer. (Accessed 14 Oct., 2008).

The boundary between the highlands of the southern hemisphere and the lowlands of the northern hemisphere, sometimes referred to as the Martian dichotomy, is marked with elevation changes of up to 1 km in some areas along the global escarpment (Kiefer 2008). The ages of these two regions, south highlands ~4.2 ± 0.8 b.y. and the northern lowlands ~4.12 ± 0.08 b.y., have been estimated by crater density and comparisons to other celestial bodies like the Earth's moon (Tanaka 1986). The approximate age for the global escarpment's formation using these techniques is 4.1 to 3.9 b.y. (Watters 2007).

Past studies have revolved around two major theories for the possible formation of the escarpment: (1) endogenic or internal processes such as mantle convection or plate tectonics (McGill and Squyres 1991); and (2) exogenic or external processes, such as large multiple impacts or a single mega-impact (Wilhelms and Squyres 1984). Both models have strengths and weaknesses and have evolved over the past 30 years with the addition of new information from satellite remote sensing and improvements in technology.

The fretted terrain (Fig. 2) is one of several transitional terrains that can be identified on the Martian surface and is located between the southern highlands and the northern lowlands. The fretted terrain is thought to have a nearly uniform height clustered around 0º elevation with respect to the aeriod comprised of polygon-shaped blocks. It is bounded by an abrupt escarpment in the highlands to the south and transitions into the knobby terrain to the north (Sharp 1973). The initial formation and evolutionary processes of this terrain are poorly understood to present date (Irwin and Watters 2004).

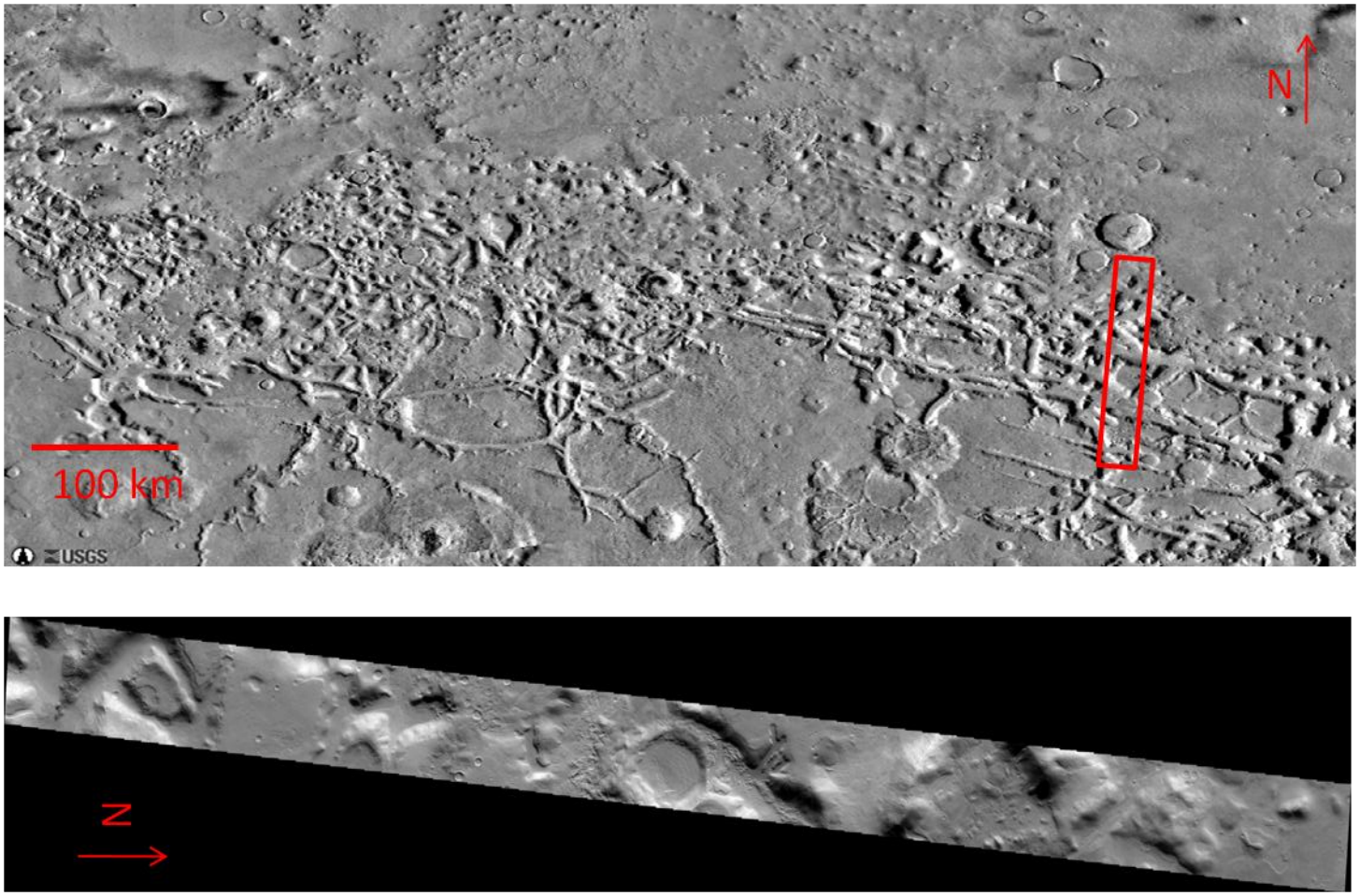

Figure 2. Example of the fretted terrain found in the northern hemisphere on the global escarpment. From http://webgis.wr.usgs.gov/website/mars_html/viewer.htm including the current USGS PIGWAD map, Themis layer. Themis image V11918012 located in red box. (Accessed 14 Oct., 2008).

OBJECTIVES AND SIGNIFICANCE OF STUDY

The objectives of this study are as follows: (1) use new planetary imagery and data products to review existing theories and propose new hypothesis about the formation and evolution of the global escarpment, with emphasis on the fretted terrain; and (2) to integrate findings of this study with existing theories of escarpment and thus provide a better understanding of the origin and evolution of the fretted terrain.

The current efforts at planetary exploration have gained momentum over the past two decades with the addition of new technology and a heightened interest in the scientific community. With publicly accessible imagery and data sets, exploration of Mars is now more readily achievable than ever before. The origin of the global escarpment has many interpretations ranging from exogenic models involving a single impact (Marinova et al. 2008) to multiple impact basins (Frey 1988) to endogenic or internally driven forces, such as mantle convection (McGill and Dimitriou 1990) or plate tectonics (Sleep 1994). The information obtained throughout this project is expected to shed some light in the direction of one or more of these possibilities. Extensively detailed topographic mapping incorporating all of these imagery layers, aspects, and comparisons to past projects has yet to be done on this single geomorphic feature of Mars.

GEOLOGIC HISTORY OF MARS: PHYSICAL AND CHEMICAL

The geologic history of Mars encompasses many violent and chaotic changes throughout its nearly 4.6 billion year life span. Because Mars has been physically and chemically active through time, we can use two types of geomorphic alterations to date surface features on the planet. These two different methods can be used to delineate two separate Martian geologic time scales.

The first and oldest method used to physically date the Martian surface is the impact crater size-frequency method (Nimmo and Tanaka 2005). Using the principles of superposition and the standard Martian crater counting method, Mars has been divided into three major epochs (Fig. 3). The cratering rate of Mars has been estimated primarily by lunar comparisons, which was adjusted for the population of Mars-crossing asteroids (Hartmann and Neukum 2001). A few issues must be considered while using the Martian crater count method.

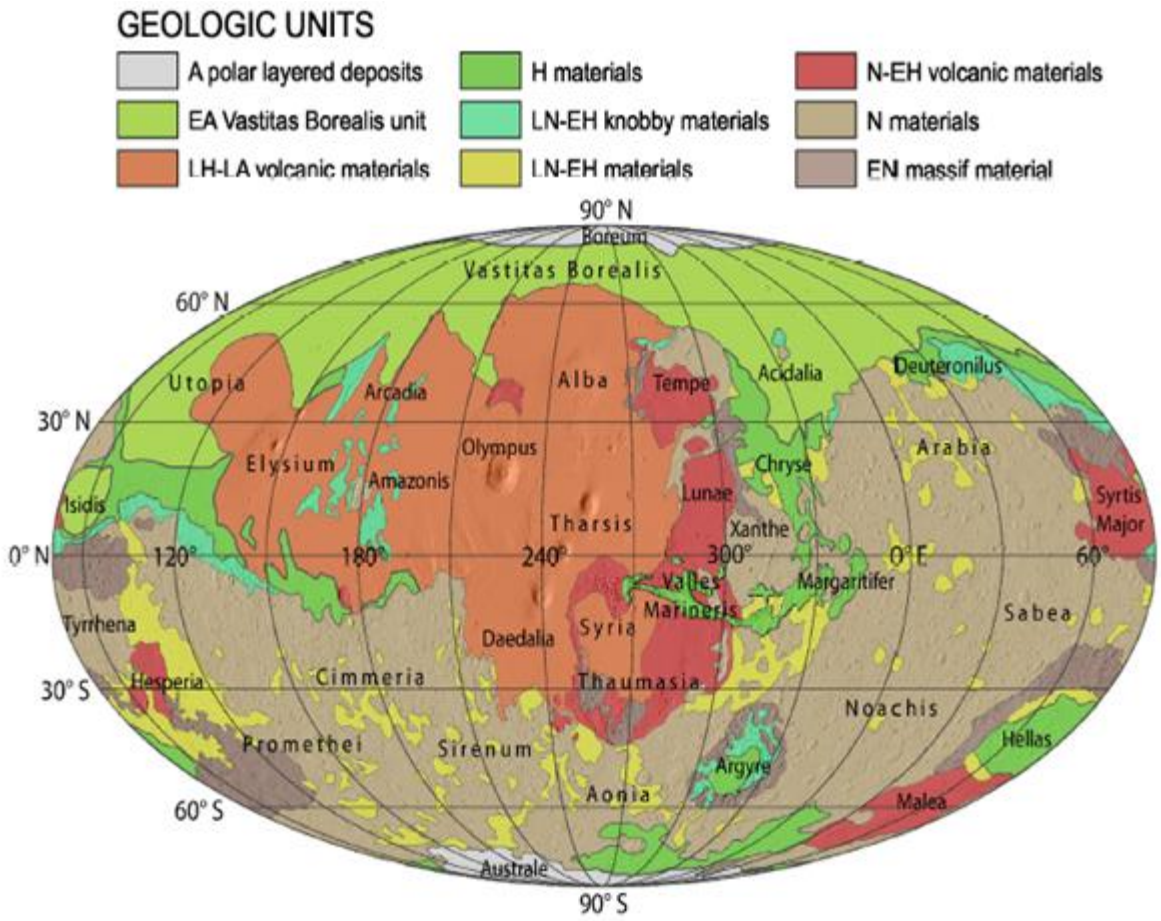

Figure 3. Generalized geologic map of Mars showing the distribution of major material types as described in the text. Unit age abbreviation: N, Noachian; H, Hesperian; A, Amazonian; E, Early; L, Late .This is a Mollweide projection, centered on 260°E. Data are from Mars Orbiter Laser Altimeter (MOLA) using shaded relief on Mars, 1° latitude = 59 km. Adapted from Scott et al. (1986-1987) and Tanaka (2003).

First is the total crater density, which is measured by statistically fitting the crater count data including size distribution to known size frequency functions over varying ranges of crater diameters (Hartmann and Neukum 2001). The use of large diameter craters means that large areas must also be covered, which could visually constrain the limit of smaller geologic units. Lastly, the crater retention age, or the average time interval for which a specified size crater will be preserved on the surface are biased toward the younger end of the newly classified geologic unit. These factors can then be incorporated to give an overall uncertainty factor of 1.2 to 1.3, and suggest a percent error between 5 to 20% (Hartmann et al. 1981). Because Mars is nearly 4.6 billion years old, ages derived for the crater counting technique could vary by 200 million to 1 billion years. Still these crater-density ratios provide relative ages for subdividing Mars into specific geologic units and enables comparison of differing geomorphic processes throughout Martian history. Using these techniques, a geologic map was produced by David Scott and Michael Carr in 1978 (Fig. 4). This map encompasses 24 Martian-rock stratigraphic units subdivided into five general categories: (1) plains material; (2) constructional volcanic material; (3) channel and canyon material; (4) rough terrain material; and (5) polar material.

Figure 4. Geologic Map of Mars derived by crater density ratios. From Scott and Carr (1978).

The three major eras of Martian geologic physical history using the crater size-frequency method are the Noachian Epoch (4.6 to 3.5 b.y.), the Hesperian Epoch (3.5 to 1.8 b.y.), and the Amazonian Epoch (1.8 b.y. to the present). These names are taken from the corresponding geographic regions of Mars.

Another more recent time scale which involves the surface mineralogy has been proposed based on new data from OMEGA Visible and Infrared Mineralogical Mapping Spectrometer on board the Mars Express Orbiter. Using spectral analysis of Martian mineralogy, Mars' history is divided into 3 different major epochs. These are the Phyllocian Epoch (4.6 to 4.0 b.y.), the Theiikian Epoch (4.0 to 3.5 b.y.), and the Siderikan Epoch (3.5 b.y. to the present (Gangle 2007); Fig. 5). This series divides the Noachian into two epochs depending on water availability and chemical alterations of the corresponding surface minerals that were present at that time.

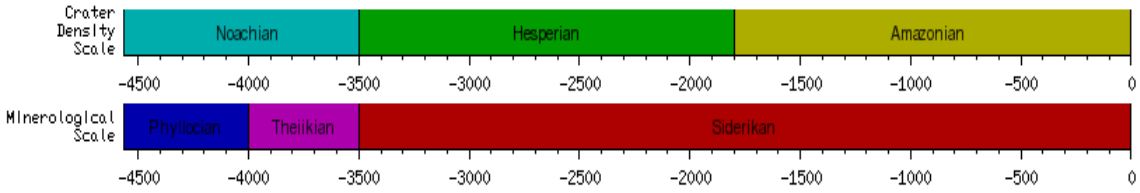

Figure 5. Geologic time scales of Mars using crater density and mineralogy. Modified from Gangale (2007).

Physical History: The Noachian Epoch (4.5 to 3.5 b.y.)

The first epoch of Martian history, sometimes referred to as the heavy bombardment era, is the Noachian. This name comes from the Noachis quadrangle where the oldest rocks on the planet are exposed (Scott and Carr 1978). The Noachian began with the initial formation of the planet from the proto-planetary disk. As Mars grew in

size, it was bombarded with planetesimals. The continued impacts from these asteroid-like bodies caused some surface regions of Mars to become heated or partially melted (Lenardic et al. 2004). Planetary heating was enhanced further by radiogenic heat produced internally.

Crust formation predates the end of the heavy bombardment era. Rock units from this epoch represent highly brecciated and faulted crustal rocks, evidence of which can be seen in many large multi-ring basins such as Hellas and Argyre (Scott and Carr 1978). The surface continued to be bombarded by the remnants of planetary material available, which caused a great deal of heating near the surface of Mars. A period of wide spread lava flooding is represented by the extensive tracts of plains between these two ancient craters (Christiansen 1995). These voluminous flood basalts were extruded from fissures, but were relatively thin (Scott and Carr 1978). Due to the constant bombardment, these lava plains and impact ejecta comprise an overlapping and interbedded geologic unit known as the cratered plateau material (Scott and Carr 1978). This planet wide heating event which entailed the release of large amounts of volatiles from volcanic edifices was accompanied by planetary hydrothermal activity or circulation of water possibly melting large amounts of permafrost that was present in the ground (Baker 2001). The early Martian atmosphere was likely more dense and atmospheric temperatures were likely higher. In view of these conditions, potential rainfall and flooding would have caused sufficient erosion and sediment transportation for large quantities of sediment to have accumulated in highland basins as well as the northern lowlands (Christiansen 1995).

Physical History: The Hesperian Epoch (3.5 to 1.8 b.y.)

The Hesperian is named for the Hesperia Planum in the Mare Tyrrhenum quadrangle and is split into three rock units: (1) rolling ridge material; (2) ridge plain material; and (3) streaked plain material (Scott and Carr 1978). The second epoch in Martian history began at the end of the heavy bombardment and was marked by the formation of extensive interlayered lava plains and eolian deposits. Later during this epoch, there was a period of heating and volcanic activity, caused by a hot plume of material that continued to rise from deep within the interior of Mars toward the Tharsis Bulge located in the northern hemisphere (McGovern et al. 2002)**.** The crust was then deformed by the extensional pull from this magma and created the Tharsis Montes, Olympus Mons, and the other volcanoes accompanied with radial fracturing (McGovern et al. 2002)**.** The northern hemisphere may have been extensively fractured during this era due to its thinner crust. The volcanoes and fissures spread lava over the lowlands of Mars and created a new surface, which shows less meteorite bombardment than do the older highlands (Frey 2006). Valles Marineris began to develop along this fracture system, followed by intense runoff evident from the channels produced from the highlands to lowlands (Tseung and Soare 2006). These were the first wide spread flooding events to take place on the Martian surface due to melting of ground ice by volcanism, meteor impacts, or climate change. At this time, the northern plains were resurfaced by sedimentation (Phillips et al. 2001). Later, the surface temperatures began to lower as Mars quickly cooled due to its relative size. Atmospheric pressure dropped due to erosional processes associated with constant solar bombardment, then making it unlikely for water to continue to exist on the surface. Consequently, water became

trapped as permafrost in the Martian soil and volcanism again caused huge amounts to melt and flood the low-lying areas. Much of the erosion that occurred along the global escarpment is attributed to this process (Christiansen 1995). At the end of the epoch, Elysium began to erupt along with highland volcanic centers and the creation of the Tharsis volcanoes began to develop (Scott and Carr 1978).

Physical History: The Amazonian Epoch (1.8 b.y. to present)

The Amazonian, named for the Amazonis quadrangle is Mars' final epoch and extends to the present day (Scott and Carr 1978). Ground surfaces of Amazonian age have a few meteorite impact craters, but otherwise are quite varied constituting volcanic material, alluvium, and eolian deposits. The Amazonian Epoch has seen localized lava flows around the huge volcano Olympus Mons and other volcanoes increase in size. Elsewhere on Mars, landslides formed along the rim of Valles Marineris and along the global escarpment with continued sediment transportation (Baratoux et al. 2002). Catastrophic outbreaks of ground water due to the Tharsis rise produced floods and formed the Chaotic terrain, which are located at the eastern end of Valles Marineris. These flood events transported sediment to the northern basin and produced short-lived seas. The Chaotic terrain was enlarged and the Global escarpment continued its southerly retreat (Christiansen 1995). Eolian processes continued to change the surface of the planet to the present day smoothing the overall appearance of Mars. The thickness of these deposits varies greatly ranging from thin sheets to thick accumulations that sometimes bury craters to depths of a few kilometers (Scott and Carr 1978).

Chemical History: The Phyllocian Epoch (4.6 to 4.0 b.y.)

The first chemical/alternative Epoch of Martian history is the Phyllocian. This epoch receives it name for the abundance of phyllosilicates that were formed during the first 500 million years of Martian existence. These clay-rich minerals, which include Fe-rich (chamosite and nontronite) and Al-rich (montmorillonite), require an alkaline-rich water environment in which to form (Bibring et al. 2006). These conditions would not require high temperatures and would indicate extensively wet periods with alkaline waters resulting from chemical alteration. Thus, we can deduce that - during this epoch - Mars must have had liquid water present at or near the surface early in its evolutionary process (Fig. 6). Clay minerals may have also been formed in the subsurface by three processes: (1) hydrothermal activity; (2) cratering, that supplied subsurface water to the impacted material; or (3) mantle cooling (Bibring et al. 2006).

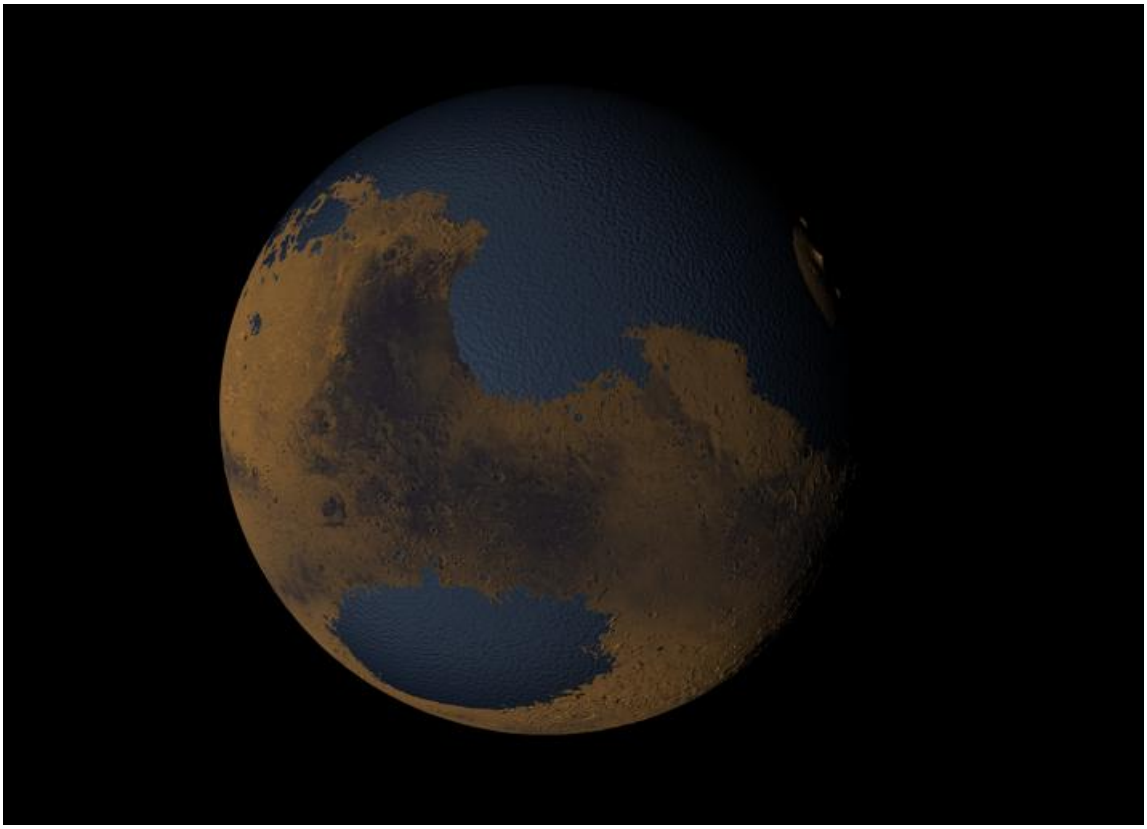

Figure 6. Artistic rendition of a possible wet Mars from the past. From http://svs.gsfc.nasa.gov/vis/a000000/a002200/a002291/index.html (Accessed on 7 Feb., 2010; NASA 2010c /Goddard Space Flight Center Scientific Visualization Studio).

Chemical History: The Theiikian Epoch (4.0 to 3.5 b.y.)

The Theiikian Epoch is dominated by the presence of sulfate minerals. Because Mars was extremely active volcanically during this period, huge quantities of sulfur dioxide along with other volatiles were expelled into the atmosphere. These volatiles precipitated and then mixed with surface waters that were either still present or part of a replenishment process on the Martian surface. Sulfate mineral formation requires considerable amounts of water to be present and then evaporate confining it to a surface process (Bibring et al. 2006).

Chemical History: The Siderikian Epoch (3.5 b.y. to present)

The final alternative epoch is the first one in which water does not play any sustainable role. This can be found in the lack of hydration of the ferric oxides in comparison to hydrated phyllosilicates and sulfates. The atmosphere and water have disappeared along with a waning of volcanism and global cooling. Ferric oxides formed as an alteration product resulting from atmospheric weathering through peroxide reactivity (Bibring et al. 2006).

BULK COMPOSITION OF MARS

The knowledge of the bulk properties of a planet can lend us invaluable information about the interior of a planet. These properties include mass, size, density, composition, and moment of inertia. If we begin by using the mass, size, and shape of the planet, we are able to calculate the bulk density and moment of inertia. The bulk composition can be estimated from the bulk density and using the moment of inertia we can determine if that planet were able to differentiate into layers (Bertka and Fei 1998). Since 1997, when the Mars Global Survey arrived at Mars, researchers have used one of its five instruments (Mars Orbital Laser Altimeter) to gain accurate measurements (~460 m horizontally and ~1 m vertically) of the topography. Using these data, an equatorial diameter of 6,792.19 km and a polar diameter of 6,752.4 km have been determined and in addition a mass of 6.44×10^{23} kg and total bulk density of 3.906 g/cm^3 have been computed (Cattermole 2001). This mass can also be calculated by the gravitational interaction between Mars and the orbital paths of Phobos and Deimos and also by Mars' effect on past satellite flybys and more recent orbiters. In comparison to the other terrestrial planets, Mercury (5.44 g/cm^3), Venus (5.25 g/cm^3), and Earth (5.52 g/cm^3), this bulk density is relatively low. The lower density can be attributed to the initial conditions during formation of the planet. Specifically, the nebular condensation model would predict that light volatiles like water would be sufficiently incorporated farther from the sun (Christiansen 1995). Early in the planetary accretion process, metallic iron mixed

with primordial water producing iron oxides via chemical reactions, which were incorporated into the interior of Mars. The other terrestrial planets with higher mean densities located closer to the sun did not readily blend the iron and water; hence they have appreciably less iron oxide that Mars (Boyce 2002).With the data acquired from the mass, size, and shape, we can now calculate the moment of inertia. This indicates whether a planet has separated into layers, and for Mars we find that it is similar to Earth i.e., it possesses a core, mantle, and crust. Even though the presence of layers can be determined through this process, unfortunately a thickness for each layer cannot. The composition of a planet is also a useful property and can be obtained from rock samples. Presently, we have samples of Martian rocks in the form of meteorites. These SNC meteorites (named after the three types of igneous meteorites-shergottites, nakhlites, and chassigny) are pieces of the Martian crust blasted off the surface by large impactors (Table 1). Pockets of gases trapped in the glasses within these meteorites are chemically consistent with what we know of Mars' atmosphere. For example, gases analyzed from the shergottite meteorite chemically and isotopically match those currently found in the Martian atmosphere lending evidence that they indeed came from the red planet (Bogard et al. 1984).

Table 1. Calculated bulk composition for Mars using three different sources. Modified from Boyce (2002).

Constituents	Composition Similar to Chondritic Meteorites (%)	Composition Calculated from SNC Composition (%)	Terrestrial Mantle and Crust (%)
Mantle and Crust			
SiO_2	41.6	44.4	45.1
TiO_2	0.3	0.1	0.2
Al_2O_3	6.4	3	4
Cr_2O_3	0.6	0.8	0.5
MgO	29.8	30.2	38.3
FeO	15.8	17.9	7.8
MnO	0.15	0.5	0.1
CaO	5.2	2.4	3.5
Na_2O	0.1	0.5	0.3
H_2O	0.001	0.004	
K (ppm)	59	305	260
Core			
Fe	88.1	77.8	
Ni	8	8	
S	3.5	14.2	
Calculated relative mass			
Mantle plus crust	81	78.3	
Core	19	21.7	

SNC (Shergottites, Nakhlites, and Chassigny meteorites)

Because SNC meteorites are relatively young, they may not represent well, the chemistry of the ancient Martian crust. With this age discrepancy of ancient highland rocks tested by Pathfinder and more modern SNC meteorites, a distribution difference can be seen. Comparing different data sets from the GRS (gamma ray spectrometer), TES (thermal emission spectrometer), Martian meteorites, and rover missions, a ($Na_2O + K_2O$) vs. SiO_2 diagram of Martian rock and dust can be composed (Fig. 7).

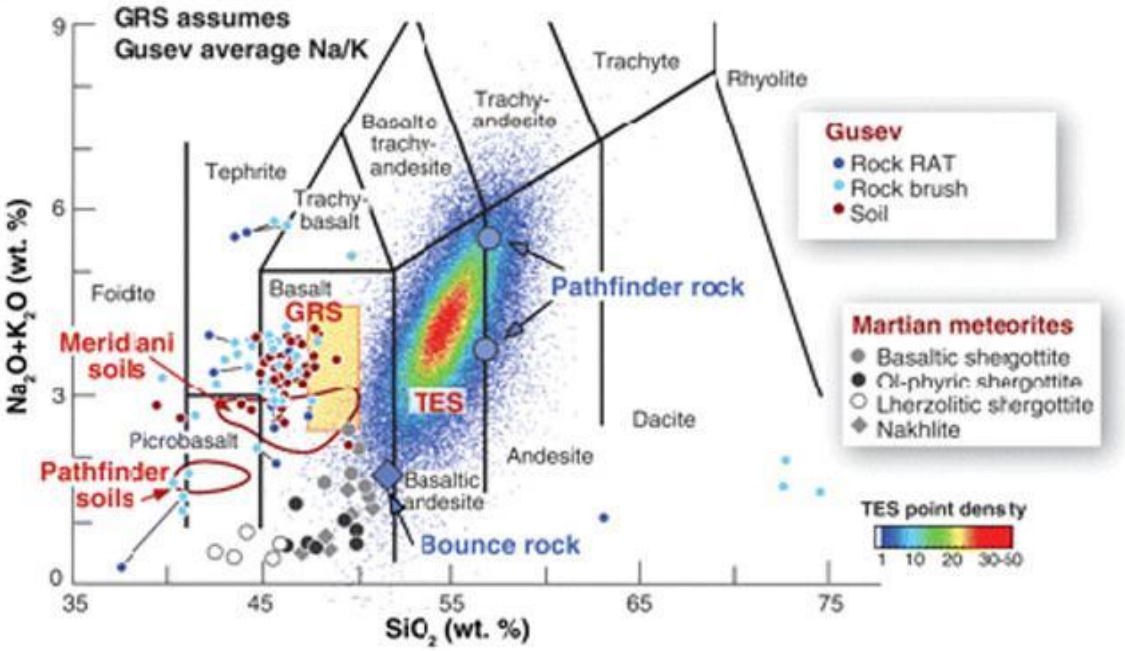

Figure 7. Diagram composed of several meteorites along with multiple orbital and lander missions assessing the Martian regolith. From Bell (2008).

The Core

The core of Mars is the key to understanding all the processes that follow the initial formation of the planet after accretion. Because we have no seismic equipment on the surface to obtain a more accurate thickness, the use of two extremes of density is necessary to bracket a size and mineralogy. The first density extreme is a core composed mainly of iron, but also rich in oxygen and sulfur. Mars' core has a radius of 2,200 km and has a bulk density of 6 g/cm^3. The other density extreme is a mixture of iron-nickel alloy with a radius of 1,300 km and a bulk density equal to 8 g/cm^3 (Boyce 2002). Analysis from the Pathfinder mission had similar results of between 1,300 and 2,000 km for the core radius (Golombek et al. 1999). The sulfur content of the core is the defining characteristic of whether a planet can generate a magnetic field and how long that field

will last. The presence of sulfur lowers the freezing point of iron below the convection temperature needed to sustain a dynamo (Stevenson 2003). If the core of Mars were to contain >15% sulfur, then the magnetic field would be present to this day due to the persisting activity of the dynamo (Boyce 2002). Again with the use of the Mars Global Surveyor instruments (a magnetometer and electron reflector), scientists found this was not the case for Mars. There are large regions of lava flows without magnetic orientation dating to ~3 to 4 b.y., thus reiterating that the Martian dynamo ceased early in Martian history. For this to be the case, a comparison of the SNC meteorites yields a core of mostly iron, 7-8% nickel and about14% sulfur (Sohl and Spohn 1997). This amount of sulfur would allow for a partially molten core to last for approximately 1 billion years. The cause of the relatively fast core cooling is attributed to the size of Mars. The core reached a stage where conduction and not convection became the dominant source of heat flow (Williams and Nimmo 2004). At this time, the dynamo would have ceased to function and no remnant magnetism could be left behind in the geologic record.

The Mantle

The thickness of the Martian mantle is directly related to the size of the core. For example, a larger core would require a thinner, less dense mantle contrasting with a smaller core having a thicker, denser mantle. With a range in core size and density, the mantle thickness can only be narrowed to a window of 1,500 to 2,100 km and an average density of 3.41 to 3.52 g/cm^3. This is considerably higher than the 3.31 g/cm^3 average for the mantle of the Earth (Boyce 2002). The higher density is thought to correspond with the amount of iron oxide present in the mantle. The crystalline structure of rocks can be altered with the addition of heat and pressure. Therefore, it is not uncommon for layers to

have the identical chemistry, but due to increasing pressure a different more compact crystalline lattice is formed. Lab experiments show that conditions like those below 1,600 km, the Martian mantle would produce high-density iron rich minerals like majorite and spinel (Bertka and Fei 1998). With a core larger than 1,600 km, the inner most layer of the mantle could not exist. Above the 1,600 km depth, majorite and spinel would transform into other minerals with equivalent compositions with lower density and greater volume. Breuer et al. (1996) use mineralogy to explain Mars' long-term volcanism. At 1,600 km, the transition of olivine to β-spinel and β-spinel to γ-spinel could generate a few strong super plumes in the Martian past, which can be seen on the surface today (Williams and Nimmo 2004). Because the upper mantle is the source for most magma, the composition of volcanic rock should be the same as that of the upper mantle. Without the effects of plate tectonics, a process apparently absent on Mars, the crust and upper mantle cannot be recycled as they are on Earth. As a result, the melts located in the upper mantle grow progressively denser due to igneous differentiation. Through this process, the density of the upper and lower mantle becomes homogenous (Halliday et al. 2004)). Other geologic land features found on the surface provide insight to the makeup of the upper mantle as well. Numerous shield volcanoes such as Olympus Mons, Tharsis Montes, and Elysium Mons can cover thousands of kilometers at their bases. These low viscosity flows reflect the high-iron, low-silicon composition of their upper mantle source.

The Crust and Soil

The uppermost and most familiar layer of Mars is the crust. Due to differentiation and lower temperatures, the crust is the least dense of the three main layers and is relatively rigid. Isotropic signatures from SNC meteorites lend to a mixture of basaltic and granitic rock (Jagoutz 1989).

If the dust samples examined by using a X-ray fluorescence spectrometer on the Viking 1 (1976) and an alpha proton X-ray spectrometer on Pathfinder Sojourner (1997), represented the broad average of upper crust composition, then basaltic, volcanic rock and evaporated salts reign over the landscape (Rieder et al. 1997). Visual evidence from the Viking sites 1 and 2 suggests iron and magnesium rich basaltic rock. The composition of the fine grained drift soil samples did correspond with the low SiO_2 (44.1 to 47.0%) and elevated iron Fe_2O_3 (18.3 to 20.1%) of mafic igneous rock, but low CaO (5.6 to 6.4%) and extremely low Al_2O_3 (7.3 to 8.4%) are not typical of terrestrial mafic volcanics (Cattermole 2001). The suggestion that the soils may be a mixture of Fe-rich smectite clay, carbonates, and sulfates would be typical weathering of volcanic glasses (Toulmin et al. 1977). Rocks analyzed using the 1997 Pathfinder's IMP (Imager for Mars Pathfinder) spectral analyzer yielded mixed results. Compositions varied from conglomeritic sedimentary deposits to columnar basalt or andesitic structures. Four spectral classes were devised: (1) ***grey***- reflective peak at 750 nm consistent with weakly weathered Fe^{2+} rocks; (2) ***red***- high reflectance at short wavelength, but comparable 750 nm for long wavelengths and contain more ferric minerals than grey rocks; (3) ***pink***- high reflectivity at all wavelengths 750 – 800 nm and are identified by encrusted drifts; and (4) ***maroon***- compared to pink rocks, they are darker in all wavelengths peaking at 800 nm

and originate from ferric-rich coatings (Cattermole 2001). In 1997, five rocks were tested by Pathfinder for composition and compared to a sulfur-free rock. Pathfinder's results indicate andesitic basalt, rich in silicon and aluminum (Table 2).

Table 2. Analysis of weight % of five rocks from the Pathfinder Lander Site. From Cattermole (2001).

Rock	A-3 Barnacle Bill	A-7 Yogi	A-16 Wedge	A-17 Shark	A-18 Half Dome	Sulfur-free rock
Na_2O	3.2 ± 1.3	1.7 ± 0.7	3.1 ± 1.2	2.0 ± 0.8	2.4 ± 1.0	2.6 ± 1.5
MgO	3.0 ± 0.5	5.9 ± 0.9	4.9 ± 0.7	3.0 ± 0.5	4.9 ± 0.7	2.0 ± 0.7
Al_2O_3	10.8 ± 1.1	9.1 ± 0.9	10.0 ± 1.0	9.9 ± 1.0	10.6 ± 1.1	10.6 ± 0.7
SiO_2	58.6 ± 2.9	55.5 ± 2.8	52.2 ± 2.6	61.2 ± 3.1	55.3 ± 2.8	62.0 ± 2.7
SO_3	2.2 ± 0.4	3.9 ± 0.8	2.8 ± 0.6	0.7 ± 0.3	2.6 ± 0.5	0
Cl	0.5 ± 0.1	0.6 ± 0.2	0.5 ± 0.2	0.3 ± 0.2	0.6 ± 0.2	0.2 ± 0.2
K_2O	0.7 ± 0.1	0.5 ± 0.1	0.7 ± 0.1	0.5 ± 0.1	0.8 ± 0.1	0.7 ± 0.2
CaO	5.3 ± 0.8	6.6 ± 1.0	7.4 ± 1.1	7.8 ± 1.2	6.0 ± 0.9	7.3 ± 1.1
TiO_2	0.8 ± 0.2	0.9 ± 0.1	1.0 ± 0.1	0.7 ± 0.1	0.9 ± 0.1	0.7 ± 0.1
FeO	12.9 ± 1.3	13.1 ± 1.3	15.4 ± 1.5	11.9 ± 1.2	13.9 ± 1.4	12.0 ± 1.3
OS	92.7	85.9	97.1	88.3	92.6	

Key: OS=Original sum of oxides prior to normalization. All iron is reported as FeO. Calculated weight % norm assumes a molar Fe_3O_2/FeO ratio of 0.026 (Avg. Shergottite value McSween and Jarosewich 1983).

During 1997, soil samples were also studied by instruments on Pathfinder Sojourner. Using 15 geological filters at 12 wavelengths, these soils were classified into 4 distinct spectral classes: (1) ***dark soil*** - dune forms and is the lowest reflective material; (2) ***bright soil*** - shallow aeolian deposits characterized by oxidized ferric rich material; (3) ***lamb-like soil*** - occurs near "lamb rock;" and (4) ***disturbed soil*** - created by rover tracts (Cattermole 2001). By using three different modes, alpha, proton, and x-ray, a high degree of accuracy could be obtained (Table 3).

Table 3. Chemical composition in weight % of six soils from Pathfinder landing site. From Cattermole (2001).

Soil	A-2	A-4	A-5	A-8	A-10	A-15
Na_2O	2.3 ± 0.9	3.8 ± 1.5	2.8 ± 1.1	2.0 ± 0.8	1.5 ± 0.6	1.3 ± 0.7
MgO	7.9 ± 1.2	8.3 ± 1.2	7.5 ± 1.1	7.1 ± 1.1	7.9 ± 1.2	7.3 ± 1.1
Al_2O_3	7.4 ± 0.7	9.1 ± 0.9	8.7 ± 0.9	9.1 ± 0.9	8.3 ± 0.8	8.4 ± 0.8
SiO_2	51.0 ± 2.5	48.0 ± 2.4	47.9 ± 2.4	51.6 ± 2.6	48.2 ± 2.4	50.2 ± 2.5
SO_3	4.0 ± 0.8	6.5 ± 1.3	5.6 ± 1.1	5.3 ± 1.1	6.2 ± 1.2	5.2 ± 1.0
Cl	0.5 ± 0.1	0.6 ± 0.2	0.6 ± 0.2	0.7 ± 0.2	0.7 ± 0.2	0.6 ± 0.2
K_2O	0.2 ± 0.1	0.2 ± 0.1	0.3 ± 0.1	0.5 ± 0.1	0.2 ± 0.1	0.5 ± 0.1
CaO	6.9 ± 1.0	5.6 ± 0.8	6.5 ± 1.0	7.3 ± 1.1	6.4 ± 1.0	6.0 ± 0.9
TiO_2	1.2 ± 0.2	1.4 ± 0.2	0.9 ± 0.1	1.1 ± 0.2	1.1 ± 0.2	1.3 ± 0.2
FeO	6.6 ± 1.7	4.4 ± 1.4	7.3 ± 1.7	3.4 ± 1.3	7.4 ± 1.7	7.1 ± 1.7
OS	68.6	78.2	89.1	99.2	92.9	98.9

(OS)= Original sum of oxides prior to normalization, normalized to 98%

With the addition of the Mars Global Surveyor's thermal emission spectrometer, corresponding results were found with basaltic material in the ancient southern highlands and andesitic material in the younger northern lowlands. These satellite and rover data sets will be compared to assess deposition and/or alteration of minerals through Martian history.

THE GLOBAL ESCARPMENT

Mars has a crustal dichotomy that is defined by abrupt differences in composition and elevation between the southern highlands and the northern lowlands. This global escarpment is unique in the solar system in that it girdles a major planet. The global escarpment is by far the largest feature on the Martian surface visually spanning more than 10,000 km in the eastern hemisphere. If it were present in the western hemisphere, it is now masked by volcanic flows of the Tharsis region. Slopes along the escarpment range from 20 to 30º with neighboring debris aprons and flow fronts sloping between 1 to 6º (Carr 2001).

Endogenic Processes

Internal (endogenic) models such as mantle or long-wavelength convection could have caused the formation of the escarpment (Nimmo and Stevenson 2001). According to Nimmo and Stevenson (2001), degree-1 mantle convection develops in a planet with the core size and planetary radius of Mars. Physical properties vary at depth, such as a mineralogical phase change or temperature- and pressure-dependent viscosity; these would drive a long-wavelength perturbation and cause it to be the fastest growing structure in the lower mantle. Two plausible explanations arise from degree-1 mantle convection in order to explain the escarpment. First, the primitive planet has yet to form a crust at all. Mantle upwelling in the form of a super plume solidifies to become the primordial crust and thickens over time to become the southern highlands (Roberts 2004).

Alternatively, lithospheric thinning by vigorous mantle convection could have caused a lowering of the entire northern hemisphere (Wise et al. 1979b; Fig. 8). All convection models assume a crustal thickness of approximately 50 km (Zuber et al. 2000). Another endogenic process such as plate tectonics would involve the spreading of the Borealis Basin. Through this process, crustal subduction under the southern highlands could have caused the escarpment (Sleep 1994).

Figure 8. Example of degree-1 mantle convection plume model. From Roberts and Zhong (2006).

Exogenic Processes

External (exogenic) processes are the other competing possibility for the escarpments origin. Extra-planetary sources such as comets or asteroids are one way to change the surface of a planet. Wilhelm and Squyres (1984) proposed that a single giant impact would have formed a basin ~ 7,700 km in diameter, centered at 50ºN 190ºW.

Later, others such as Andrews-Hanna et al. (2008) proposed an impact ellipse measuring approximately 10,600 by 8,500 km, centered at 67° N, 208° E (Fig. 9). If the impact origin of the Northern Basin of Mars is correct, such a crater would dwarf any other in the solar system by a factor of two (Table 4).

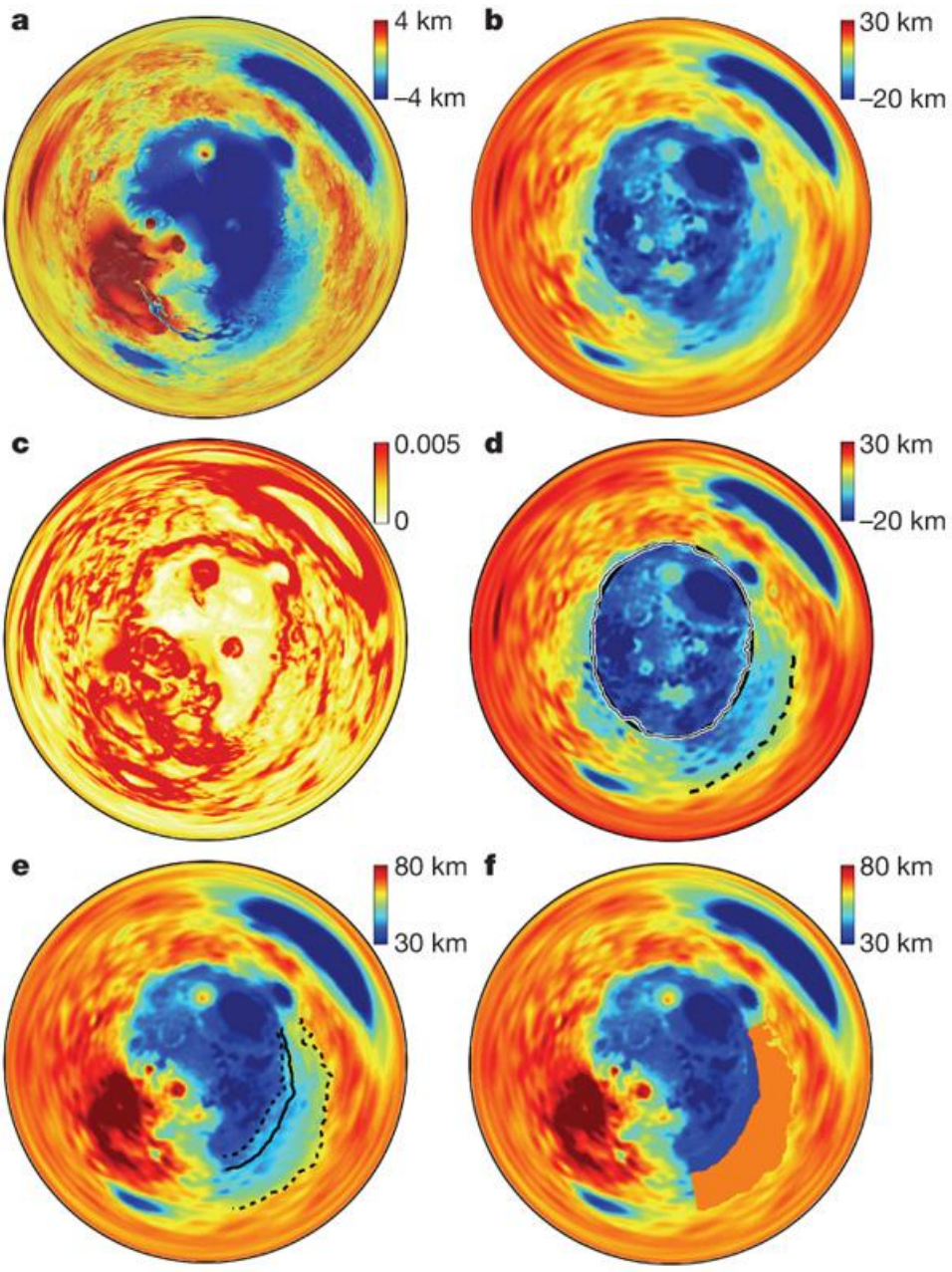

Figure 9. Views of the Borealis Basin: (a) polar projection around the basin center at 67° N, 208° E, showing the present-day topography and shaded relief of Mars; (b) the modeled crustal root; (c) the modeled topographic gradient; (d) traced dichotomy boundary is shown and compared with the best-fit ellipse (southern boundary of Arabia Terra denoted by dashed line); (e) outlines of the northern and southern edges of Arabia Terra (dotted lines; approximated using a threshold crustal thickness) are shown over a crustal thickness map along with the reconstructed basin rim required to restore the crustal thickness in Arabia Terra to the mean highlands value; (f) reconstructed crustal thickness before basin modification in Arabia Terra. From Andrews-Hanna et al. (2008).

Table 4. List of largest known impact basins in the Solar system. From USGS 2010a Planetary Nomenclature. (Accessed on 12 Jan., 2010).

	Name	Location	Size (diameter)
1	Aitken basin	Moon	2,500 km
2	Hellas Basin	Mars	2,100 km
3	Skinakas Basin	Mercury	~1,600 km
4	Caloris Basin	Mercury	1,550 km
5	Mare Imbrium	Moon	1,100 km
6	Isidis Planitia	Mars	1,100 km
7	Mare Tranquilitatis	Moon	870 km
8	Argyre Planitia	Mars	800 km
9	Mare Serenitatis	Moon	700 km
10	Mare Nubium	Moon	700 km
11	Beethoven	Mercury	625 km
12	Valhalla	Callisto	600 km, rings to 4,000 km diameter
13	Hertzsprung	Moon	590 km
14	Turgis	Iapetus	580 km
15	Apollo	Moon	540 km
16	Huygens	Mars	470 km
17	Schiaparelli	Mars	470 km
18	Menrva	Titan	440 km
19	Korolev	Moon	430 km
20	Dostoevskij	Mercury	400 km
21	Odysseus	Tethys	400 km
22	Tolstoj	Mercury	390 km
23	Goethe	Mercury	380 km
24	Tirawa	Rhea	360 km
25	Mare Orientale	Moon	350 km, rings to 930 km diameter
26	Epigeus	Ganymede	340 km
27	Gertrude	Titania	320 km
28	Asgard	Callisto	300 km, rings to 1,400 km diameter
29	Vredefort crater	Earth	300 km

*There are approximately twelve more unnamed impact craters/basins larger than 300 km on the Moon, five on Mercury, and four on Mars.

The largest and most complex impact related structures are called multi-ring basins. They contain concentrically oriented radial rings with inward facing scarps (Melosh 1989). Multi-ring basins on Mars are divided into three groups depending on the

increase in diameter of the basin: (1) 300 < D < 1850 km; (2) 1850 < D < 3600 km; (3) D > 3600 km (Schultz and Frey 1990). Variations in multi-ring basin morphology may be related to lithospheric thickness, mechanical interactions between the basin-forming impacts, or the spherical geometry of the target (Schultz and Frey 1990). Theoretical models of large impact structures suggest that basin topography and the formation of concentric rings can differ due to post impact relaxation (Melosh 1982). Therefore, older basins are structurally and morphologically different than younger crater basins. Basin rings can be inferred by topography, channel geometry, and the distribution of radial concentric structures (Schultz et al. 1982). Past studies have used the Orientale basin, located on the Moon, as a template for all multi-ring basins of any planet (Head 1974). Orientale is the youngest and best preserved multi-ring basin and has not changed geomorphically since its formation ~3.85 billion years ago (Wilhelms 1987). Lithospheric thickness is an important factor in the development of concentric basin structure (Melosh and McKinnon 1978). With a relatively thin crust, post crater relaxation will dominate and topographic features will remain subdued, on the contrary, with a much thicker crust, the relaxation is limited allowing for the crater rim and ring structures to be more pronounced. Therefore, if the northern basin is an impact feature depending on the crustal thickness at the time of impact, we would expect to see some remnants of radial rings and inward facing scarps along the global escarpment.

More recent impact models have been developed using computer software and have evolved to reveal the pre-existing Martian crust before the Tharsis bulge had developed (Andrews-Hanna et al. 2008). One such model extrapolates the Borealis Basin as an elliptical shape suggesting an oblique impact from a large celestial object in early

Martian history (Andrew-Hanna et al. 2008; Fig. 10). During a mega-impact, the crust would have been thinned because of ballistic transport and the escarpment would represent the resulting crater rim (Marinova et al. 2008). Other elliptical basins are present on Mars such as Hellas and Utopia.

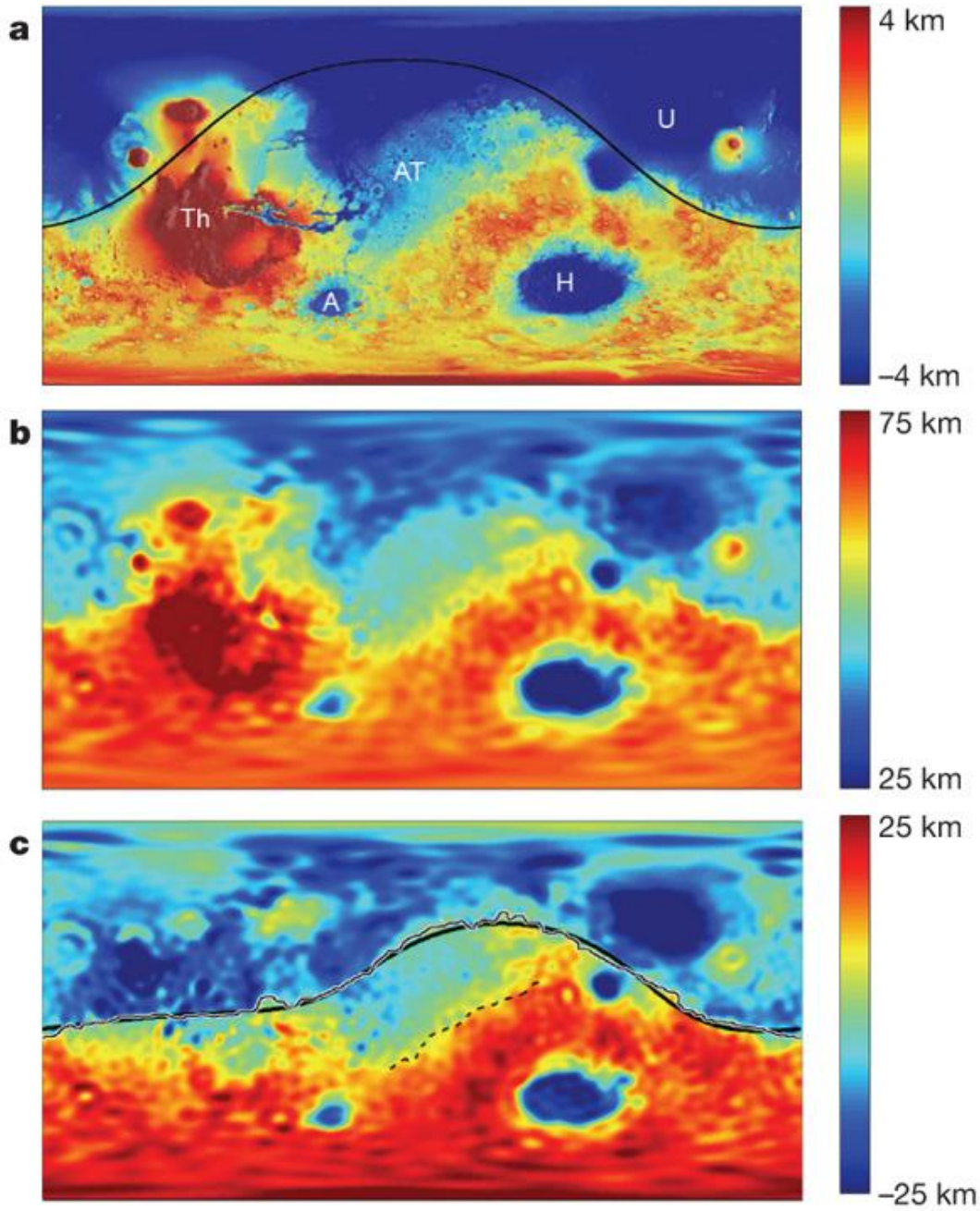

Figure 10. Cylindrical projections of: (a) topography (MOLA data) and (b) crustal thickness from Neumann et al. (2008) of Mars. Main features labeled in **a** include Tharsis (Th), Arabia Terra (AT), Hellas (H), Argyre (A), and Utopia (U), as well as the Borealis basin outline proposed by Wilhelms and Squyres (1984). In these cylindrical projections, crustal thickness was modeled with perturbation (isostatic root) showing continuation of the dichotomy boundary beneath Tharsis; (c) The observed dichotomy boundary (thin line) is compared with the best-fit ellipse (bold line). The break in slope separating Arabia Terra from the highlands is shown as a dashed line. From Andrews-Hanna et al. (2008).

The shape of the Borealis Basin has been under scrutiny by mantle convection advocates (e.g. Zuber et al. 2000) since the early exploration of the dichotomy. The irregular shape of this basin does not conform to typical impact features that leave either a circular or elliptical crater. One explanation is that multiple impacts are responsible for the irregular shape of the basin. By overlapping several large basins that formed early in the Martian past, the pattern of knobby/fretted material in the form of ancient crater rims would coincide with these impacts (Frey and Schultz 1998).

THE FRETTED TERRAIN

The fretted terrain is located along the global escarpment +/- 10º from 40º N latitude and confined between 280º to 350º longitude (Sharp 1973). The steep walled escarpment traces a somewhat irregular course along the southern boundary of the terrain beginning the planimetric pattern associated with the fretted terrain (Fig. 11). In some places, the terrain is dissected by flood channels growing wider northward and there are numerous island-like outliers who resemble butte and mesa structures.

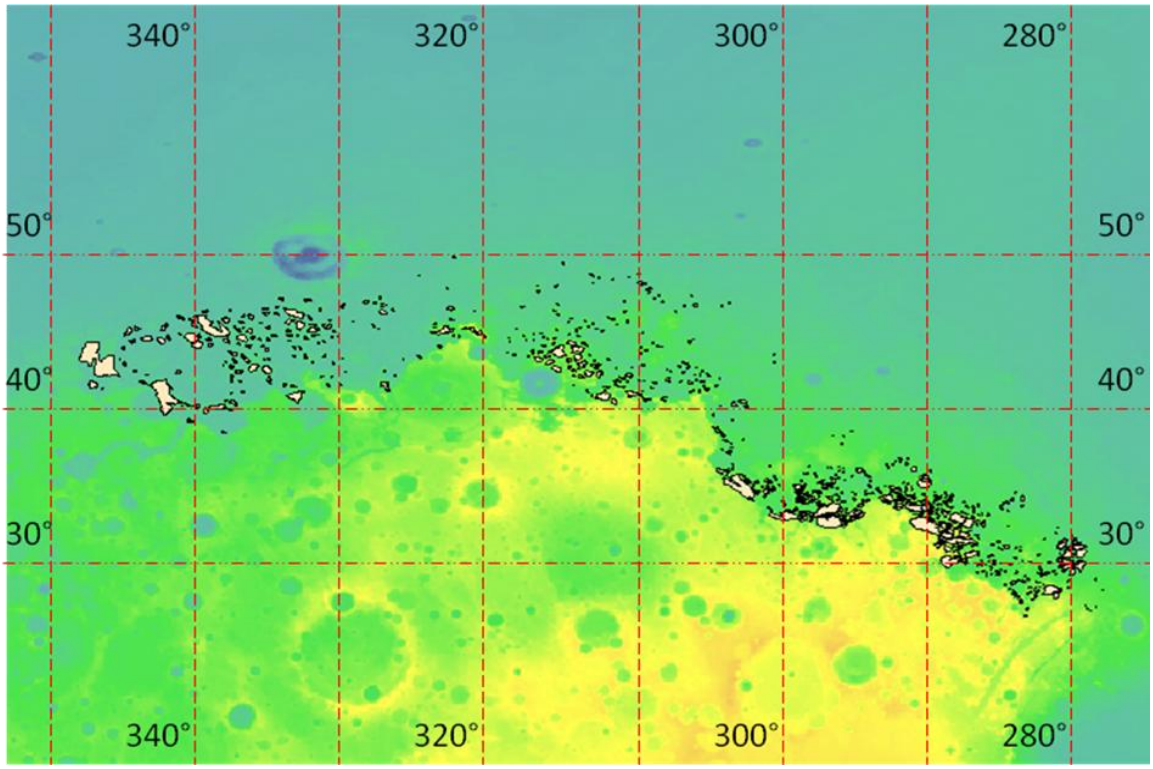

Figure 11. Map showing the location of the fretted terrain used in this project. Modified from USGS MOLA DEM (1999).

The time frame for the formation of the fretted terrain either coincides with its initial formation or is a product of an evolving scarp over time. During early Noachian, internal forces consisting of mantle convection or plate tectonics could have initially formed the terrain. If mantle convection created the global escarpment along with the fretted terrain, then the tops of these blocks should dip toward the northern lowlands as a product of crustal relaxation to fill the lower lying areas to maintain isostasy. External forces like single or multiple impacts creating a crater wall and terrace structure could have produced this type of terrain as well. This terrace effect would cause these fretted blocks to slope toward the southern highlands (Grieve 1987; Fig. 12). If an oblique, large impact were the scenario, then the terrace would not only tilt back toward the escarpment, but also tilt away from the original direction of the impactor.

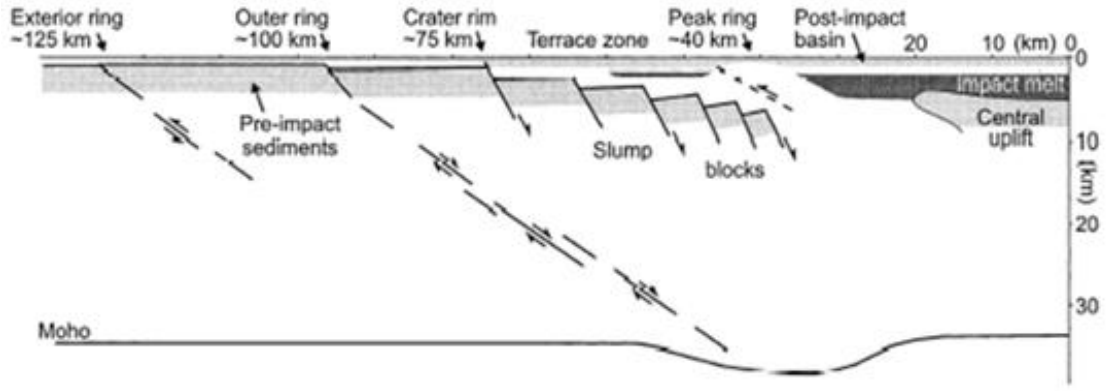

Figure 12. Example of terrace formation due to a large meteor impact at zero on the horizontal scale. From Morgan et al. (2000).

During Hesperian, the fretted terrain could have been caused by rifting following a linear crack which is prominent during this epoch, or it could be an erosional feature, such as a winding channel, due to intense runoff corresponding to the chaotic terrains that are present in the eastern region of Valles Marineris. If the formation of the fretted terrain

occurred during Amazonian such processes might involve either ice wedging or slumping and calving analogous to ice-wedging polygons (Sharp 1973; Fig. 13). The fretting process as defined by Sharp is “the receding of a steep scarp by undermining or sapping mechanisms, maintaining its steepness but developing a complex planimetric configuration.” By this process, a smooth, flat floor is created with isolated buttes and mesas.

Figure 13. Image of terrestrial, local scale, ice-wedge polygons located in Barrow, Alaska. From Lucchitta (1980).

Another proposed formational process for the escarpment and fretted terrain could be the representation of a huge paleoshoreline (Parker et al. 1993). Vastitas Borealis is extremely smooth like the abyssal plain of Earth’s oceans and the volume of water required to fill the basin is within the upper boundary of availability early in the Martian

history (Cattermole 2001). Below contact 2 most surfaces are smooth, indicative of abyssal plain deposits, whereas contact 1 encompasses rougher terrain and could potentially be a short interval of a Martian sea-level high-stand (Parker et al. 1993; Fig. 14).

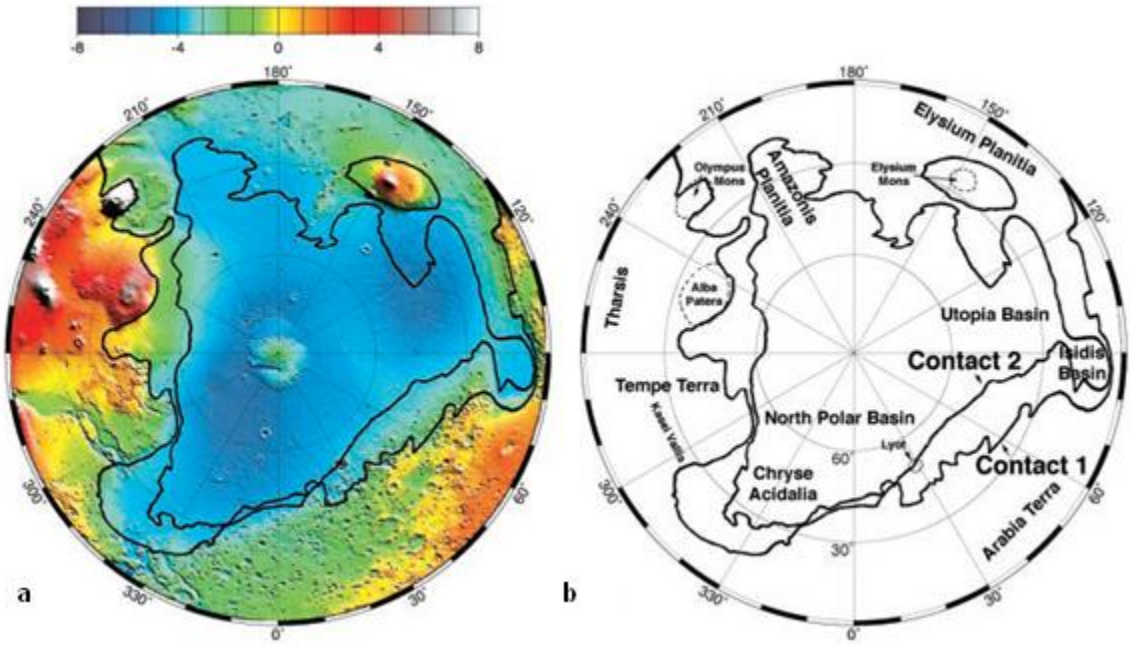

Figure 14. Mars northern polar view: (a) Lambert equal area projection of MOLA Northern Pole-to-equator topography from Smith et al. (1999). Black lines indicate positions of contacts interpreted to be shorelines; (b) Major features as seen in (a). From Head et al. (1999).

Depending on the slope orientation of the fretted-terrain blocks, inferences and comparisons can be made about the possible formation and continuing geomorphic processes. Dips toward the lowlands would involve crustal relaxation and /or sapping and mass wasting over time. Horizontality or little dip to the top of each block would indicate thermokarst activity or a remnant ring structure. Thermokarst activity could also produce a concave structure on the tops of the blocks. If the fretted terrain blocks dip away from the lowlands or the majority of the blocks dip to the east or west, they could have

possibly been formed during a major impact in the past (as shown in Fig. 12). Because the terrain is composed of the same rock type, the weathering processes over time should be relatively consistent over the entire scarp. All imagery processing and modifications will be cross-checked with other imagery data bases and then compared to past literature for review.

MISSIONS AND INSTRUMENTATION

Mars Global Surveyor

Mar Global Surveyor operated by the Jet Propulsion Laboratory (JPL) arrived at Mars on September 11, 1997 and continued to collect data until November, 2006. Its longevity was due in part to the ingenious use of angular momentum management implemented in August, 2001 to conserve propellant and extend the orbiters lifespan by an additional three years. Mars Global Survey was designed to encircle the planet every two hours in a polar orbit at an altitude of 378 kilometers (NASA 2010a). The altitude was chosen to take advantage of a sun-synchronous orbit to obtain identical light conditions unconstrained by the date of the corresponding data. Six scientific instruments were mounted on the spacecraft and four were used in this study: (1) MOC – Mars Orbital Camera; (2) MOLA – Mars Orbital Laser Altimeter; (3) TES – Thermal Emission Spectrometer; (4) MAG/ER – Magnetometer and Electron Reflectometer; (5) USO/RS – Ultra-stable Oscillator for Doppler measurements; and (6) MR – Mars Relay

MOC– Mars Orbital Camera

The Mars Orbital Camera was designed to take highly detailed images from any orientation with respect to the horizon. It consists of two independent cameras each supported by a 32-bit microprocessor. The narrow angle camera utilizes a 70 cm, f/10 Ritchey-Critien reflector and with two 2048-element charged couple device (CCD) is able to resolve objects as small as 1.4 m/ pixel (Dallas 1996). Owing to the size of the

data set, high resolution images are black and white sacrificing color for clarity. The wide-angle camera contains two f/6, fish eye lenses, paired with two 3456-element CCD's. This arrangement allowed for the acquisition of color images between 575 and 625 nm with a resolution of 250 m/pixel as MOC collected more than 240,000 images during the life span of the instrument (MSSS 2010).

MOLA - Mars Orbital Laser Altimeter

MOLA was constructed to generate high resolution topographic profiles. With the use of a diode-pumped neodymium-yttrium, aluminum-garnet laser and a firing rate of 10 pulses per second, MOLA was able to obtain the most accurate and complete LIDAR (light detecting and ranging) set of any planetary body in the solar system, including Earth. Recording the lag time between the firing and interception of the reflected laser pulses by the 50 cm Cassegrain collecting mirror gives a precise local altitude on the surface. Each laser spot measured approximately 160 meters in diameter and were spaced 300 meters apart (Dallas 1996). This technique yielded a range resolution of one to ten meters up to 30º slopes, and an absolute accuracy of ~1 meter (Zuber et al. 1992). A high resolution map composed of 27 million elevation measurements was used to create a DEM which is the base map of topography for this study.

TES – Thermal Emission Spectrometer

The TES was comprised of two telescopes and used to determine thermal and mineralogical properties on the Martian surface. The larger 15.24 cm Cassegrain telescope bolsters a two port Michelson interferometer spectrometer with a 6.25 to 50 μm spectral range. The smaller telescope supplies two channels (0.3 to 3.9 μm and 0.3 to 100 μm) respectively. Because the instrument utilizes six detectors and is nadir pointed (180º

from the zenith), illumination values can be obtained for surface comparisons (Christensen et al. 2001).

USO/RS – Ultra stable Oscillator for Radio Science

A two-fold approach is used with the final MGS instrument. Observations of the distortions, which include frequency, phase, and amplitude, of the spacecraft's radio signal through the Martian atmosphere can produce a high resolution temperature profile. Also by instituting the Doppler tracking and monitoring the minute changes in the frequency, a gravity field can be reconstructed with a high level of accuracy. The only way to accomplish this is by providing an ultra-stable oscillator with extremely stable frequencies for the reference. A frequency of 19.143519 MHz was chosen to limit variations to less than 1.0 in 10^{10} Hz (Dallas 1996).

MRO - Mars Reconnaissance Orbiter

Orbital insertion of MRO, which is operated by JPL, was achieved on March 10, 2006. The payload for this satellite consists of six different instruments: (1) HiRISE - High Resolution Imaging Science Experiment; (2) CRISM - Compact Reconnaissance Imaging Spectrometer for Mars; (3) CTX - Context Imager; (4) MCS - Mars Climate Sounder; (5) MARCI – Mars Color Imager; and (6) SHARAD – Shallow Subsurface Radar. Only the first three will be discussed and used in this project. The MRO is also operated in a sun-synchronous, polar orbit located closer to the Martian surface than MGS only skimming the surface at altitude between 255 to 320 km (Murchie et al. 2004). The MRO served a dual purpose with the high resolution imagery and spectrometers aboard, it could provide instant data, but also look for potential landing sites for future Martian missions.

HiRISE – High Resolution Imaging Science Experiment

HiRISE is unparalleled for image quality, coverage, and resolution to the present date. An aperture of 50 cm, the largest ever carried into deep space, gives a resolution of approximately 30 cm/pixel. The images are collected in three color bands, 400 – 600 nm, 550 – 850 nm, and 800 – 1,000 nm. With a lager storage capacity than previous satellites, images can be taken in different modes increasing image sizes from a few to 28 megabits (Graf et al. 2005).

CRISM – Compact Reconnaissance Imaging Spectrometer for Mars

High resolution hyperspectral images were taken in the electromagnet spectrum between 0.4 to 4.0 μm and were used to indicate water and hydrothermal systems by mineralogical means (Graf et al. 2005). The instrument encompasses a Ritchey-Chretien, 10 cm telescope with 2.06º field of view and two corresponding spectrometers. The light is split inside the spectrometer with a dichroic into visible, near-infrared, and infrared (Murchie et al. 2004). Unique to CRISM is the gimbal mounting which enables a specific target to be track as opposed to just being in the swath path.

CTX – Context Camera

The CTX is capable of 6m/pixel resolution using its 10.8 cm aperture. Differing from the other instruments by more than twice the field of view of the CRISM (5.8º) and a 5,000 pixel detector allow for a larger area to be scanned in a shorter period of time (Graf et al. 2005).

Mars Odyssey

On October 24, 2001 the insertion period began for Mars Odyssey spacecraft under the direction of Arizona State University (ASU). The satellite carried three scientific instruments onboard: (1) THEMIS – Thermal Emission Imaging System; (2) GRS – Gamma Ray Spectrometer; and (3) MARIE – Mars Radiation Environment Experiment (Fig. 15). Again only THEMIS is used in the present project and will be the only instrument discussed further. Odyssey not only provides data from its payload instrumentation, but also acted as a transmitter for the Martian rovers Spirit and Opportunity (NASA 2010b).

THEMIS was used to investigate physical properties and mineral compositions of the Martian surface. Collecting images in nine wavelengths in the thermal-infrared (6.8 to 14.9 μm) and five bands in the visible/near-infrared (0.42 to 0.86 μm) gives this instrument the ability to function day or night with its 12 cm aperture and 100 m/pixel resolution capability. By decreasing the resolution, a larger swath path can be achieved thus providing the ability to map the entire surface of the planet during the lifetime of the satellite. Because most geological materials have strong fundamental, vibration absorption bands in the thermal-infrared part of the spectra, THEMIS should provide insight into mineralogical compositions of the planet's surface (Christensen et al. 2001).

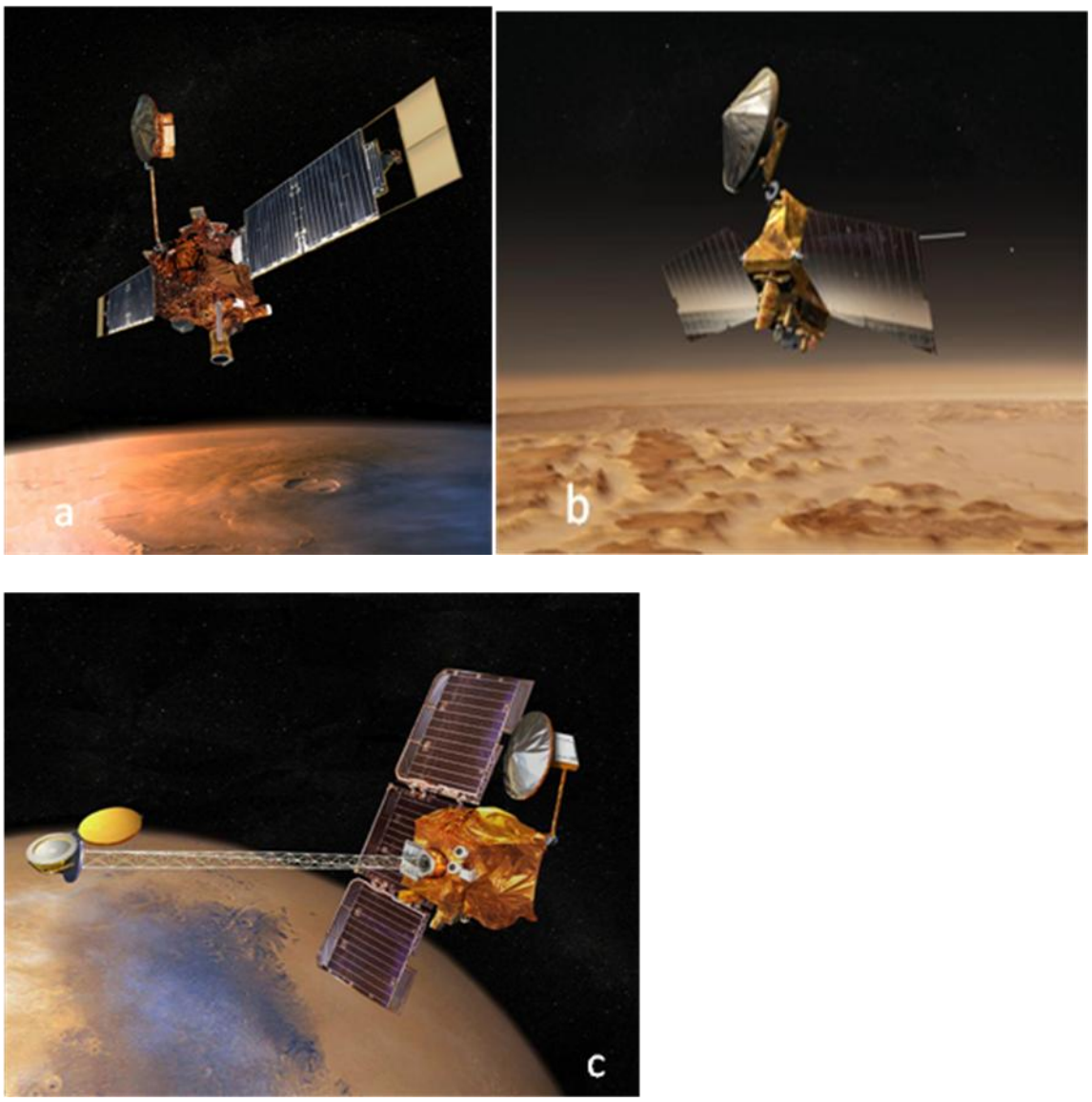

Figure.15. Satellites that generated data used in this project: (a) Mars Global Surveyor; (b) Mars Reconnaissance Orbiter; (c) Mars Odyssey Spacecraft. All images from NASA 2010d. (Available from http://mars.jpl.nasa.gov/gallery/spacecraft/index.html).

METHODOLOGY

Remote Sensing was defined by Pruitt (1962) as "The acquisition and measurement of data/information on some properties of a phenomenon, object, or material by a recording device not in physical, intimate contact with the features under surveillance." For monetary reasons, remote sensing is arguably the best, current viable way to study planetary bodies. With the advancement of technology and instrumentation, a wealth of knowledge can be obtained through these processes. Three satellites (Mars Global Surveyor, Mars Reconnaissance Orbiter, and Mars Odyssey; Fig. 15) were used in the study, each with multiple instruments to gather information on Mars. Imagery was used to digitize and map the location, shape, and orientation of the global escarpment and fretted terrain. In addition, MOLA data will be used to map the profile of the corresponding fretted terrain and escarpment to help determine slope stability. This information along with mineralogical data will potentially give us evidence that the Borealis Basin was formed by either endogenic or exogenic processes.

Data Extraction

The initial stage of this project involved a survey of the global escarpment and fretted terrain using Google Earth 5.0. Three dimensional global projections can be represented by using this type of software. The tilt and zoom can be adjusted allowing for any aspect or orientation to be analyzed. An application for the planet of Mars gives access to six global maps including Visual, MOLA, Daytime Infrared, Nighttime

Infrared, Viking Color, and MDIM 2.1which provide a quick reference to the surface of Mars. There is also an imagery data base of five orbital satellites: (1) HiRISE; (2) CTX; (3) MOC; (4) HRSC; and (5) CRISM with the ability of image importation and overlay allowing multiple applications to be presented simultaneously. Images from these orbiters can be extracted by turning on the corresponding satellite function and clicking on the image of interest. This application will connect you to one of the many websites where the data-base of images is located. From these databases, files can be downloaded, saved as a tiff file, and imported into Google Earth for overlay and rectification. Examination and processing of these maps and images will provide a three dimensional, interactive map for detailed quantitative analysis. An example of one of the maps used to research the proposed area is provided in Figure 16.

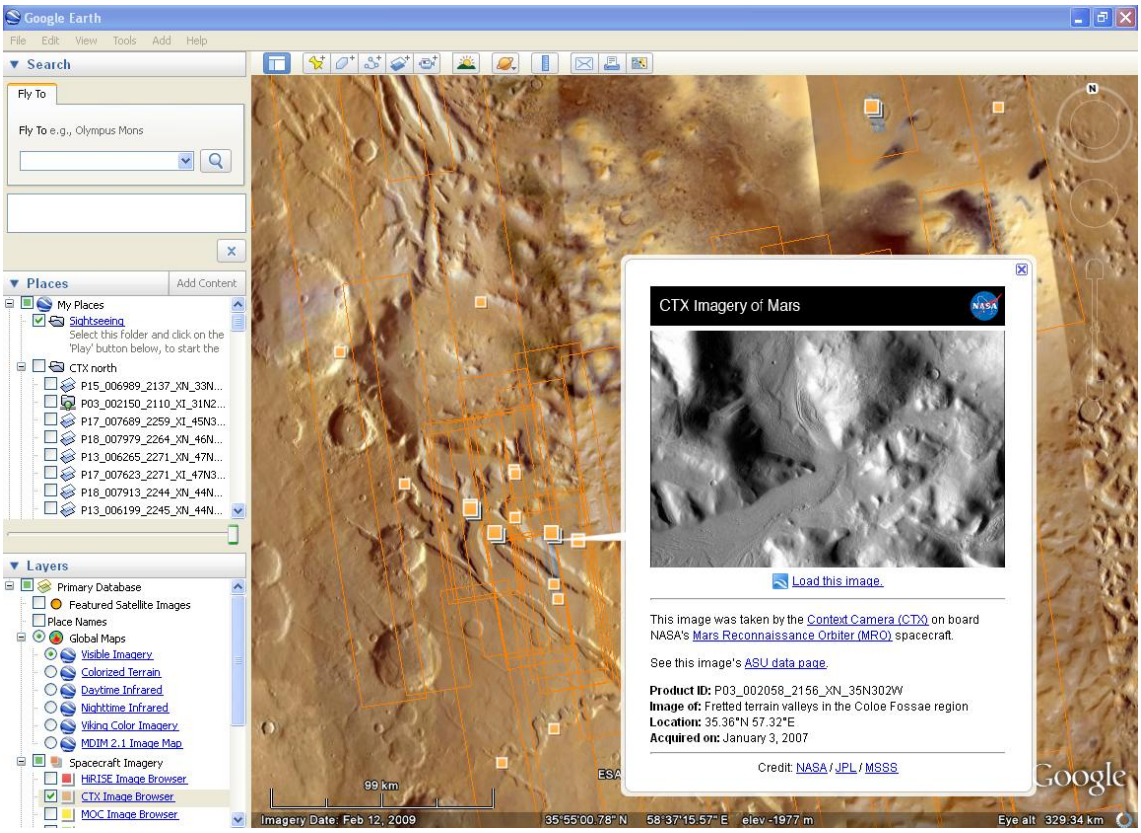

Figure 16. Applications in imagery overlays in Google Earth 5.0.

Any planetary study must first begin with an accurate base map. The United States Geological Survey (USGS) website (1999) (fttp://pdsimage2.wr.usgs.gov/pub/pigpen/mars/mola/) offers a wealth of data-bases from which files can be downloaded. MOLA data are the most complete topographic data set that is currently available of Mars. For this reason, it makes an excellent base map for which all other data can be positioned. The simple, cylindrical projection used for MOLA data was acquired from the USGS site with the file name (mola128_88Nto88S_Simp_clon0)zip. The MOLA data set is a digital elevation model raster data set which contains information in x, y, and z coordinates for each pixel

providing a three dimensional map that can be imported into GIS for detailed analysis of topography including elevation profiles, slope, and orientation of morphology.

Additional data were collected from the USGS Planetary GIS Web Server, the Planetary Interactive G.I.S.-on-the-web Analyzable Database (PIGWAD) (http://webgis.wr.usgs.gov/pigwad/maps/index.html). The database incorporates a multitude of capabilities for image processing and analysis. The layers involved for this project include: (1) Mars Orbiter Laser Altimeter (MOLA); (2) Mars Orbital Camera (MOC); (3) Mars Reconnaissance Orbiter (MRO); and (4) Mars Odyssey Mission (THEMIS-Thermal Emission Imaging System). These layers can be accessed in PIGWAD using the select by line/polygon tool to draw a line across an area of particular interest. Any image that is crossed by that corresponding line will then be available as a tiff file for analysis in GIS.

The Arizona State University website (http://mars.asu.edu/data/) provides access to many other data sets that have been acquired from various orbiting satellites and were used for downloading corresponding images.

Data Incorporation

A three dimensional global projection map was used in Google Earth (GE) 5.0. The layers that were used in this project included the MOLA, MDIM 2.1, and Visible because they are the highest resolution maps that cover 100% of the planet's surface. Once the images were extracted, they were overlain and rectified to the correct position on the global projection using the stretch and transparency functions that is incorporated with the overlay tool in GE. Using this process, a mural was composed of 171 context

camera images (CTX) aboard the Mars Reconnaissance Orbiter covering more than 80% of the entire visual escarpment and fretted terrains (Fig. 17).

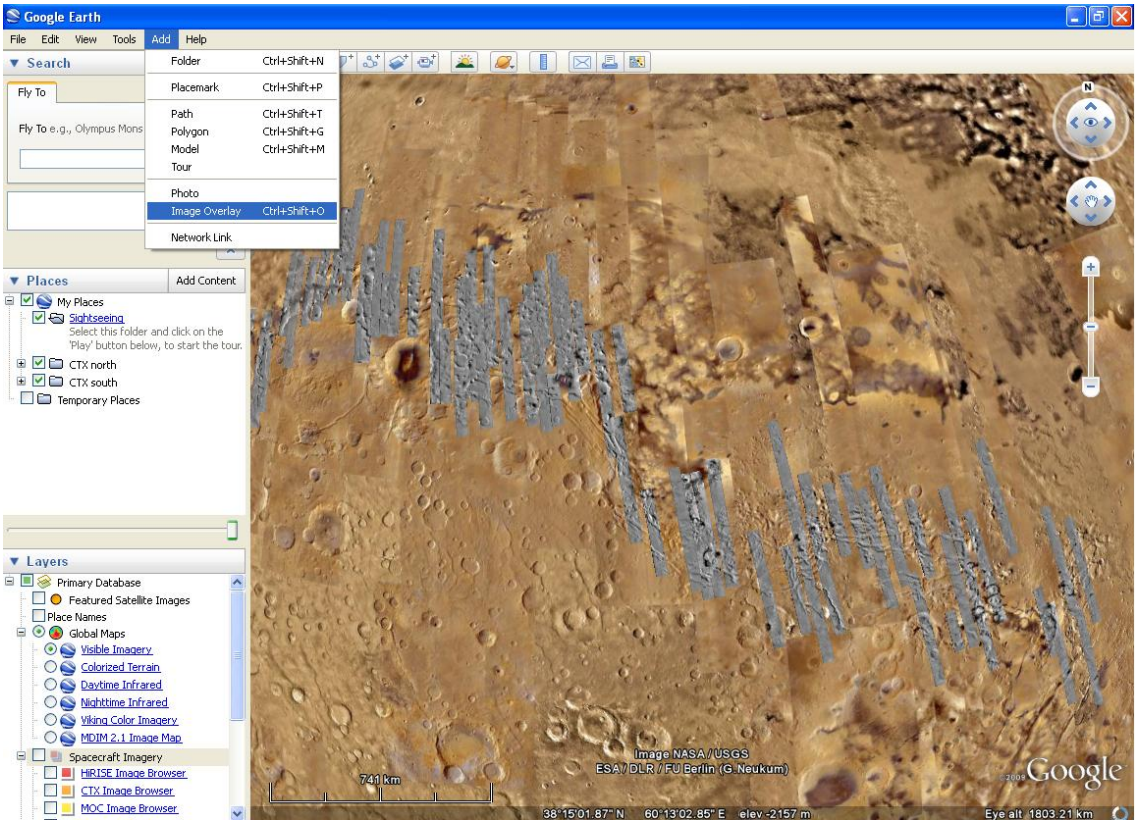

Figure.17. MDIM 2.1 and visible map with image overlays from context camera in Google Earth 5.0.

After the MOLA data set has been extracted from the USGS website, it can then be processed in GIS. First and foremost, since the study involves a celestial body other than Earth, the projection must be defined so the data line up properly in GIS that accounts for the size and shape of Mars. After adding the MOLA data to GIS (in this case ArcGIS 9.2) projection can be defined with a few commands (see Appendix 1). This allows the user to set the geoid, or in this case aeriod, to the current Martian projection system. From here, the linear unit was set to kilometers due to the large sizes of the

fretted terrain blocks. Finally, a coordinate system is selected: Select>>Solar System>>Mars 2000.prj. This sets the aeroid to the base coordinates of the MOLA data (semi-major axis = 3,396.19 km, semi-minor axis = 3,376.20 km) for use in GIS. Figure 18 illustrates the MOLA data in ArcGIS 9.2 with the data frame properties window open.

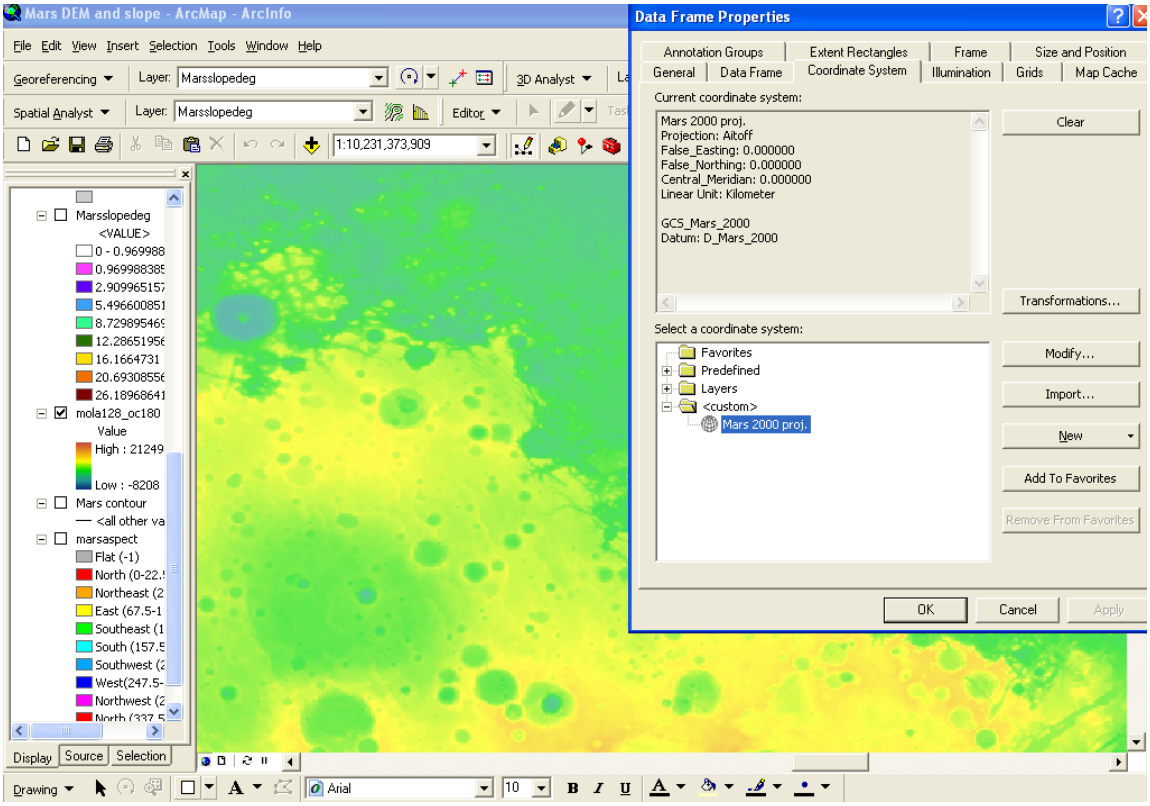

Figure 18. Defining projection of MOLA digital elevation model in ArcMap 9.2.

Using the MOLA data, a slope map was produced using the spatial analyst feature (see Appendix 1). Using the base map, slopes are calculated to a particular degree with a z factor = 1 and a cell size of 463.0836 meters. This will provide a ratio for inclination and slope stability (maximum angle of repose) that will be discussed later. A contour line and aspect (orientation as defined by north) can be extracted using the same spatial analyst tool. Owing to the size of some of these data sets (>10 GB), multiple maps were

generated for specific individual analysis. These maps are a vital part in the assessment of the global escarpment and fretted terrain. Depending on the formation and evolution of the fretted terrain, slope stability and directional orientation toward the sun could provide evidence of mass wasting and/or thermokarst activity.

Unprojected Mars global data sets from The Arizona State University website (http://mars.asu.edu/data/) are processed through a procedure termed georeferencing which allows for overlay of imagery with the MOLA base map. New unprojected imagery is added to GIS along with the rectified MOLA base map. Using the georeferencing tool in ArcGIS 9.2, ground control points (GCPs) can be added to the new map and then matched to the corresponding GCPs of the original base map (see also Appendix 1). The four corner controls points are sufficient to accurately georectify the imagery. This application was repeated for 25 overlays of imagery representing mineralogy, roughness, and albedo, among others.

Analysis Techniques

After the processing of all maps, data sets, and imagery; geospatial analysis proceeded. First, the global escarpment had to be established as a linear feature for the purpose of future comparisons and techniques. For this method, a shape-file was produced using ArcCatalog 9.2 (see Appendix 1) and added to the existing map. Using the editor tool in ArcMap, the escarpment was Heads-up digitized. Once in an editing session, the escarpment was digitized by selecting vertices using the slope map generated earlier. The slope angle of > 20º was used due to the maximum average angle of repose on Earth is roughly 40° for talus/regolith and since MOLA data resolution is 463 m² per pixel. With these two factors in mind, an average of 0 to 40º is 20° and therefore was

used to delineate the escarpment. The global escarpment was split into three different sections (northern low escarpment, northern escarpment, and southern escarpment) each with an individual shape-file in order for differing techniques to be processed later, such as buffers, orientations, and sizes of blocks. This will allow for the assessment of modification processes such as fluvial and eolian transport along with thermokarst activity depending on elevation and latitude.

The fretted terrain was considered as individual blocks for this study and could be classified as polygons accordingly. Since there are approximately 700 blocks to classify, the most efficient way to achieve this is by creating a personal geodatabase. This can be performed using ArcCatalog and allows you to incorporate multiple datasets into the same database (see Appendix 1). Finally, within each feature data set, new feature classes (in these instances, polygons) can be created again splitting the data into smaller, more discrete manageable pieces. The creation of personal geodatabases utilize topology and is a time saving technique for once the feature datasets are established, a table is constructed in the personal geodatabase feature class incorporating identification, length, and area for each polygon. After the feature datasets have been added to the map, the polygon creation can then commence utilizing the same technique for establishing the global escarpment for digitizing the blocks. Due to the vast differences in elevation traveling east to west along the escarpment, the fretted blocks were split into two different sections (blk- northern fretted terrain and polynorth- northern low fretted terrain) for analysis. Differences in elevation would play a deciding role as to how steep the potential debris aprons around the blocks can be and the possible interaction with ancient oceans as shore lines in the past as well as other geomorphological processes. The

classification scheme created to differentiate between a block or mesa and a knob or mound is as follows: (1) blk- a horizontal congruency of < 2º slope between adjacent pixels located on the top of the block and the perimeter of each block must be surrounded by pixels with at least 50% >20° and 75% >16º and; (2) polynorth- a horizontal congruency of < 2º slope between adjacent pixels located on the top of the block and the perimeter of each block must be surrounded by pixels with at least 25% >20°, 50% >16º, and 75% >12°. The two part classification scheme was used due to differing elevations of the two block groups which could promote different formational and erosional circumstances in the past. Blocks located at higher latitudes would have a greater probability of ice accumulation during the Martian seasons and processional cycle leading to faster erosion and lower angle debris aprons. With this established, digitization of each individual polygon was performed using an editor session in ArcMap accruing 580 blk and 132 polynorth polygons.

After the polygons were created, the center of mass had to be established in order to produce a center point for which long and short axis could be drawn. The corresponding lengths of the axis provide insight into orogenic and evolutionary processes. Extensional forces whether they are internally or externally driven would provide a plane of failure that would roughly mimic the corresponding escarpments orientation lending to greater average variation in the length vs. width ratio > 2:1. If water driven erosion were the culprit for the formational patterns, a dendritic pattern which is much more erratic can be deduced and the polygons would have an irregular shape. Finally, if ice wedging is the only cause for the formation of the fretted blocks, an average ratio of no greater than 2:1 would result as compared to similar blocks in higher

latitudes on Earth (see Fig. 13). ArcGIS has the ability for the use of scripts and tools for more customized applications. One such tool is Easy Calculator 5.0 (http://www.ian-ko.com/) which provides a variety of features for data extraction/organization for points, lines, and polygons. Using this tool, a center of mass for each polygon can be extracted (Fig. 19; see also Appendix 1). Once a center of mass is established axes can be drawn through the point to assess length vs. width ratios of these blocks. These shape-files (lines) can be exported as new feature classes in the featured datasets of existing personal geodatabases. Axes for each polygon were digitized perpendicular to one another in this process. Another tool can be incorporated with the axes to obtain compass bearing (see Appendix 1). With this process, length and orientation of these lines can be found which could possibly help determine orogenic processes. Again, assessment of the axes for random orientations or corresponding directions would provide evidence of either extensional or mass wasting processes. Once the long axis length has been computed, +90º can be added to the corresponding long axis for the orientation of the short axes.

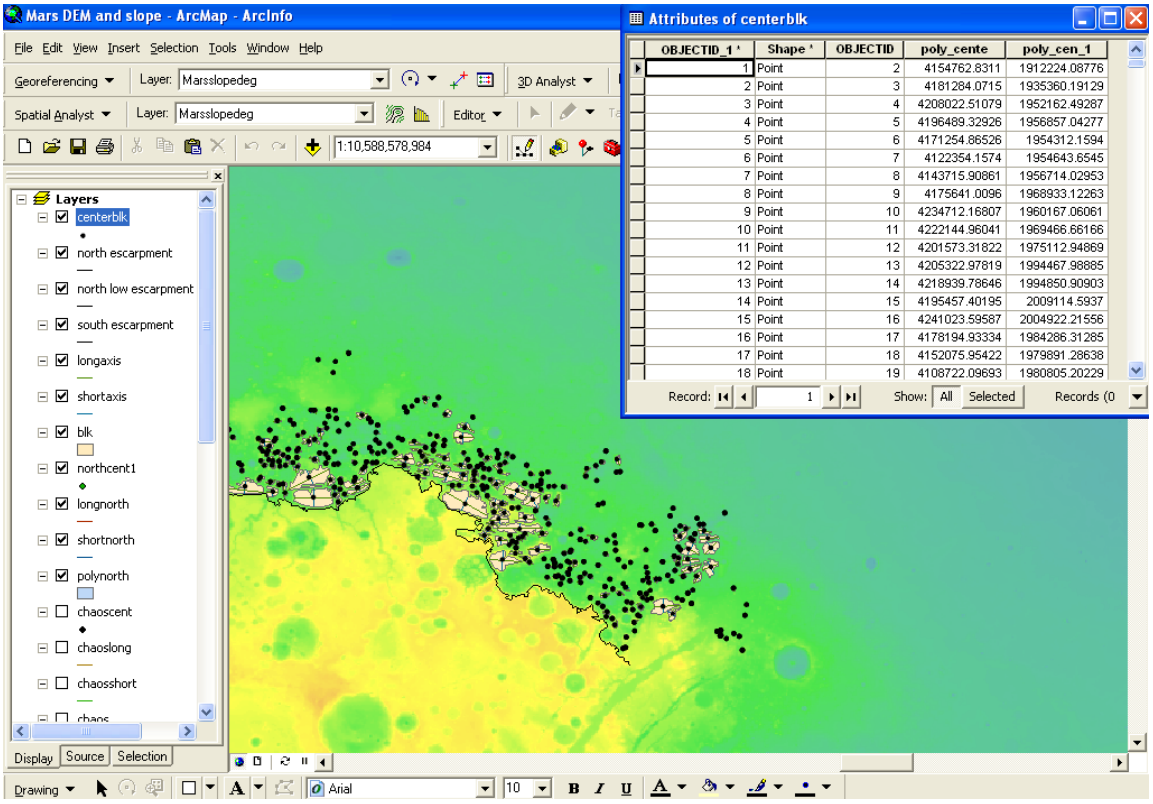

Figure 19. Geoprocessing of MOLA data for extraction of fretted terrain.

RESULTS

Regional Analysis

After insertion and rectification of the MOLA DEM base map in ArcGIS quantitative and qualitative analysis began. Regional scale was classified as interpretations made along any transect of > 500 km. The escarpment was split into two regions (northern- 280º to 325º and northern low- 325º to 350º) for this study on the criteria of elevation changes found along the boundary. The boundary line for the escarpment was traced along the greatest southerly extent with a slope of >20°. The change in elevation along the 1,884.8 km northern escarpment was approximately 2,400 meters with the greatest elevation of +1,039 meters around 27º 31'N, 284º 27' and lowest -1,377 meters around 43º 20'N, 323º 16'. The general dip in elevation followed a symmetric east to west pattern. Elevation differences along the 2,314.4 km northern low escarpment was at least -687 meters around 41º 12'N, 327º 25' and at most -3,618 meters around 44º 28'N, 345º 35', which demonstrated a difference of almost three kilometers from east to west. The 4,968.8 km southern escarpment ranged from +878 meters around 8º 24'N, 262º 54' to -1,334 meters around 2º 8'N, 228º 7'. There are variable fluctuations in the elevation, but the general trend here was roughly horizontal with no more than a few hundred meters of difference in elevation from east to west along the transect.

The northern escarpment primarily follows the division between the Noachian cratered plateau material (Nplc), Noachian hilly cratered material (Nhc), and Hesperian

knobby material (HNk). These two Noachian aged units were coeval with the early formation of the feature and the later erosion that takes place. Structurally the crust averages between 40 to 50 km thick, along this section of the escarpment suggesting a deeper seeded mechanism of origin rather than simple topology.

The southern escarpment was more erratic in that there was moderate symmetry as it followed the Noachian cratered plateau material (Nplc) and Hesperian knobby material (HNk), but there were intermingled units of Hesperian rolling plains material (Hpr) and Amazonian cratered plains material (Apc) that cut across the traced escarpment boundary. The crustal thickness of this section is between 50 and 60 km (Fig. 20).

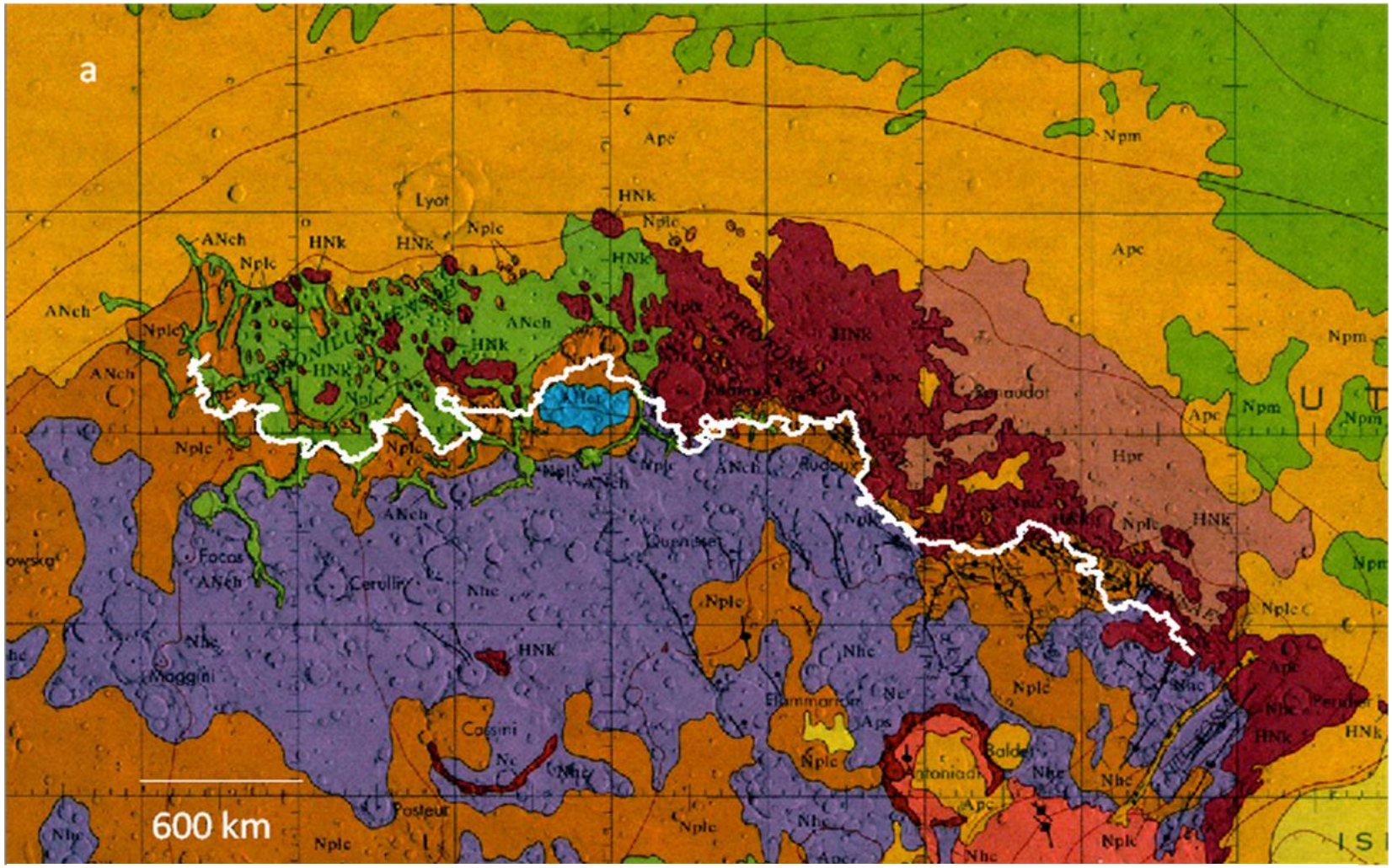

Figure 20. (a) Geologic Map of Mars including the northern escarpment. (White line delineates escarpment boundary line). Image modified from Scott and Carr (1978).

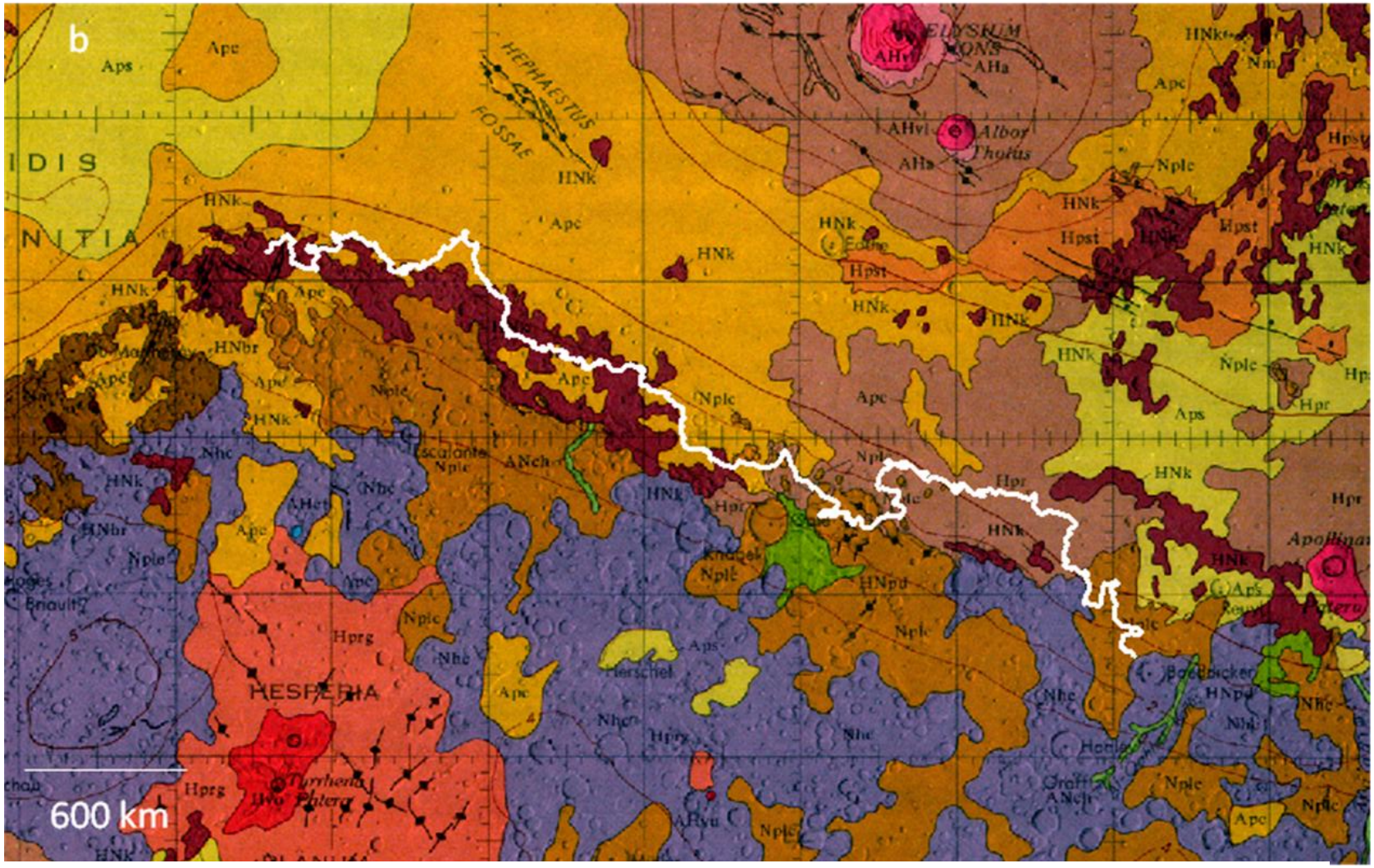

Figure 20. (b) Geologic Map of Mars including the southern escarpment. (White line delineates escarpment boundary line). Image modified from Scott and Carr (1978).

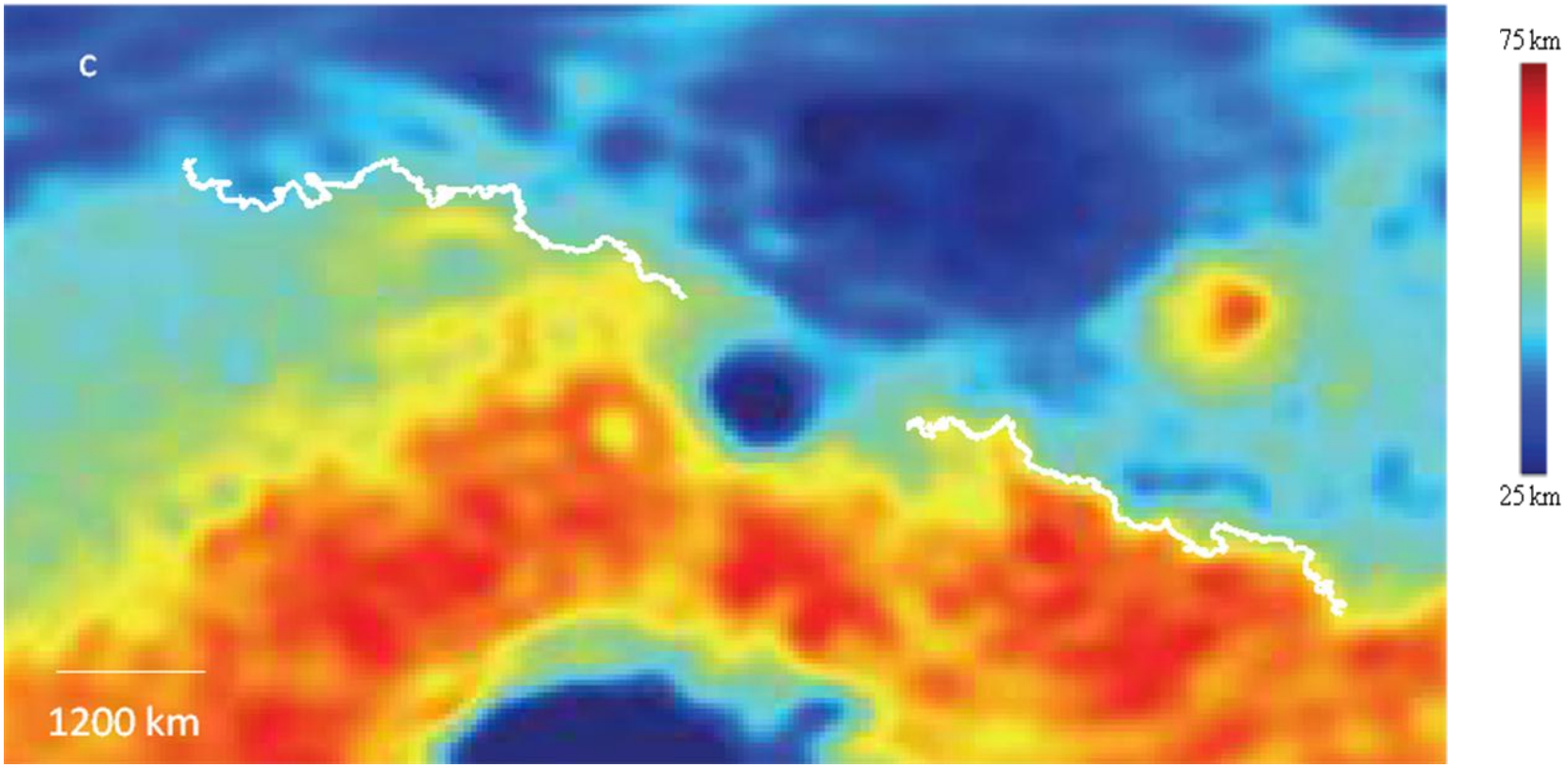

Figure 20. (c) Modeled crustal thickness map (0.5 pixel/degree), (White line delineates escarpment boundary line). Image modified from Andrews- Hanna et al. (2008).

Topographic cross sections were obtained using the previously incorporated DEM in ArcGIS corresponding with the earlier work of Andrews-Hanna et al. (2008) and Kiefer (2008) showing along the escarpment there are elevation changes of over 3 km over distances of <100 km depending on location. Other comparisons were made using the steep cliffs of Valles Marineris and the relic crater rims of Hellas and Argyre which can be found on the Martian surface (Fig. 21).

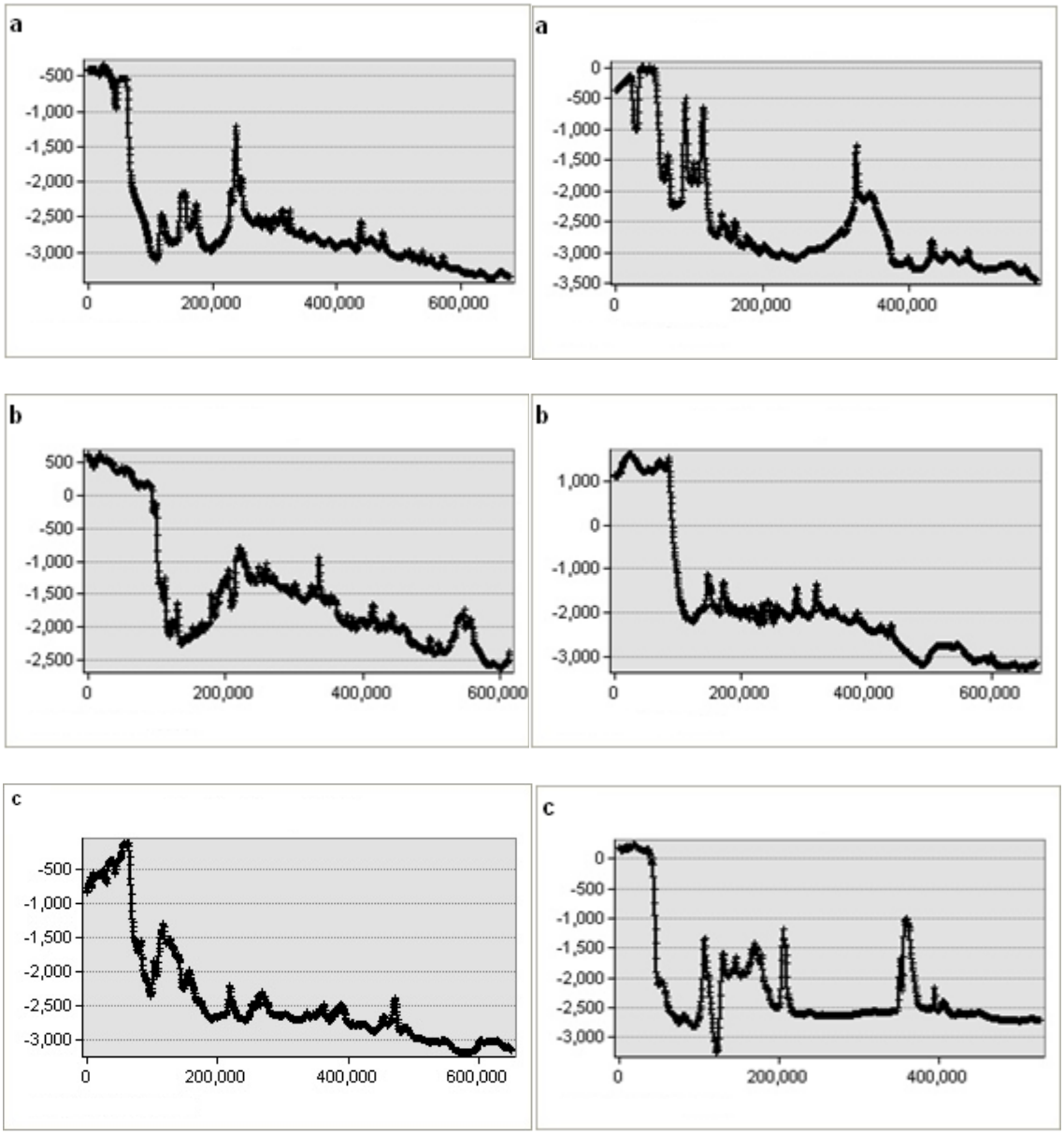

Figure 21. Cross sections along the entire global escarpment: (a) Two regional cross sections of the northern low global escarpment; (b) Two regional cross sections of the northern global escarpment; (c) Two regional cross sections of the southern global escarpment (scale = meters).

Regional mineralogy shows a distinct transition zone that is located approximately along the global escarpment boundary. Basaltic rocks are the dominant rock type south of the dichotomy in the highlands resulting from massive volcanic floods in the past, whereas andesite is more prevalent in the northern basin lending to a differing origin either from possible fissure filling due to crustal contracting or from excavation and mantle refilling due to a large impact (Fig. 22).

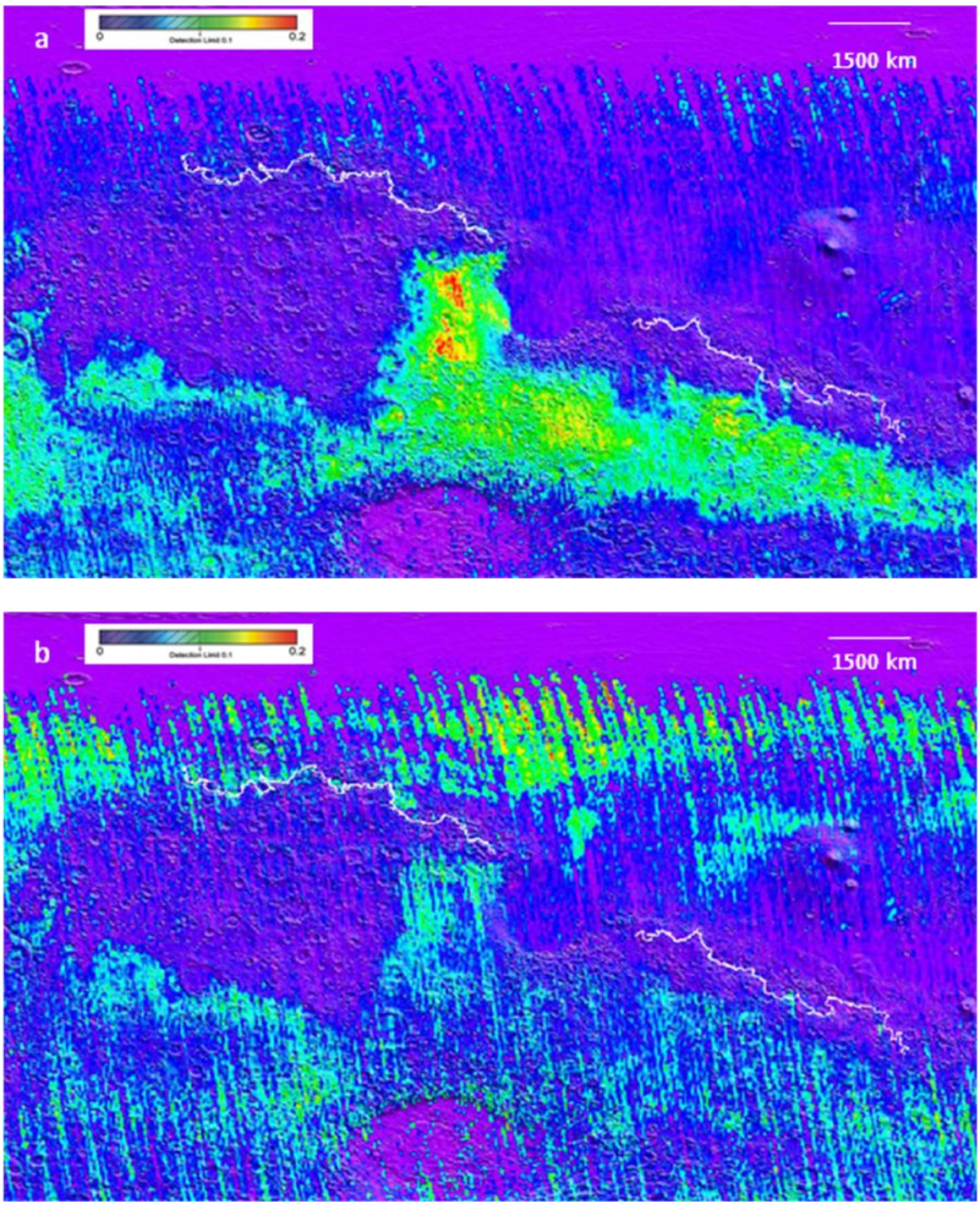

Figure 22. Intensity value map derived from TES mineralogical data: (a) basalt; (b) andesite (4 pixel/degree. White line delineates global escarpment). Images from Arizona State University, Mars Global Data Sets (2006).

Eight other regional maps were composed to gain a broader sense of the mineralogy. These maps are vital in assessing orogenic and evolutionary processes on a global scale for Mars. Bowen's reaction series is a classification scheme used to determine the silica content of magma at the time of cooling. Group 1 is the discontinuous series of Bowen's reaction series, whereas group 2 is the continuous reaction series (Fig. 23). These maps show the differentiation of the silica and possible cooling rate of the magma that was present at the time of deposition/intrusion and correspond with that mineral type.

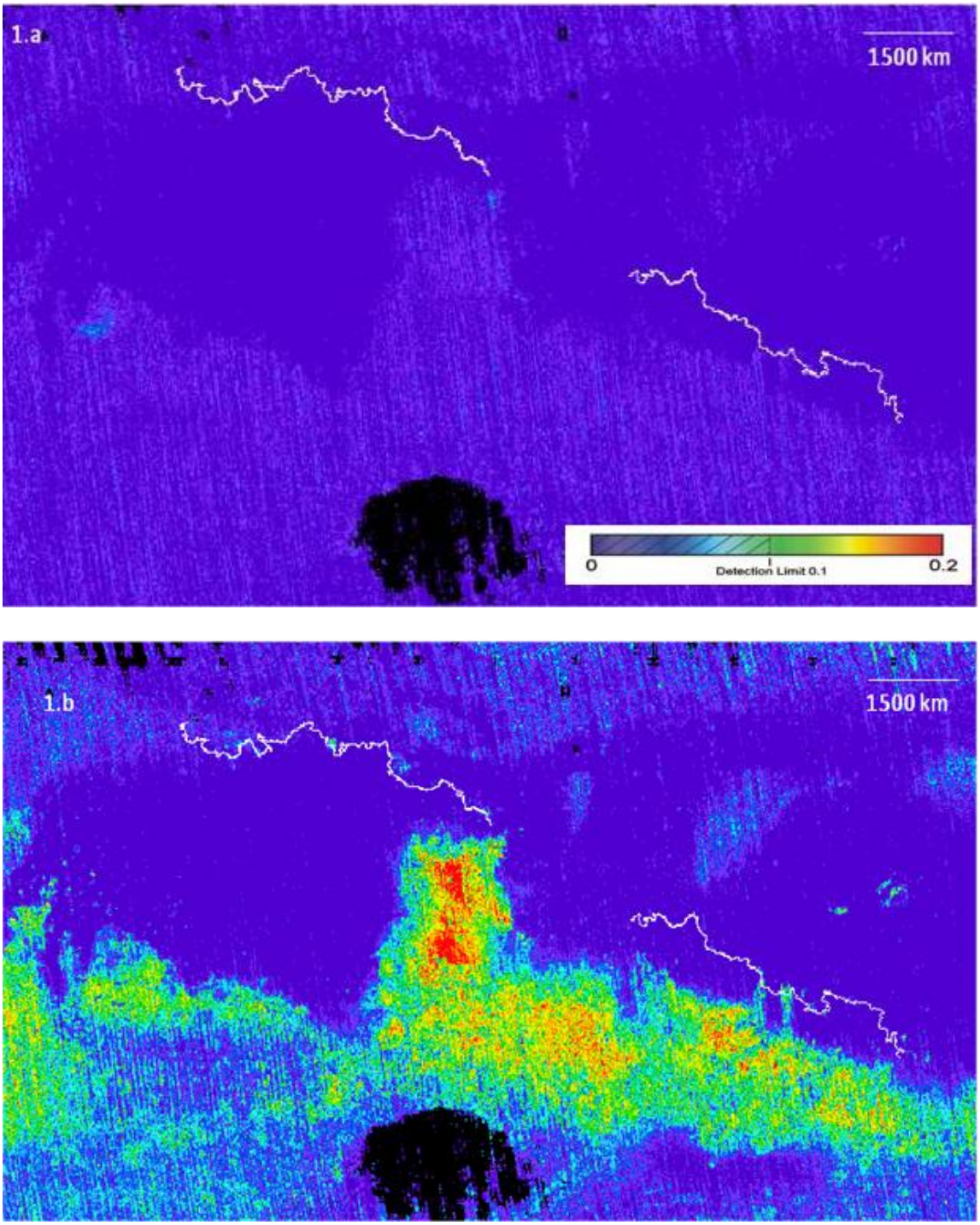

Figure 23. (Group 1a-b) Bowen's discontinuous reaction series including quartz acquired from TES mineralogical data: (1a) olivine; (1b) clinopyroxene. White line delineates global escarpment. Images from Arizona State University, Mars Global Data Sets (2006).

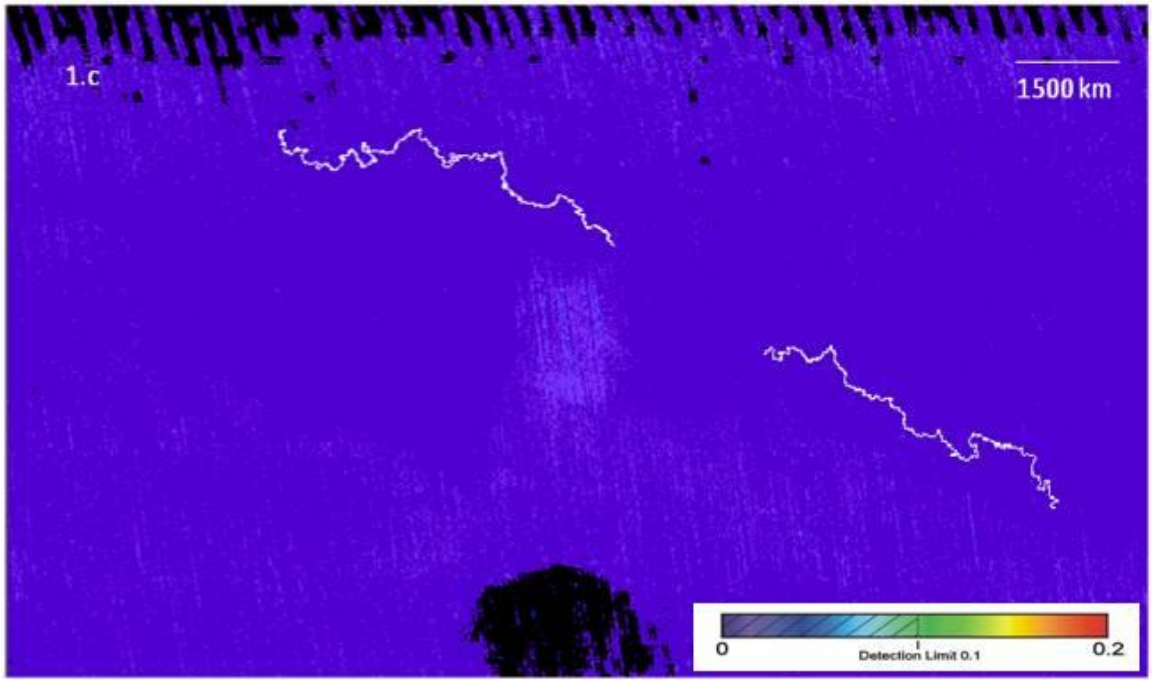

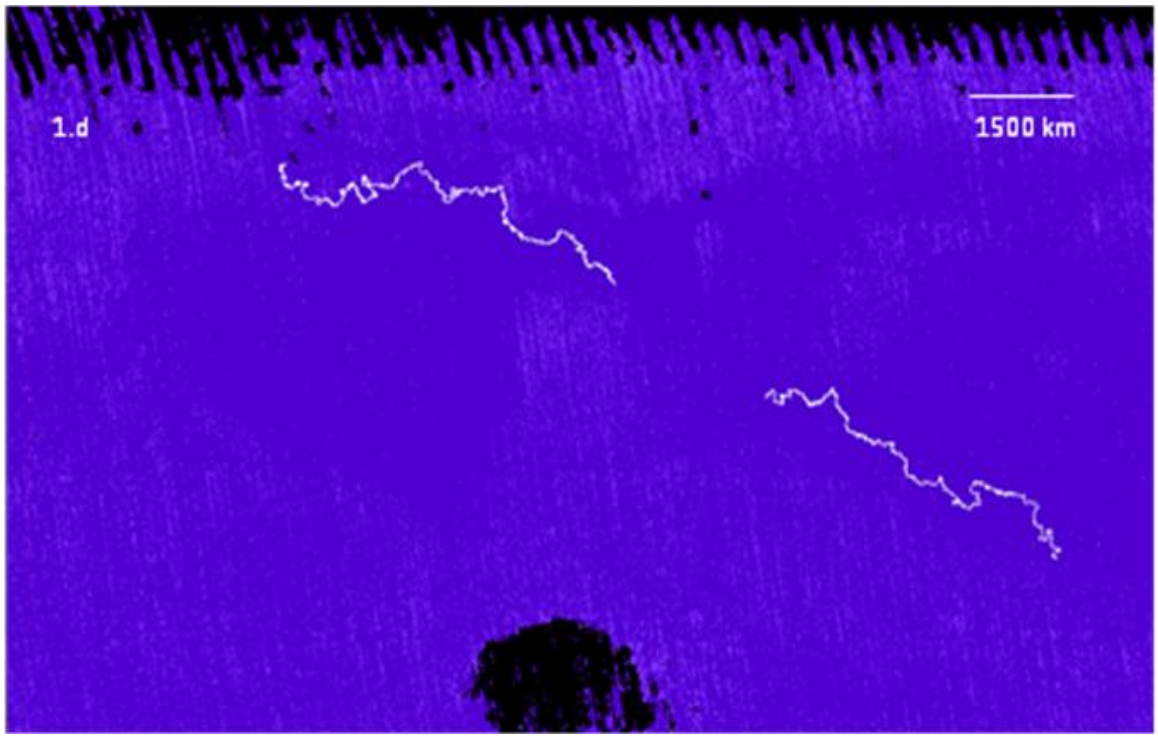

Figure 23. (Group 1c-d) Bowen's discontinuous reaction series including quartz acquired from TES mineralogical data: (1c) amphibole; (1d) quartz. White line delineates global escarpment. Images from Arizona State University, Mars Global Data Sets (2006).

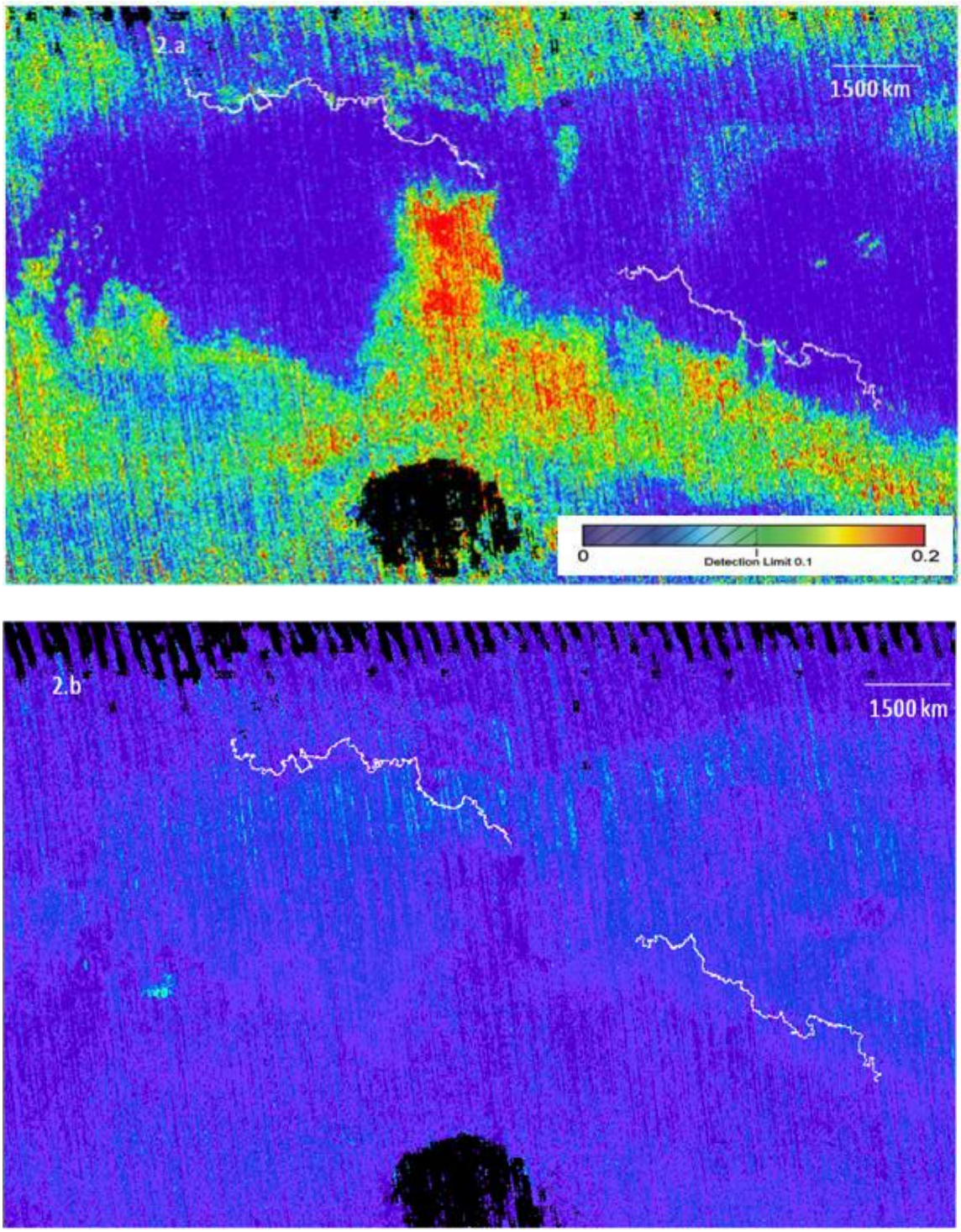

Figure 23. (Group 2a-b) Bowen's continuous reaction series including hematite acquired from TES mineralogical data: (2a) plagioclase; (2b) feldspar. White line delineates global escarpment. Images from Arizona State University, Mars Global Data Sets (2006).

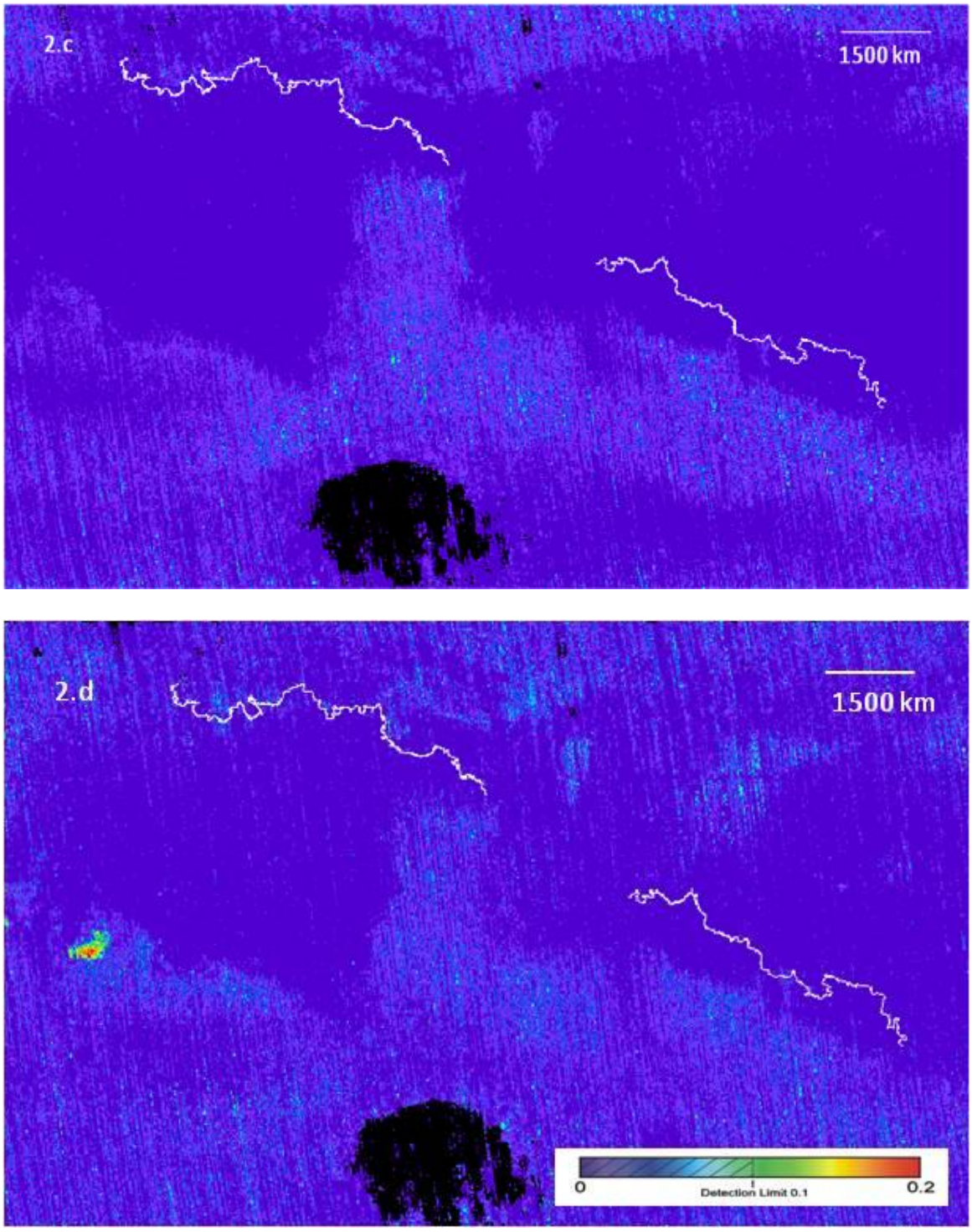

Figure 23. (Group 2 c-d) Bowen's continuous reaction series including hematite acquired from TES mineralogical data: (2c) orthoclase; (2d) hematite. White line delineates global escarpment. Images from Arizona State University, Mars Global Data Sets (2006).

Sectional Analysis

Sectional scale constitutes landscape sizes that are between 50 and 500 km. Analysis of these areas include the initial break in the escarpment and the fretted terrains located up to 300 km away. The fretted terrain was split into two corresponding sections as was the escarpment due to elevation differences for future orogenic and evolutionary analysis. Along the escarpment boundary and the first tier of northern fretted blocks there are deep valleys/fractures with depths reaching 1 km and a strong linear orientation between the long axis of the blocks and the escarpment is present. The northern low fretted terrain blocks show no preferred orientation of the long axis as opposed to the escarpment boundary (Table 5).

Table 5. Analysis of fretted terrain composed in ArcGIS 9.2

Northern fretted polygons						
	length (km)	width (km)	perimeter (km)	area (km²)	length vs. width	azimuth
average	15.24	5.17	42.33	141.49	4.48	91.90
maximum	139.68	49.20	537.96	5246.87	49.67	180.00
minimum	1.95	0.46	8.78	1.33	1.01	0.16
distance from escarpment (km)	0-50	0-100	0-150	0-200	0-250	0-300
average total area(km²)	331.64	195.61	173.95	160.48	153.36	149.80
# of total polygons	119.00	275.00	381.00	449.00	490.00	514.00
% of polygons	20.84	48.16	66.73	78.64	85.81	90.02
	0-50	50-100	100-150	150-200	200-250	250-300
average area in buffer zone (km²)	331.64	92.38	121.14	80.56	79.93	77.06
# of polygons in buffer zone	119.00	156.00	106.00	68.00	41.00	24.00
Northern low fretted polygons						
	length(km)	width(km)	perimeter(km)	area (km²)	length vs. width	azimuth
average	22.18	8.67	67.70	355.45	3.20	103.26
maximum	143.48	58.85	721.40	10418.30	12.54	178.88
minimum	2.48	0.66	7.62	3.19	1.01	0.30
distance from escarpment (km)	0-50	0-100	0-150	0-200	0-250	0-300
average total area(km²)	887.97	597.94	441.99	378.95	367.29	362.95
average total area(km²)/ without largest block	506.75	352.43	275.72	257.99	270.65	282.50
# of total polygons	26.00	45.00	61.00	84.00	105.00	126.00
% of polygons	19.70	34.09	46.21	63.63	79.54	95.45
	0-50	50-100	100-150	150-200	200-250	250-300
average area in buffer zone (km²)	887.97	99.22	126.15	211.74	320.67	341.22
# of polygons in buffer zone	26.00	15.00	20.00	23.00	21.00	21.00

These fretted valleys have flat lying bottoms that are composed of lineated valley fill along most of escarpment (Lucchitta 1984). The northern fretted blocks also show signs of some extensional processes with an average length vs. width ratio of ~4.5 and a logarithmic trend of decrease in the size of the blocks traveling from south to north. The northern low fretted blocks are on average more than twice the size of the northern blocks and show less if any signs of extensional processes with a length to width ratio of ~3 along with a logarithmic trend of decrease in the size of the blocks (Fig. 24).

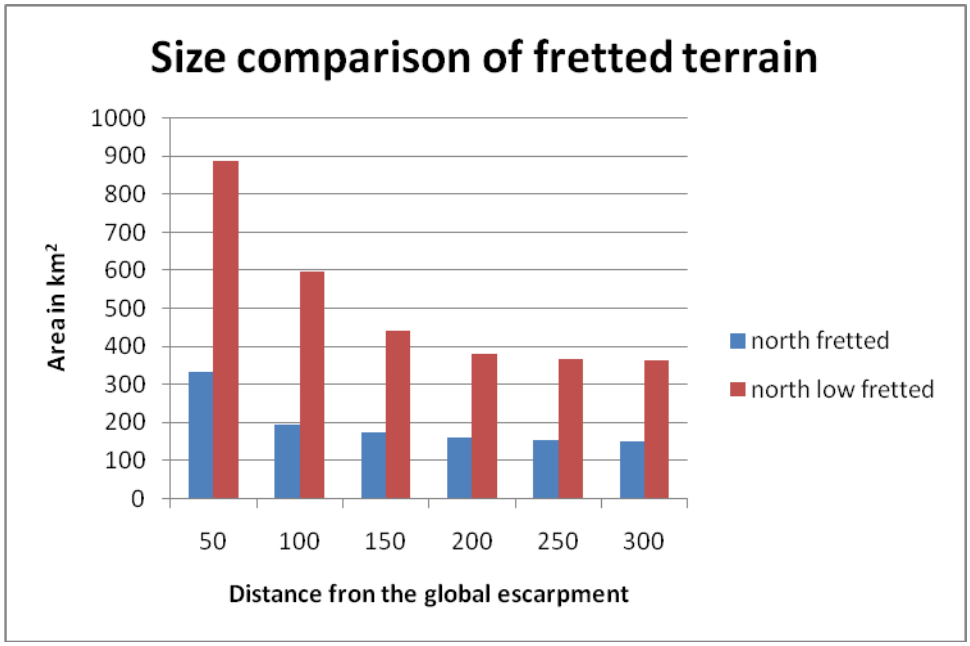

Figure 24. Chart showing size distribution on both classes of fretted terrain (Data from table 5).

Debris aprons located on the global escarpment and around the 1st tier of the northern fretted blocks are generally steep (>30%) and small. Farther from the escarpment to the north, these aprons become more shallow in angle of repose (<30%) and are much more pronounced and encompass a greater area than the 1st tier blocks (Fig. 25). Conversely, almost all of the northern low fretted blocks have broad, low angle aprons that in some places overlap one another. The transition from blocky to knobby material becomes evident around 100 km from the escarpment.

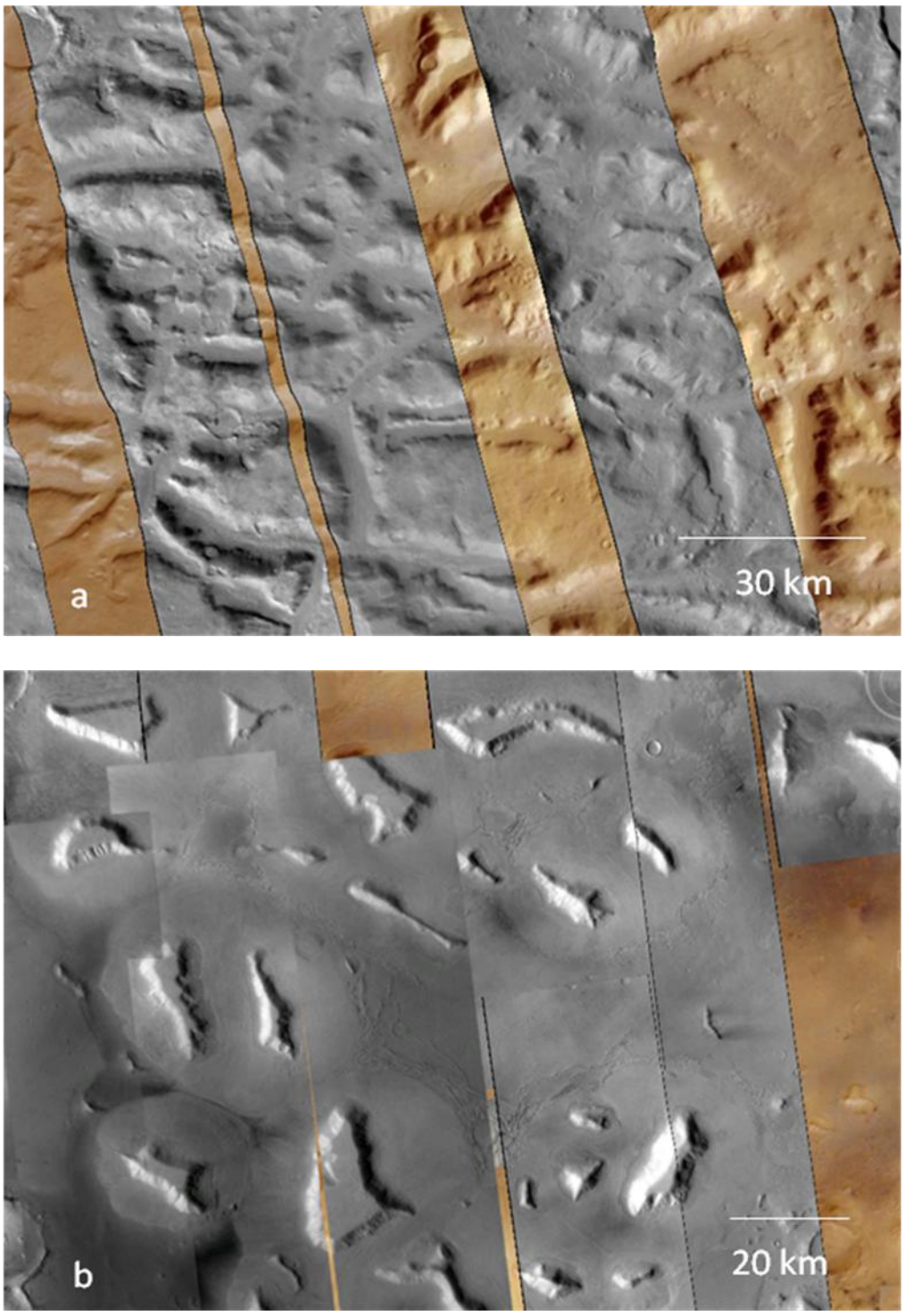

Figure. 25. Mosaic of CTX images composed in Google Earth 5.0: (a) examples of northern fretted blocks < 50 km from escarpment; (b) examples of northern low fretted blocks > 200 km from escarpment. Images from Arizona State University, Context Camera Images (2007 – 2008).

Mineralogically at this scale, mafic material and oxidized iron minerals are the dominant regime as collected by spectral analysis from CRISM. This material constituted the individual blocks as well as the valley fill. Geomorphologically the blocks show no sign of rotation in any direction (x, y, or z) and some blocks have degraded in situ into multiple blocks. Evidence of fluvial incisions from the southern highlands is found along the entire escarpment, but their sinuous nature ceases along the boundary line (Fig. 26). The northern low polygons seem to be associated with multiple impact structures that dominate the area instead of the northern polygons which follow a fault/fracture pattern.

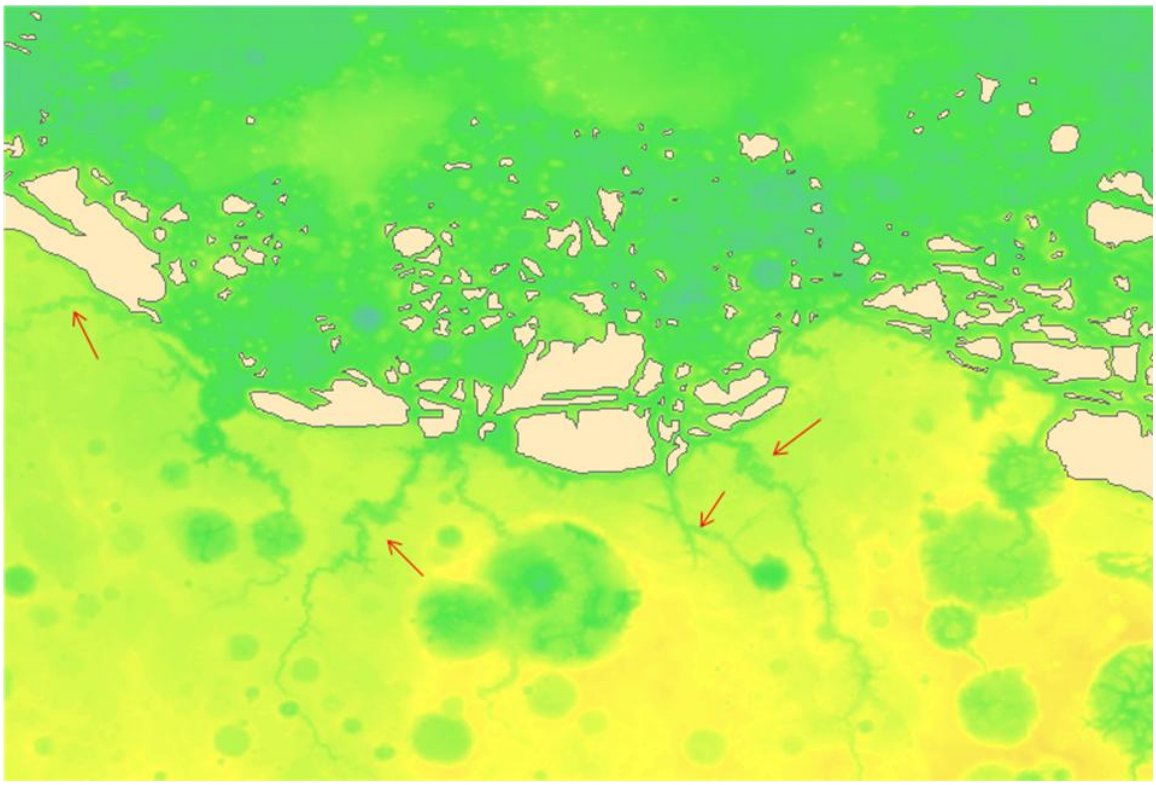

Figure 26. Sinuous nature of fluid transport along the northern global escarpment. Modified from USGS MOLA DEM (1999); northern fretted terrain – beige blocks; red arrows – areas of fluid incision.

Local Analysis

Local scale involves any section/area that is smaller than 50 km. Major geologic and geomorphic differences can be seen at this resolution. Geologically, individual CRISM images show a diverse and constantly changing landscape. While the tops of the blocks are predominately mafic, in some the lower lying elevations along parts of the escarpment in the fretted valleys a variety of minerals including iron, iron oxides, olivine, pyroxene, Fe/Mg phyllosilicates, and clays can be found. In situ weathered rock and regolith so close in proximity to one another provides evidence of continual mass transport and altering of sediment in the more recent Martian past (Fig. 27). In regions greater than 30º latitude, sources of water bound ices can be found as well.

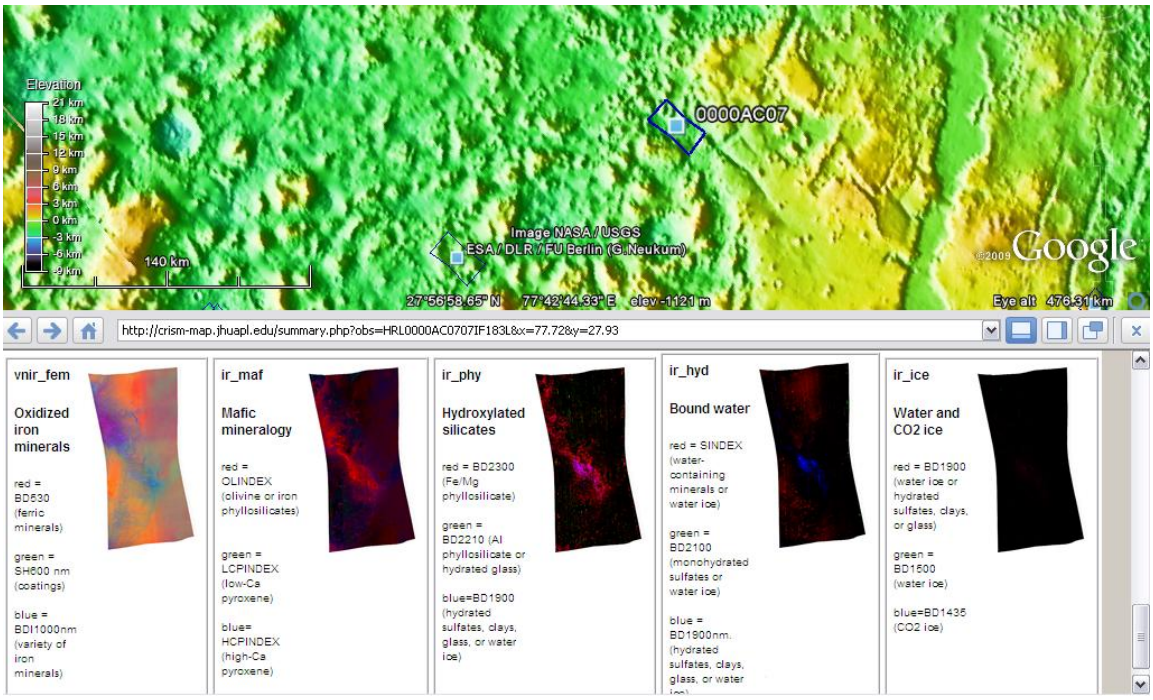

Figure 27. CRISM image 0000AC07 from Google Earth 5.0 showing varied mineralogy found in the fretted valley regions. Images from Arizona State University, CRISM Images (2008).

Investigation of geomorphology also provides insight into the constantly changing landscape. Multiple episodes of more recent slumping/mass wasting can be seen on the flanks of many fretted blocks (Fig. 28; NASA 2010e:PDS).

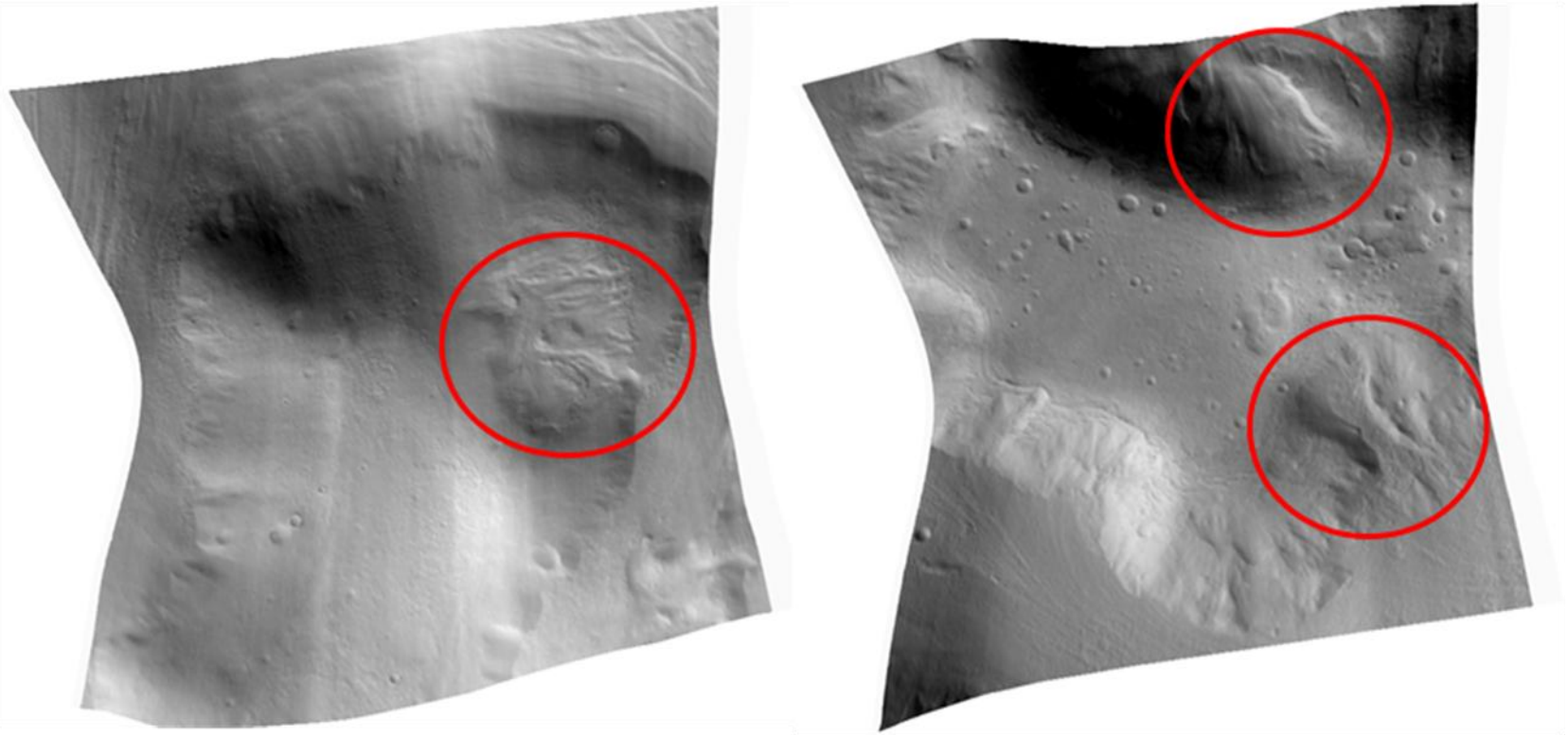

Figure 28. CRISM images 0008986 and 0009605 showing mass wasting/ gravity driven processes along the margins of the fretted blocks. Images from NASA 2010e Planetary Data Systems (PDS; 2006).

Evidence of lineated valley fill is visible in many of the fretted valleys. The current theories that address the formation of these features are: (1) mobilization of ice-rich regolith due to sublimation; and (2) glacial moraines (Carr 1996; Fig. 29). Possible scenarios will be addressed in the discussion section.

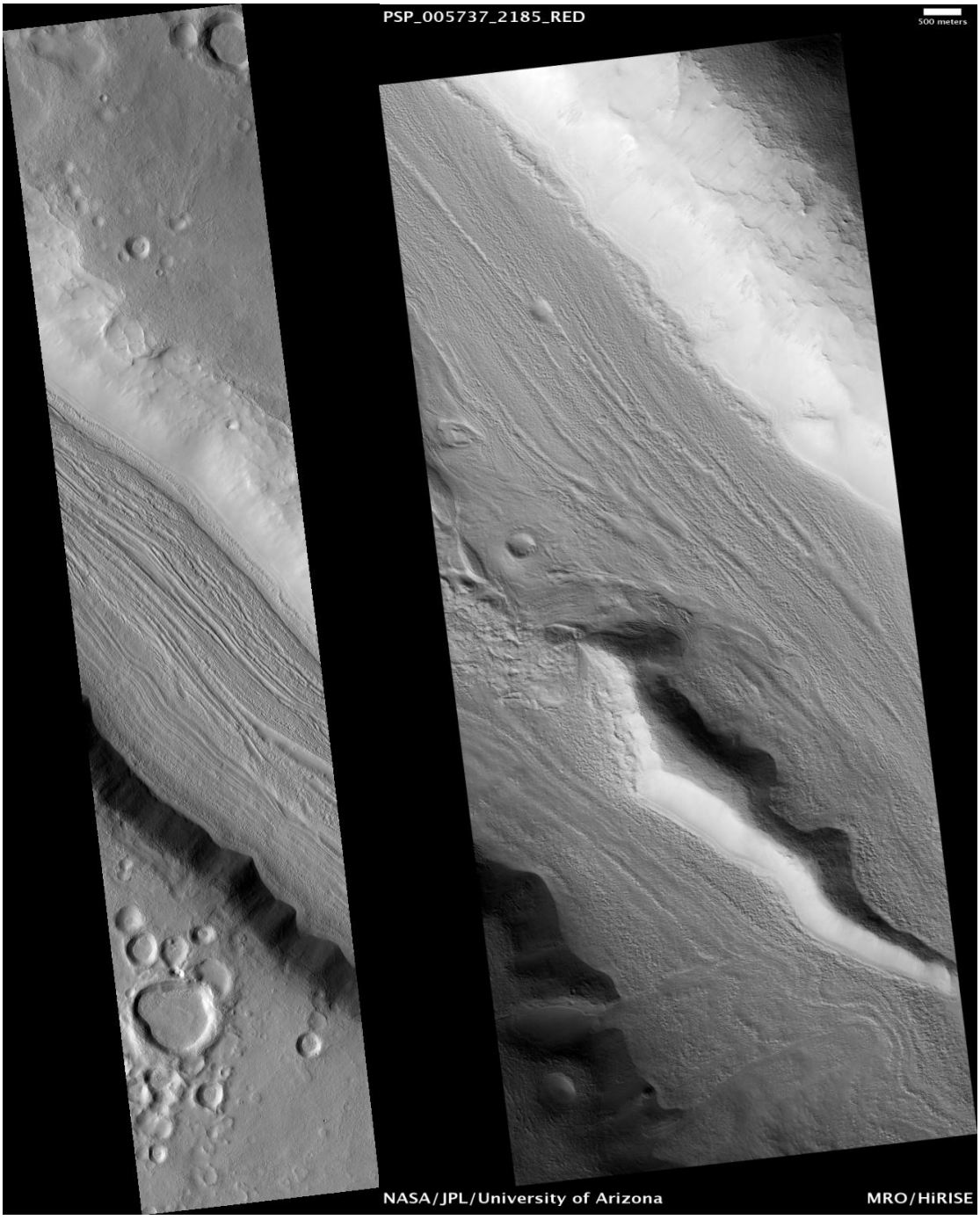

Figure 29. Example of HiRISE images showing lineated valley fill found between fretted blocks. HiRISE image 005737 from Arizona State University (2007).

INTERPRETATION AND DISCUSSION

Mars is a planet that is encircled by a hemispheric dichotomy that has been dated using crater counting techniques to be between 4.1 and 3.9 billion years old (Watters et al. 2007). The northern lowlands comprise roughly 1/3 of the planet's surface and are on average 4 km lower in elevation than the southern highlands (Watters et al. 2007). The crust is about 25 km thicker in the southern highlands and this buoyancy is expressed as higher elevation topography (Aharonson et al. 2004). The expression of these elevation differences can be compared to the Earth's continents and the ocean basins, however spatial consistency is not found along the entire escarpment that encircles Mars. An abrupt 1 km vertical change which is dominantly in the form of a steep scarp is located west of Isidis (280º to 350º) and varies greatly from the same 1 km elevation change in Arabia Terra region (350º to 30º) which can sprawl for almost 1,000 km horizontally. Many geologically complex features can also be found along the transition zone between the southern highlands and the northern lowlands. In the eastern hemisphere, fretted and knobby terrains (mesas and knolls) are located along the boundary and stretch for 100's of km in some areas (Sharp 1973). Endogenic or exogenic processes are the two main competing hypotheses for the formation of the global escarpment. One of the problems with testing either of these theories lies in the fact that 30% of the boundary has been covered by more recent Tharsis volcanism (Andrew-Hanna et al. 2008). Other assessments involve resurfacing of the northern basin after the formation of the

dichotomy. These would include either volcanic and/or sedimentary processes that continue to be active on Mars to the present day.

Endogenic processes

Endogenic or internal processes comprise any mode that involves convection to some degree that would be driven by heat, pressure, composition, and viscosity - along with others constituents. These processes invoke no outside sources of energy that would be considered extraterrestrial in origin. Models are one of the best ways to study and interpolate these alterations in the early crustal formation history of Mars. The two main hypotheses that introduce these mechanics are degree-1or long-wavelength mantle convection and plate tectonics. Remote sensing information gathered by past and current satellites has added additional data to these theories. The composition of Mars is critical in the understanding and analysis of these internal processes (Fig. 30).

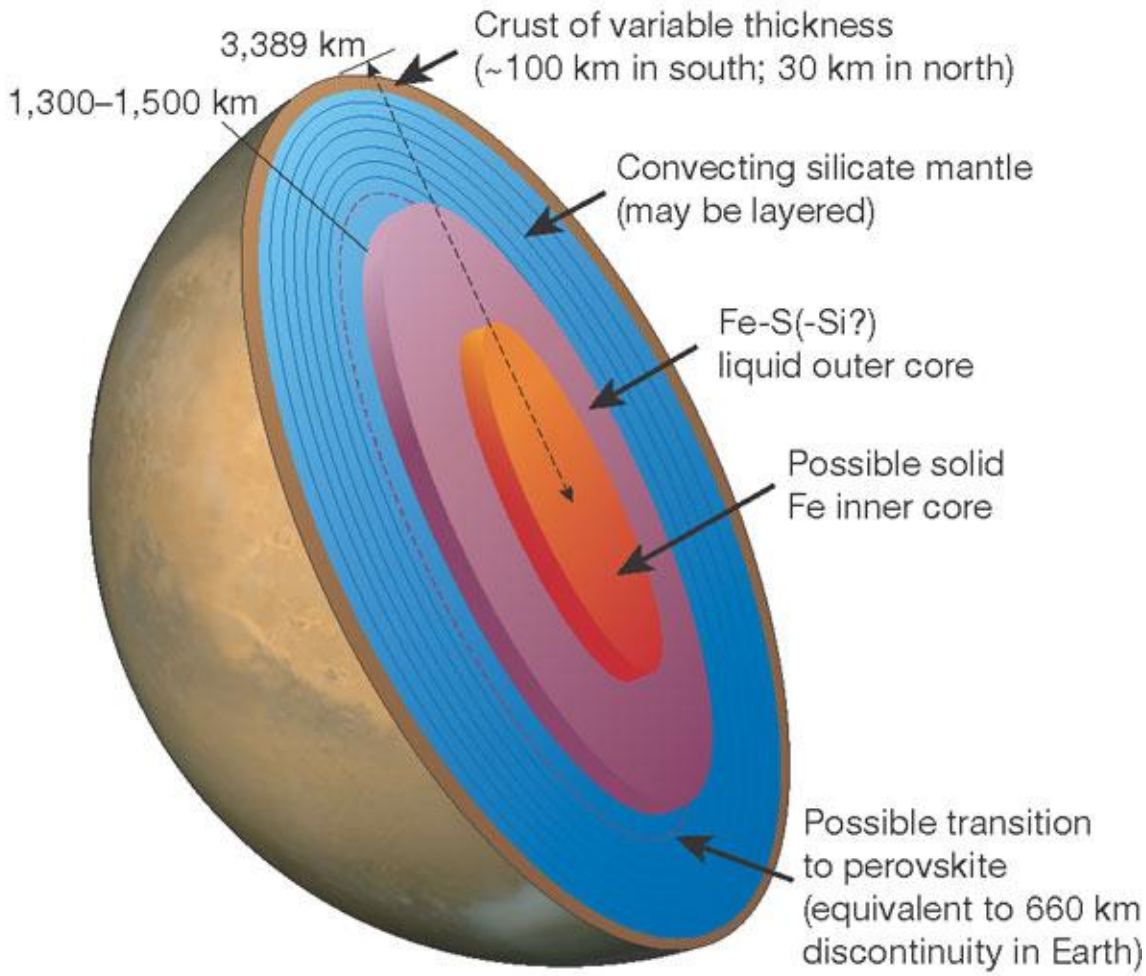

Figure 30. One possible view of the Martian interior. From Stevenson (2001).

Remnant magnetism present in the crust reveal a primitive dynamo that persisted for approximately 0.5 billion years early in Martian history (Williams and Nimmo 2004). The presence of an active dynamo and the convection driven in the core can be explained by two processes. Either the initial Martian core was substantially hotter than the over lying mantle, due to radioactive decay of K^{40}, U^{235}, U^{238}, and Th ^{232} and the presence of sufficient sulfur, or a rapidly cooling mantle due to the size of Mars were the driving forces behind this heat flux (Williams and Nimmo 2004). If the SNC meteorites are from

Mars, then an estimate of 14% sulfur for the core is determined which would allow for a partially molten core to persist for upwards of 1 billion years (Boyce 2002).

Degree-1 mantle convection

Degree-1 mantle convection models are one way to study and assess large scale, single hemispheric anomalies (Zuber et al. 2001). The Martian dichotomy and the Tharsis volcanic rise are two examples of such structures (Harder and Christensen 1996). Past modeling studies have suggested that there is a viscosity increase in the lower mantle on Earth (Hager and Richards 1989) so the same approach is used when modeling the early Martian interior.

Zhong and Zuber (2001) demonstrate that by altering the viscosity of a layered mantle that long-wavelength patterns are produced using Rayleigh-Taylor instability analysis and finite element convection models. At the end of planetary accretion process, a high thermal gradient could be found between the core and mantle producing a low viscosity layer at the base of the mantle which could lead to a single, hemispheric super plume (Ke and Solomatov 2006).

There are three scenarios for degree-1 mantle plumes to form the dichotomy. The first example is directly after the main accretion phase of the planet where no substantial crust has formed. A single plume forms above the solidus phase and then extruded to form new crust (Roberts 2004). The second example consists of a stagnant lid with a uniform >50 km thick crust to form on the planet. An upwelling mantle plume would erode away or undercut the crust and redeposit the material above the down welling fringe (Wise et al. 1979ab). Finally the last scenario is a similar combination of the first two examples. A degree-one mantle plume would cause a thickening of one hemisphere

due to upwelling and consequentially producing a thinner opposite hemisphere due to relaxation of the overlying crust (Zhong and Zuber 2001; Fig. 31).

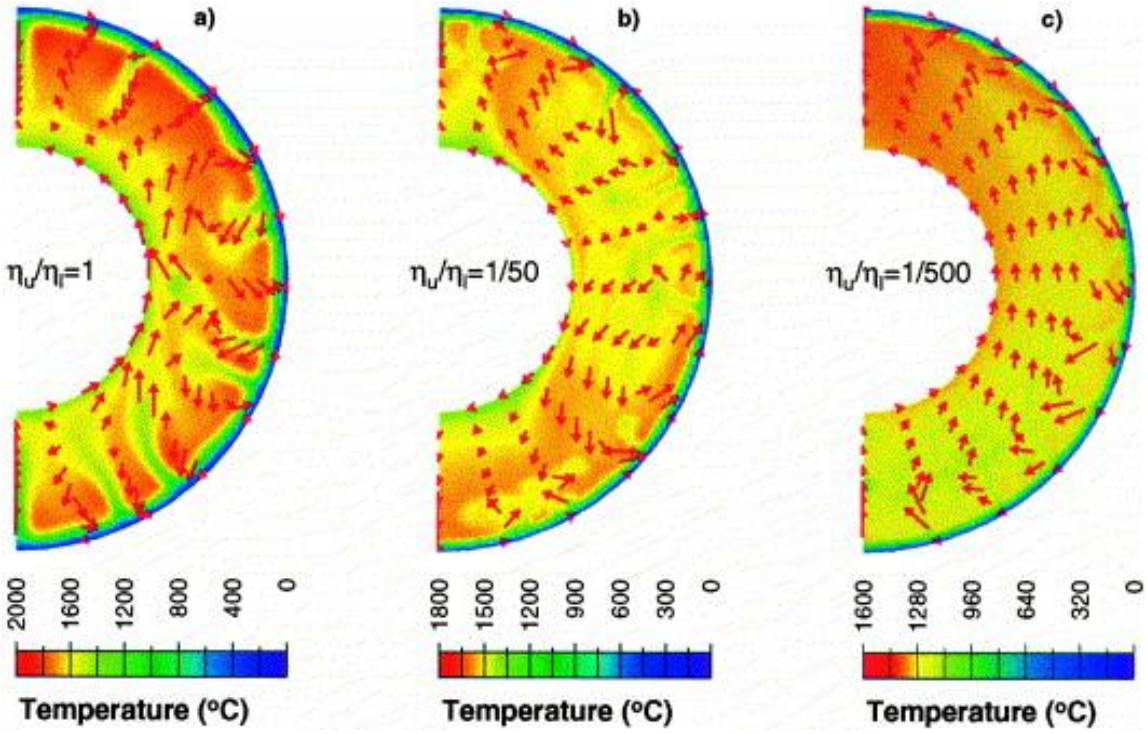

Figure 31. Example of Rayleigh-Taylor instability analysis with 3 differing viscosities. Radius to initial boundary is 1,325 km with an 80 km thick lid. From Zhong and Zuber (2001).

Rock rheology is the driving force for any internal process of a planet. If the Martian mantle/core boundary is located around the γ-spinel to perovskite boundary, the time range for a degree-1 convection cell to form exceeds 2 billion years using a finite element model with an endothermic phase change (Harder and Christensen 1996). Breuer et al. (1998) used many exothermic phase reactions at the olivine-spinel transition with lowered pressure and free slip boundary conditions, but with the introduction of temperature dependant viscosity the age for a single convection plume to form exceeds 4.5 billion years. Clearly there are timing issues with this model since the global

escarpment is ~ 4 billion years old. Other models composed by (Roberts and Zhong 2006) show that with a layered mantle, viscosities can differ by >100 times and the resulting mantle plume can develop on a time scale of 100 million years.

Varying models show that a degree-1 mantle plume can form a hemispheric dichotomy that is present on Mars today. However many assumptions in composition, depth, and viscosity have to be inferred. Problems are invoked when we look at the crustal thickness of Mars (Fig. 32).

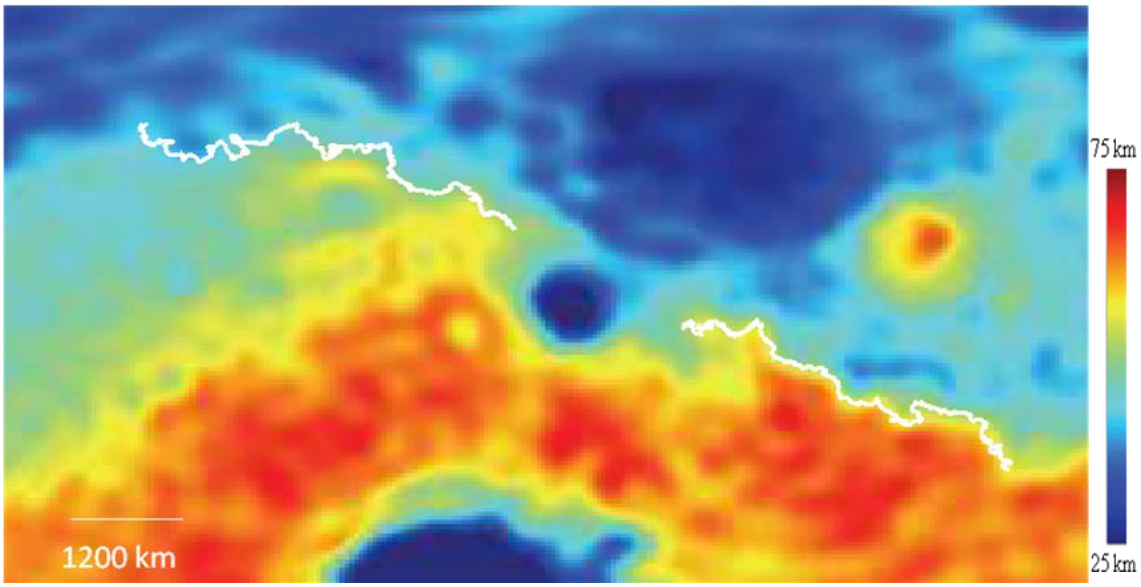

Figure 32. Modeled crustal thickness map (0.5 pixel/degree). White line delineates escarpment boundary line. Image modified from Andrews- Hanna et al. (2008).

The first example for degree-one mantle convection proposes that the entire southern hemisphere was formed by a single upwelling. As magma was extruded to form the primordial crust, there should have been a gradual thickening of the crust toward the center of the plume with a waning in thickness as you move toward the outward extent of the plume resulting in a lens shape. Clearly there is a distinct difference in crustal

thickness as traced by the steepest slope path of the escarpment ranging from 75 to 30 km thick in just a few 10's of kilometers contradicting a lenticular shape.

The second example inversely states that the plume scoured or undercut the northern hemisphere crust and redeposited the material at the edge of the plume. If this were the case (see Fig. 32), we would expect to see the thickest portion of the crust on the southern side of the escarpment due to accretion. The fretted terrain could be a remnant of this condition due to crustal collapse at the escarpment boundary, but does not explain how these mesas and knobs extend for 100's of kilometers northward. The fretted blocks are not tilted toward the northern basin as you would expect if there had been crustal thinning and collapse along the escarpment.

The last example provides evidence of thickening and thinning of both hemispheres simultaneously. Extremely high viscosities are needed at the mantle/core boundary for such a large scale feature to be produced. Although the strong difference in crustal thickness along the escarpment along with the horizontality of the tops of the fretted blocks would contradict such an outcome.

Another problem that arises is the fact that any type of degree-1 mantle plume could not produce such a lengthy, steep, stable cliff like the global escarpment that would have a life span of more than 4 billion years. Presently there is only one way to produce such a structure of this magnitude and that is through plate tectonics. Lastly and taking into account Andrews-Hanna's model (Fig. 8) of the global escarpment before the Tharsis rise was present; we can see a distinct elliptical shape which could not be produced by mantle convection alone (Kiefer 2008). Degree-1 mantle plumes are not symmetrical and would produce finger-like patterns on the outer fringe which do not

match the approximate linear pattern that we see in the crustal thickness of today (see Fig. 10).

Plate Tectonics

The other endogenic process that could have produced the Martian dichotomy would be plate tectonics. This ongoing process on Earth creates new crustal material at spreading centers and subducts older crustal material to maintain isostatic equilibrium (Fig. 33). Convection processes from the mantle driven by heat loss and the change in density of the newly formed plate over an extended period time are the driving force behind plate movement (Bercovici 2003). Plate tectonics is an effective process for mantle cooling and would help drive an early dynamo (Nimmo and Stevenson 2001).

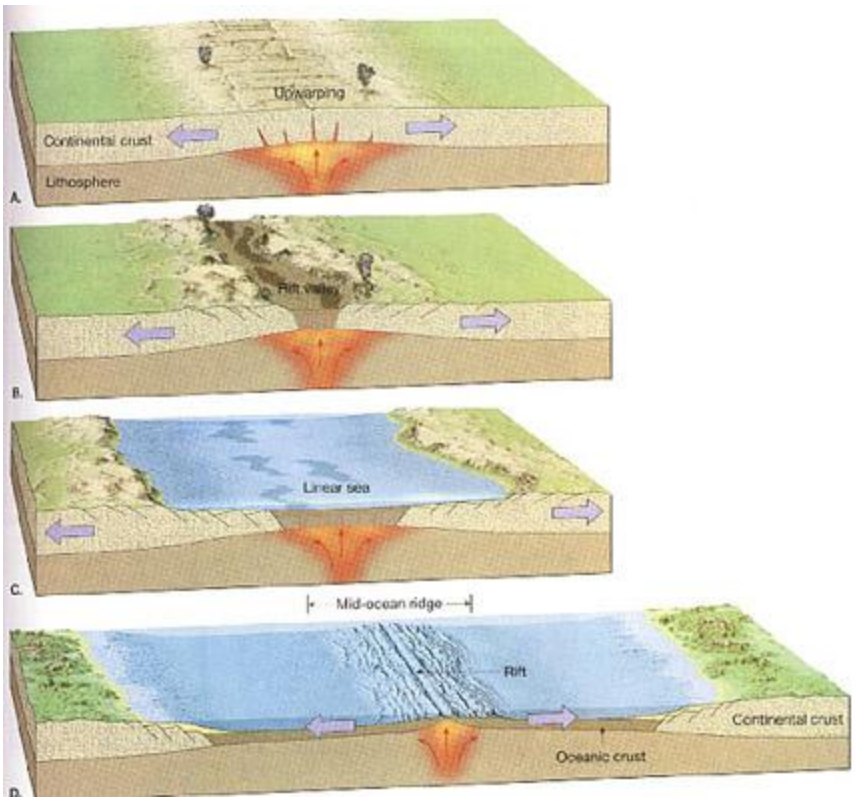

Figure 33. Picture depicting sea floor spreading through time A-D, which produces a steep terrace. From Scienceray (2010), Great discoveries in the field of Earth science. <http://scienceray.com/earth-sciences/great-discoveries-in-the-field-of-earth-sciences/> (Accessed: 24 May 2010).

On Mars, older, marginal crust would have been subducted, while a process akin to terrestrial seafloor spreading would have produced the younger northern lowlands in the early Noachian (Sleep 1994). The expression of this activity would be a relatively symmetrical crustal thickness across the northern basin with a gradual thickening at the escarpment boundary with an abrupt change around the subduction zone/continental margin which is seen in Figure 33. However, there are fallacies in this theory as well.

The northern basin on Mars is approximately 8,500 km wide and 10,600 km long and covers 40% of the planet's surface (Andrews-Hanna et al. 2008). Using maximum spreading rates on Earth, it would take 100's of millions of years to produce such a basin

by this process. Comparison of the density of quasi-circular depressions (QCD) contradicts this spreading motion (Frey 2004). Mars is smaller than Earth and would have cooled more rapidly. If plate tectonics were to have happened on Mars, it would have been brief. It is unclear if mantle convection could cause subduction of a crust 50 km thick because the basalt-eclogite phase transition does not occur until a depth of ~200 km (Zuber et al. 2000). Other discrepancies are there is no evidence of any large, relic subduction zone either along or near the escarpment which would constitute orogenic morphologies including trenches, mountain chains, or major rifting zones (Watters et al. 2007).

Exogenic processes

External or extraterrestrial processes could have formed the global escarpment. Excavation and ballistic projection of material due to an impact can form a steep cliff in the embodiment of a crater wall. At the end of planetary formation, it is estimated that the inner solar system was populated by ~20 Mars to Moon sized objects (Kominami and Ida 2002). Multiple planetesimals could have shared the same orbit at differing Lagrangian points similar to the Trojan asteroids located in orbit around Jupiter (Freitas and Valdes 1980). Eventually these orbits become unstable and either a catastrophic collision or ejection from the inner solar system will occur. The current hypothesis about the Earth-Moon system is thought to be a collisional event that tilted the Earth's axis to its present orientation. The major accretionary process for the inner planets ceased at the end of the heavy bombardment ~3.8 billion years ago (Gomes et al. 2005). The proximity of Mars to Jupiter and the asteroid belt make it a likely candidate for a greater density of large impacts.

Multiple impacts

Unlike endogenic processes, impact models do not have a problem with time constraints. Using crater counting techniques, we know that the global escarpment predates the end of the heavy bombardment era (Frey and Schultz 1988). Evidence of this catastrophic event can be seen on all the objects in the inner solar system. The close proximity of Mars to the asteroid belt and the large gaseous planets made it a prime target for collisions.

Tracing the transition zone between the southern highlands and the northern lowlands using topography and crustal thickness models we see the dichotomy is irregular and not circular in shape lending that a single impact was not the source (Zuber et al. 2000). Multiple large impacts would provide an alternative answer for the irregular shape of the northern basin.

Impact craters of considerable size (>200 km) would leave a considerably high topographic rim compared to the surrounding relief, yet there is no evidence of this in the northern basin using MOLA data (Fig. 34 a). A good example of one of these structures is the Utopia basin which is ~3,000 km in diameter, but has no relic crater rim (Fig. 34 b). For this to be plausible, more than 2 km of sediment would have to fill the entire northern basin to subdue this topography (McGill and Squyres 1991). Later volcanism has resurfaced the northern basin in the past, but there is no evidence of a long, sustained era in which kilometers of flow which is needed to erase impacts of this magnitude.

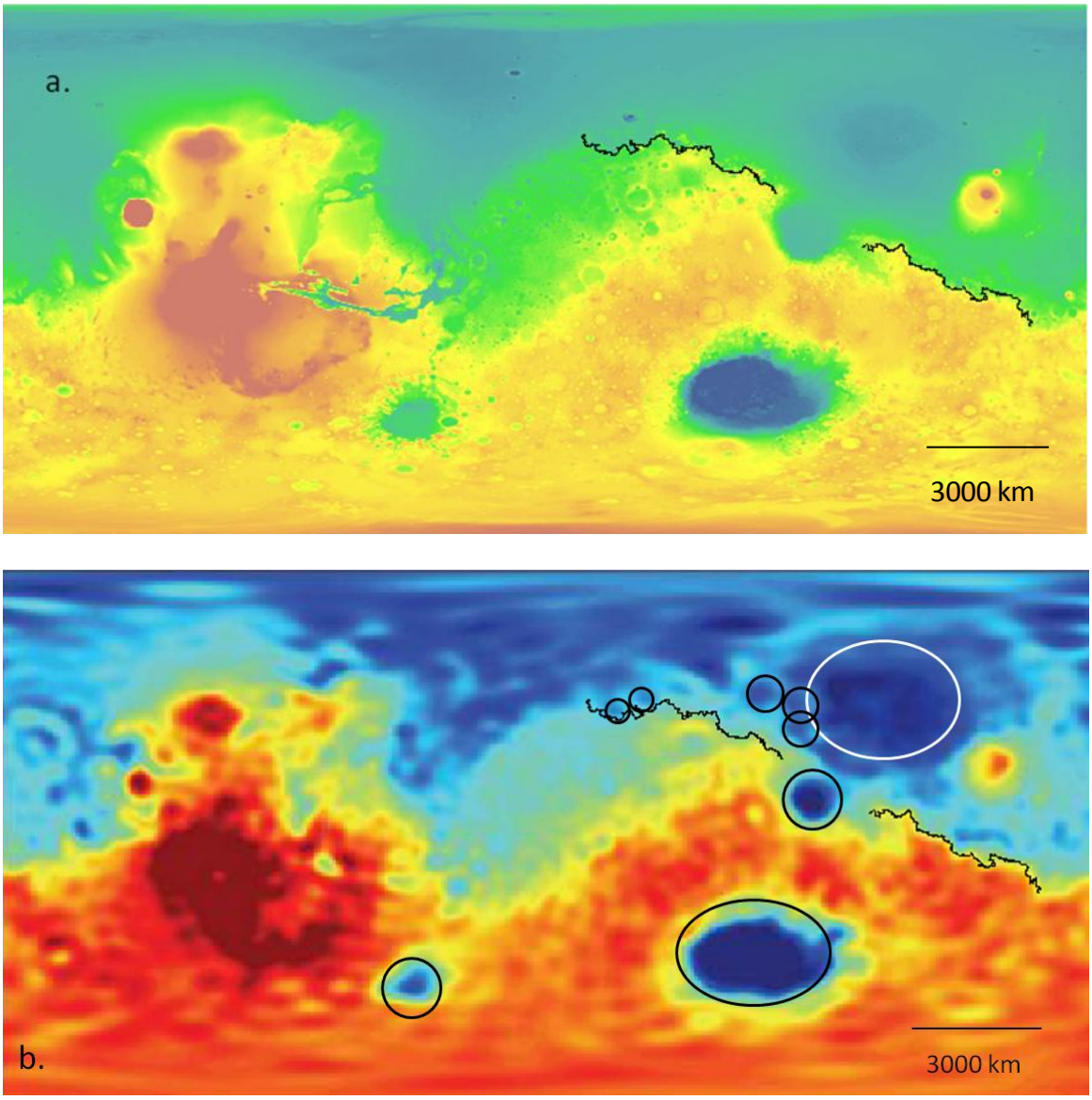

Figure 34. Topographic and Crustal thickness maps: (a) MOLA relief map, Black line is traced escarpment; (b) crustal thickness map, Black line is traced escarpment; White ellipse is Utopia impact site: Black ellipses mark sites of major thinning due to other impacts. Images were modified from USGS MOLA DEM (1999) and Andrews- Hanna et al. (2008).

Furthermore, it would take many Utopia scale impacts to account for the amount of material that is missing from the basin. Not only is it unlikely that a cluster of large bolides preferentially struck one hemisphere of Mars, but there are no structural features to affirm this claim. These features would include crater rims, concentric radial fractures,

and overlapping ejects blankets (Frey and Schultz 1988). While multiple impacts could have produced some of the escarpment, crustal thickness maps shed doubt on the scenario for the total escarpment formation (Fig. 34).

Single impact

Large impacts are common throughout the solar system. Almost any terrestrial body demonstrates these features including Mercury, Mars, the Moon, and many of Jupiter's and Saturn's moons (see Table 4). The inner solar system was cluttered with at least 20 Mars- or larger size bodies during the early Noachian era (Kominami and Ida 2002). This provides a basis on which assumptions of mega-impacts can be inferred. Again, the Earth-Moon theory is thought to be one such impact.

Wilhelm and Squyres (1984) first proposed that a single giant impact could have formed the northern basin on Mars. Since that time, the shape of a non-circular corresponding global escarpment has led to question that theory. With a better understanding of impact events, we now know that impacts can be circular or elliptical depending on the angle of entry. There are several examples of elliptically shaped impact basins on Mars and other planets.

Andrews-Hanna et al. (2008) modeled the crustal thicknesses of Mars extracting the mass of the Tharsis rise to view the dichotomy before its emplacement. By comparing his results with other accepted elliptical basins found in the solar system, definite similarities arise (Fig. 35).

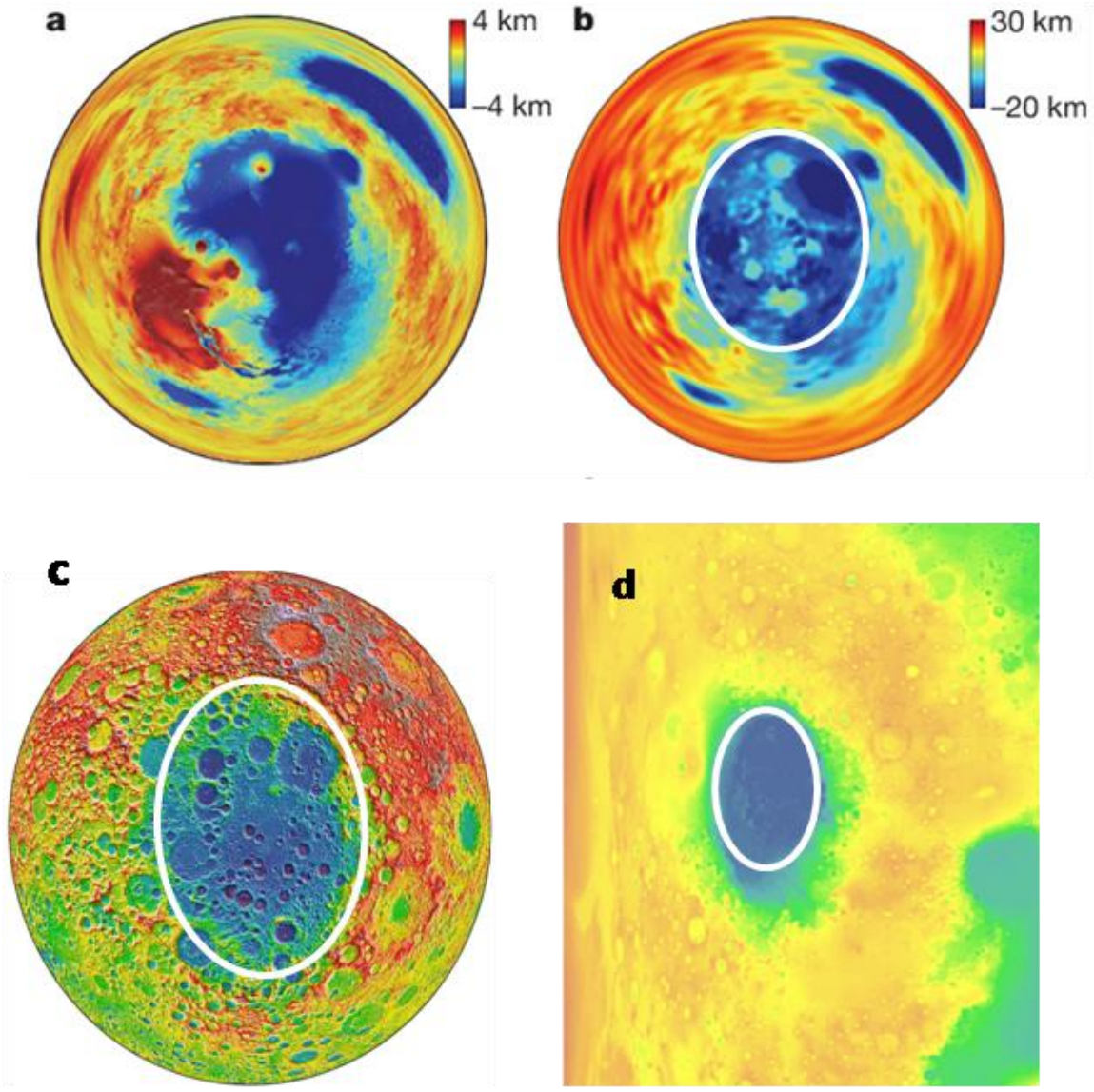

Figure 35. Comparison of three major elliptical basins: (a) northern polar projection of Martian topography; (b) modeled crustal thickness of Mars removing the Tharsis rise; (c) topographic polar projection of the South-Pole Aitken basin on the Moon; (d) the Hellas basin on Mars. Modified from Google Earth 5.0, USGS MOLA DEM (1999), and Andrews-Hanna et al. (2008).

The ratios of major to minor axis for these 3 major impacts from figure 35 are: (1) Borealis basin 10,600/8,500 km = 1.25; (2) South Pole-Aitken basin 2,125/1,542 km = 1.38; and (3) Hellas basin 2,414/1,820 km = 1.33. Any deviance from a true elliptical shape can be attributed to tectonic activity, later impact overprinting, and/or local erosion

(Andrew-Hanna et al. 2008). There are confirmed partial ring structures associated with the South-Pole Aitken basin and Hellas. With this in mind, the fretted terrain could be a partial relic ring structure. Timing is not issue with of a single impact as there would be for any endogenic process. Because the formation of the global escarpment predates the end of the heavy bombardment, it could have been modified by other later impacts thus a uniform basin thickness would have been altered as well. With an oblique impact of this size, the resulting crustal removal would blanket the entire planet and the melt would be largely contained in the transient crater (Marinova et al. 2008). Since the majority of the energy would be expelled in the form of ejecta due to a low angle impact, the entire surface of the planet would not melt and hence leave evidence of such an event (Hart et al. 2007). Even at an oblique angle of entry, such an impactor should produce a partial multi-ring structure. Again, a remnant of this could be the fretted terrain that borders the global escarpment (Fig. 36).

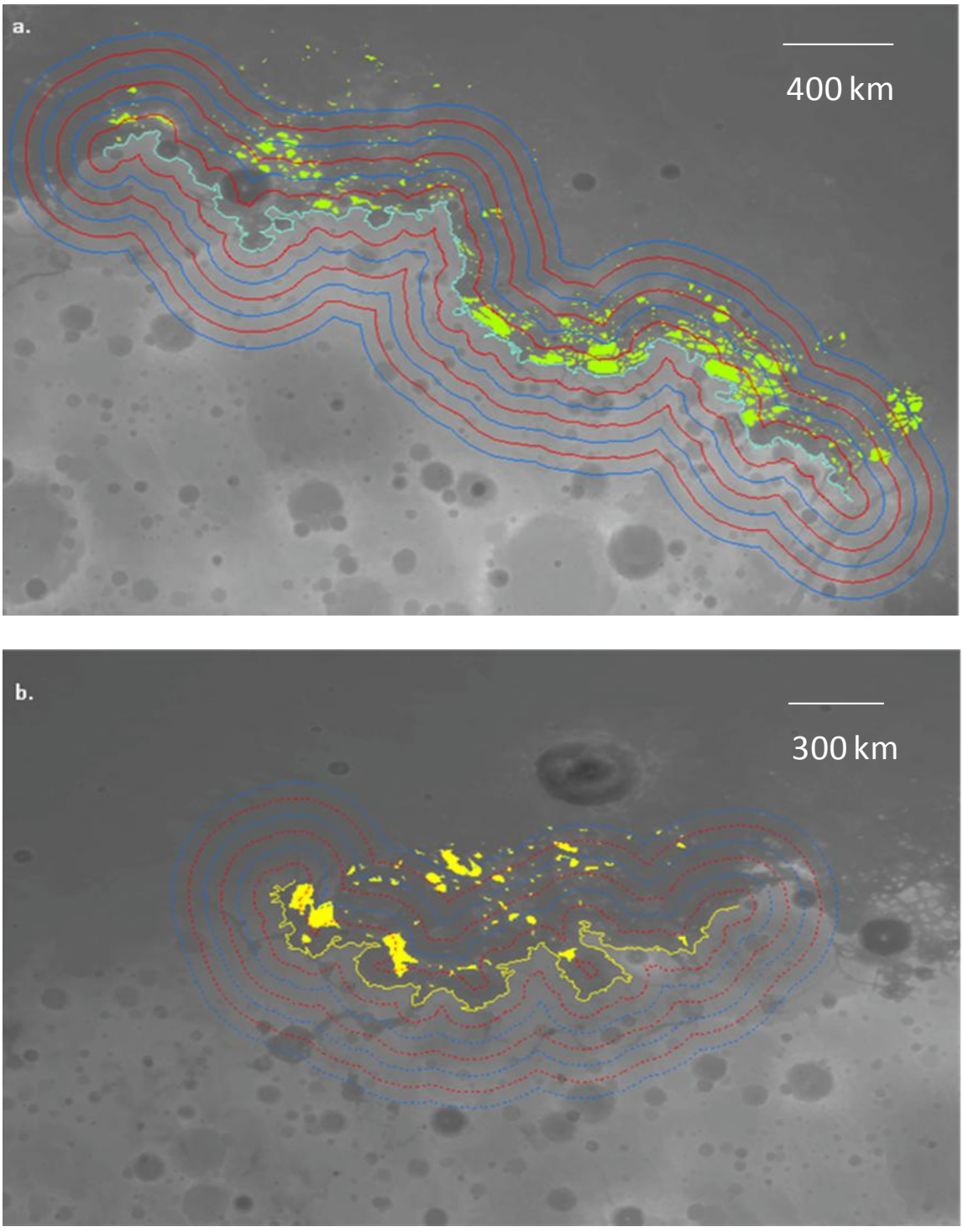

Figure 36. MOLA greyscale scale DEM: (a) northern escarpment - light blue line, 50 km buffers - red and blue lines, fretted terrain - green polygons; and (b) northern low escarpment - yellow line, 50 km buffers - red and blue dashed line, northern low fretted terrain - yellow polygons. Modified from USGS MOLA DEM (1999).

An impact of this magnitude would have excavated the entire crust from the area thus exposing mantle material and producing a decompression magma ocean for a period of time. Mineralogical maps derived from TES show a distinct difference in geology between the northern lowlands and the southern highlands. The southern highlands are dominated by basaltic flows, while a higher concentration of andesite is found in the northern basin (see Fig. 22 a-b). This is easily explained if a mega-impact cleaved out the initial crust and was then refilled with underlying mantle material As material resurged into the crater, undercutting of existing crust could have caused a possible rafting effect similar to iceberg calving transporting cohesive blocks for large distances due to density variations between the crust and underlying mantle material (Melosh 1989; Fig. 37).

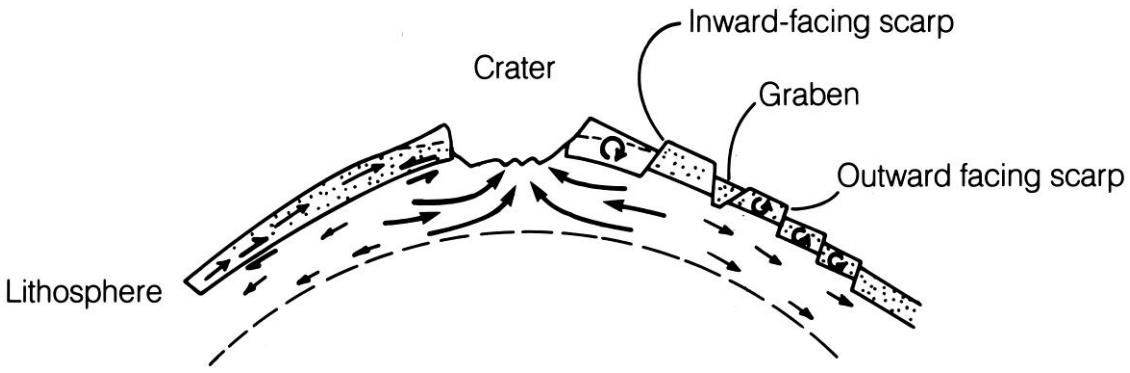

Figure 37. Possible motion of lithosphere and underlying fluidized mantle material during a major impact. From Melosh (1989).

Defining similarities arise when accessing the data acquired during this project. Regarding Figure 36 a, there is a continuous fracture line that runs almost the entire length of the northern escarpment that corresponds to the 50 km buffer zone. All large blocks trend identically to their position on the escarpment. These larger 1st tier blocks are also horizontally equal in elevation with the escarpment with no apparent dip in any

direction. This division could a possible ancient outer ring structure that would coincide with an impact of this magnitude. The thinning of the fretted blocks into knobs traveling northward away from the escarpment would coincide with an inner ring or rings and would have been tilted due to their proximity to the basin (Fig. 37). These inner rings would have been more susceptible to erosional smoothing with the inner peaks rounding over time and potentially filling in the face of the inward facing scarp.

Another possible outcome for an impact of this magnitude would be a large deviance of obliquity in the axis of the planet as compared to the orbital stellar plane. As the large gas giants settled into more stable orbits, some of the remaining inner planets would have been perturbed out of their orbits. These future projectiles could have struck multiple planets including the Earth, Mars, and Neptune which would explain their current axial tilt (Rubin 2002). Mars currently has an axial tilt of ~25º, but it can vary from 18º to 48º over time (Head et al. 2003). One possible mechanism for this large variance would be some time in the early history of Mars, a giant impactor struck the planet, thus tilting its axis and producing such an extreme wobble (Rubin 2002).

Formation and evolution of the fretted terrain

The fretted terrain is the boundary transition zone between the northern lowlands and the southern highlands. It was recognized to cover 3% of the Martian surface and is a product of erosive/abstractive processes (Sharp 1973). The terrain is marked by steep, flat-floor chasms that dissect the blocks which become less abundant the further you travel from the escarpment (Lucchitta 1984). These fretted blocks which resemble mesas and buttes on Earth transition into knobs and knolls northward from the escarpment boundary. The fretted terrain can be found between 280º and 350º longitude plus 25º and

50º latitude (see Fig. 11). Due to the geographic nature of these blocks, two distinct regions were used to assess the nature of the formations. They are (1) the northern fretted terrain- 280º to 325º longitude and 25º to 50º latitude and (2) the northern low fretted terrain- 325º to 350º longitude and 40º to 50º latitude (Fig. 38).

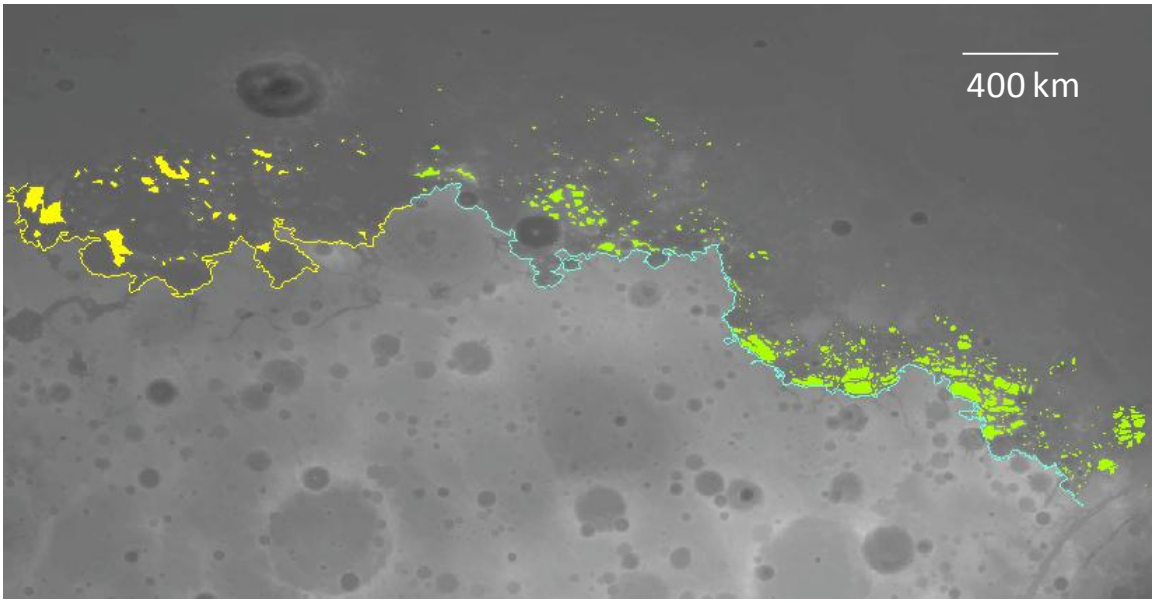

Figure 38. MOLA greyscale scale DEM showing two regions of escarpment and fretted terrain (blue line - northern escarpment, green polygons - northern fretted terrain, yellow line - northern low escarpment, yellow polygons - northern low fretted terrain). Modified from USGS MOLA DEM (1999).

The formation of the escarpment would have a direct impact as to how the fretted terrain came to be and was then altered by later processes. If endogenic processes were to have formed the escarpment problems arise with the current location of some of the blocks and the amount of material that has been removed. Squyres (1978) notes that the debris aprons currently found around individual blocks would only account for ~5 km of scarp retreat, yet we see mesas and knobs more than 300 km from the scarp today. One way to

account for these island-like mesas and knobs would be a mega-impact followed by crustal extension, potential terrace formation, and rafting (Fig. 39).

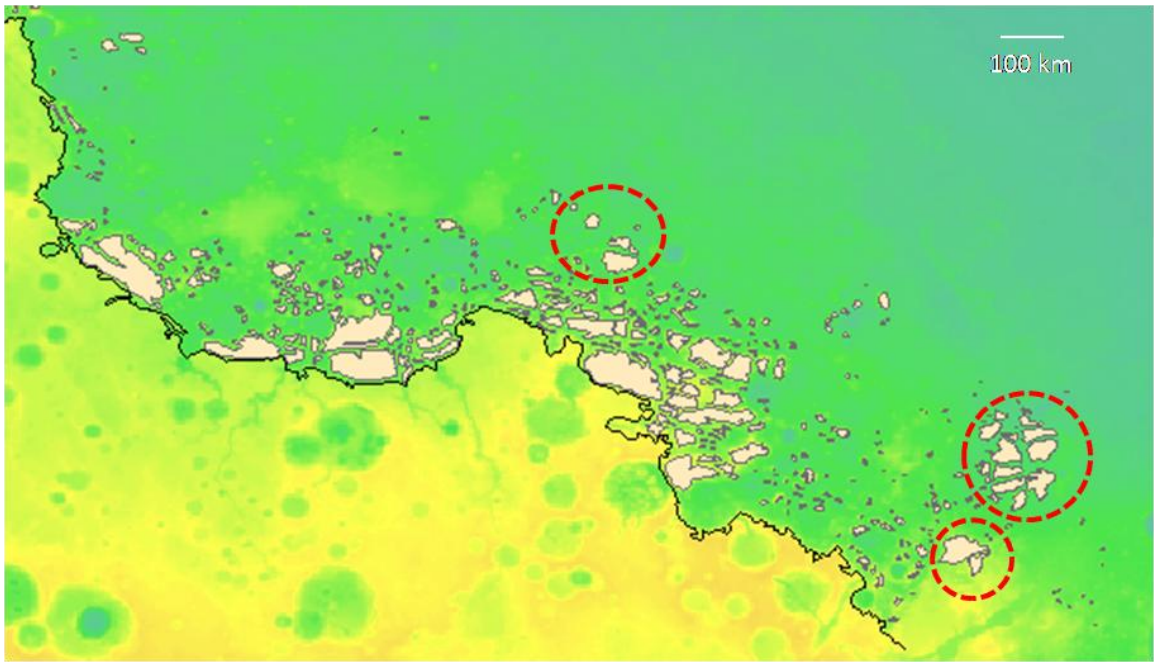

Figure 39. Possible cohesive, rafted fretted blocks of same elevation located at least 150 km from the global escarpment. Black line – global escarpment; beige blocks – northern fretted terrain blocks; red dashed circles – possible rafted blocks. Modified from USGS MOLA DEM (1999).

Associated with the impact, crustal extension in the form of horst and grabens and a tilted terrace structure could form (Melosh 1989; see Fig. 37). This would greatly reduce the amount of erosion and sediment transport that would have occurred under normal conditions and could account for the >300 km distance that is related to some mesas and knobs. The orientation of the long axis of the northern fretted terrain blocks approximately parallels the escarpment and the ratio of the long vs. short axis provide evidence of contiguous extension over a large area (Fig. 40). The 1st tier of the northern fretted terrain is also horizontally equivalent to the escarpment and shows no preferential tilt (Fig. 40).

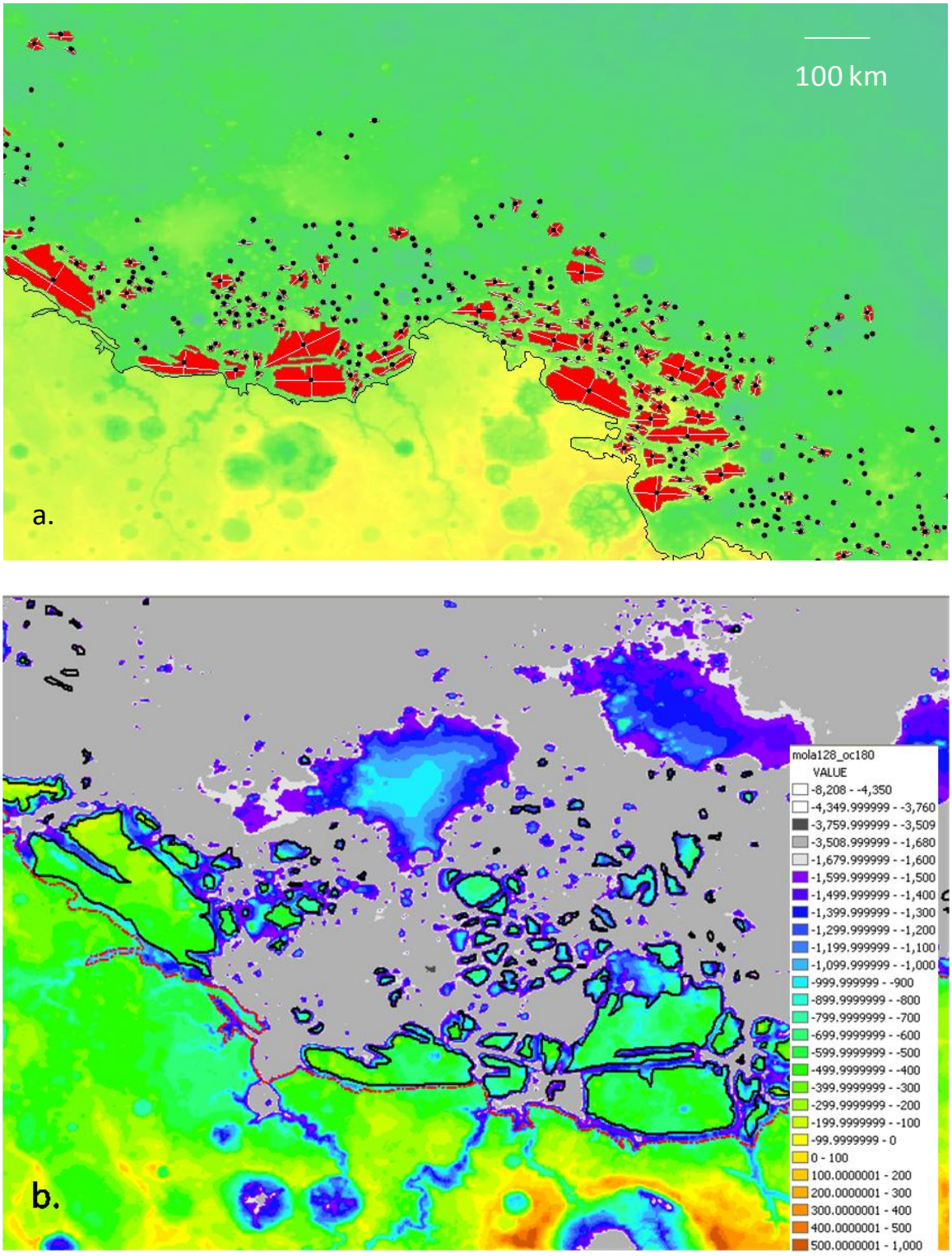

Figure 40. Orientation and elevation of the fretted terrain: (a) orientation of fretted blocks with center of mass, long, and short axes; (b) reclassification of MOLA DEM showing consistent elevations. Modified from USGS MOLA DEM (1999).

The northern low fretted terrain does not show any corresponding trend, but major overprinting of later impacts could have obliterated any evidence of earlier extensional fracturing. Crustal contraction of a magma pool during cooling could be formed in a crater of considerable size. This radial pattern is seen in many crater basins on Mars including the ones associated with the northern low fretted blocks. A safe assumption on the lines of this evidence would be that the northern low fretted terrains are the remnants of later impacts and the majority of the fretted blocks are potentially crater rims and/or contractional blocks (Fig. 41).

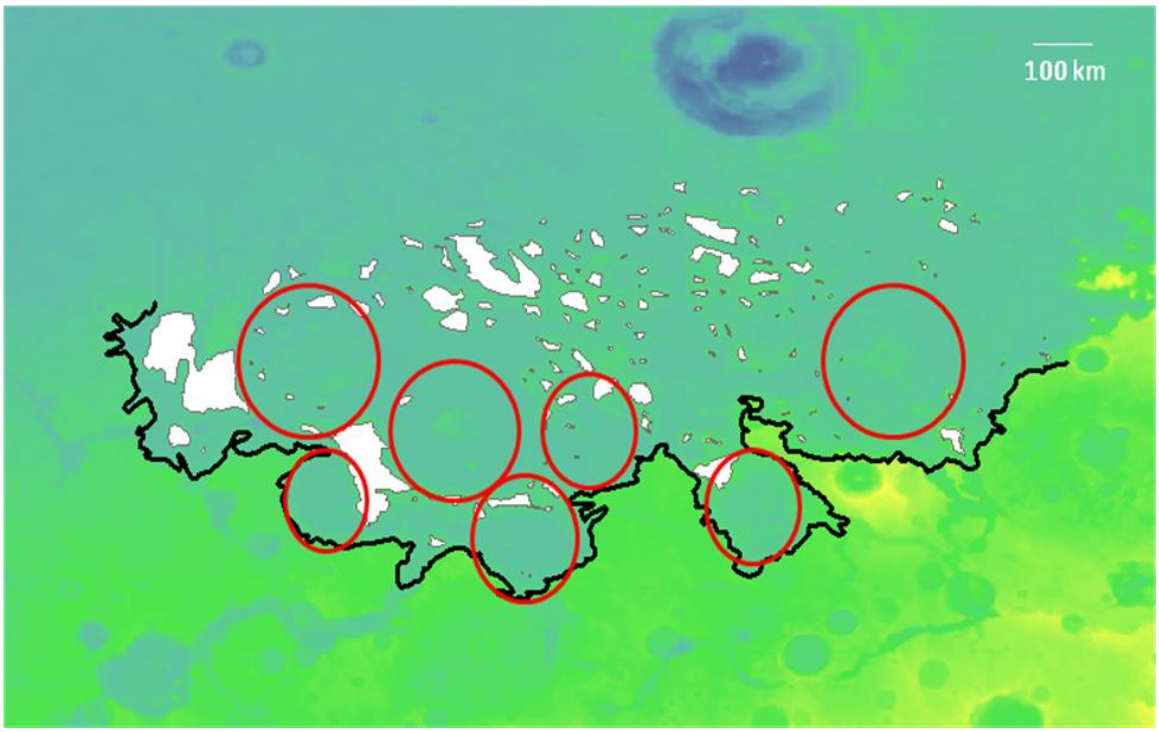

Figure 41. Sections of the global escarpment composed from MOLA-based DEM: (a) northern section (black line - northern global escarpment, red polygons - northern fretted blocks, black dots - center of mass of polygon, and white lines- long and short axis); (b) northern low section (black line - northern low escarpment, white polygons - northern low fretted blocks, red circles - post escarpment formation impact sites). Modified from USGS MOLA DEM (1999).

Erosional processes have played a major role in the evolution of the fretted terrain. Many geomorphic processes have been identified on Mars and the timing and intensity of some of these modifications are debatable. The Martian history is complicated so differing processes will be addressed separately depending on their place in history.

After the formation of the escarpment more than 4 billion years ago, Mars would have been cool enough have a primitive, denser atmosphere. If this were the case, then water would have been stable at the surface unlike today. Oceans or seas could have formed in the low lying areas or basins. The extremely flat lying topography which is located in the northern basin could be attributed to an ancient ocean. To assess the erosional capability of a potential oceanic shoreline in the northern basin, four different proposed paleoshores were incorporated in ArcGIS (Fig. 42).

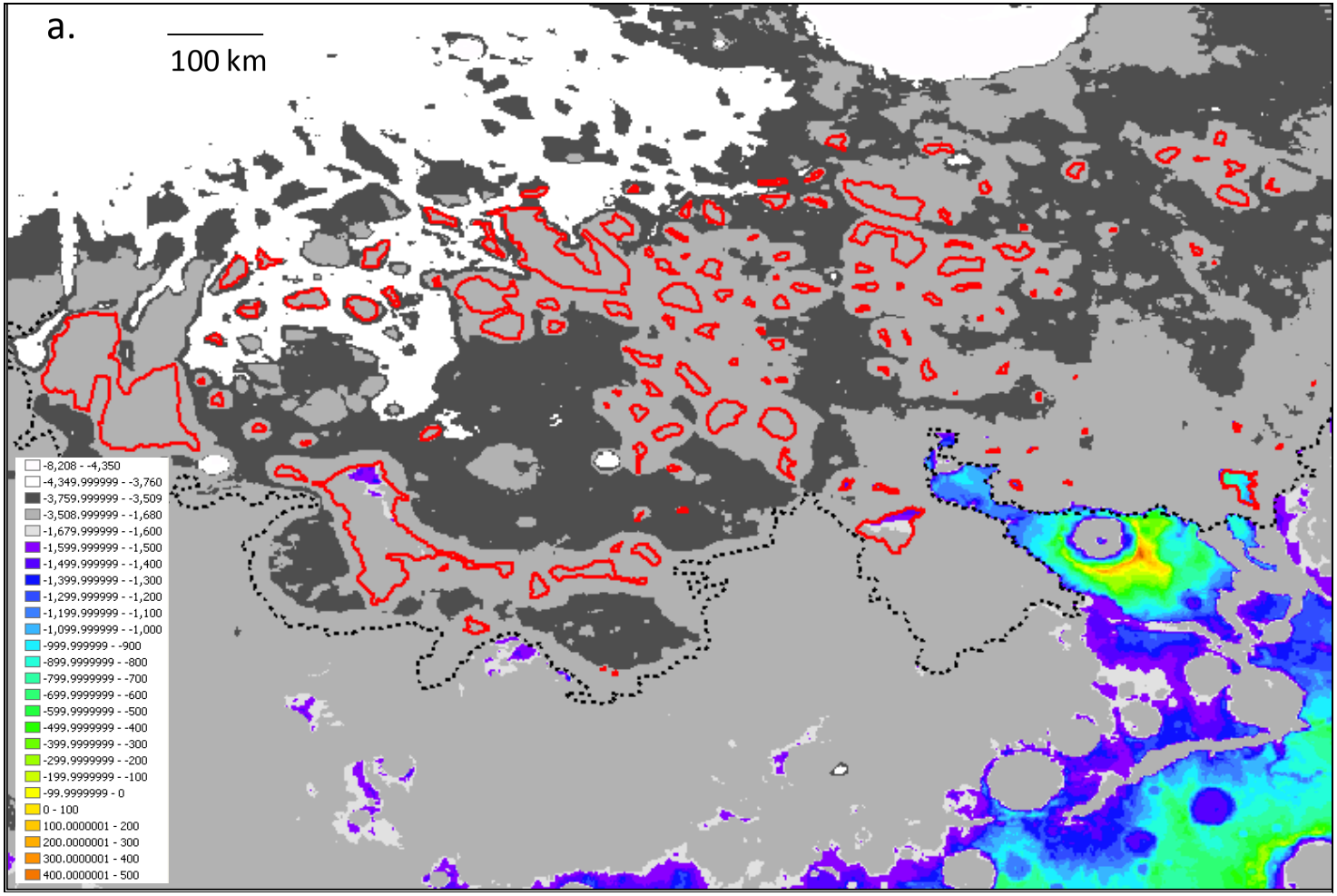

Figure 42. (a) Reclassified MOLA-based DEM of proposed ancient high stand shore lines: northern low escarpment area (black dashed line - northern low escarpment, red polygons - northern low fretted blocks). Modified from USGS MOLA DEM (1999).

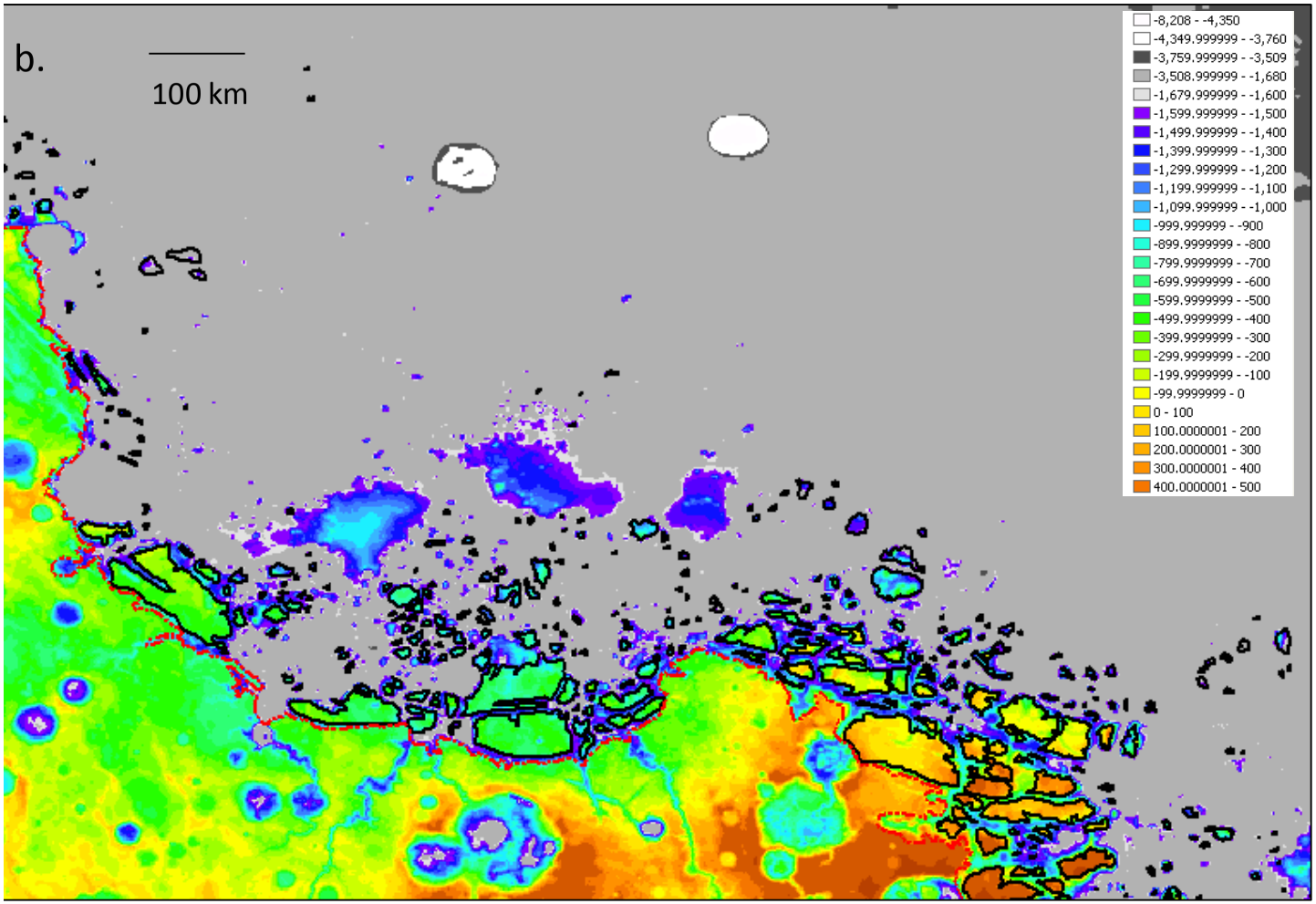

Figure 42. (b) Reclassified MOLA-based DEM of proposed ancient high stand shore lines: northern escarpment area (dashed red line - northern escarpment; Northern polygons are outlined in black). Modified from USGS MOLA DEM (1999).

The four proposed shoreline elevations were extracted using MOLA data with imagery and correspond to possible high stands. These elevations are -1,680 m and -3,760 m from Head et al. (1999) along with -3,509 m and -4,350 m from Baker et al. (1991). Analyzing these four proposed shorelines some fallacies become apparent. In the northern fretted terrain only the -1,680 m elevation would have been able to gradually erode the escarpment. Again Squyres (1978) attributes only ~5 km of retreat over the life of the escarpment providing question as to the northern fretted terrains being formed only due to erosional processes of a potential shoreline. Of the four shorelines, this elevation is the most erratic and less contiguous over long distances and has a greater tendency for topographic modification over time. Due to the lower elevations present in the northern low escarpment region alterations are far more likely with any of the four paleoshoreline elevations with complete submergence at the -1,680 m line. Erosional processes could have contributed to mass wasting and larger debris aprons that are seen around the northern low fretted blocks. The point of this analysis is not to justify the presence of a past ocean, but simply to show possible analogs that would correspond with these ancient shorelines.

Findings using analysis on recently studied craters and by the Pathfinder Rover show strong evidence that subsurface ice is stable on Mars at relatively shallow depths (Smith et al. 2009). One example of this is CRISM image 0009DEC (Fig. 43). Looking closely at the sediment transport pattern, we can deduce that liquid water has possibly breached the crater rim and flown down gradient. Also the non interconnecting rill pattern seen on the side of the block lends to more recent activity possibly associated with the corresponding impact.

Figure 43. CRISM image 0009DEC. Recent crater showing reactivation of subsurface ice by melting. Image from Arizona State University, CRISM database (2006).

Due to these confirmations, the scarp recession by the undermining of an overlying resistant material in the form of weathering is a viable solution to the transport mechanisms that form the fretted terrain (Sharp 1973). Outlying mesa and buttes of the region are irregular in shape and lack a streamline appearance that would more resemble fluvial transport (Lucchitta 1984). These fretted blocks are also non-uniform in shape, while on Earth such formations tend to be aligned parallel or become conical in varying

wind patterns (Breed et al. 1982). The extent as to when this process began is still debatable, but is an ongoing process today that could been accelerated in the recent past by Milankovitch-type cycles.

Milankovitch's proposal that the Earth's climate has been modulated through time due to changes in the axial tilt and other orbital parameters is well accepted in the scientific community today (Short et al. 1991). These three cycles on Mars are: (1) eccentricity – the change in shape of Mars' orbit around the Sun; (2) precession - the slow wobble as it spins on axis; and (3) obliquity - the inclination of Mars' axis in relation to its plane of orbit around the Sun are thought to be the cause of glacial periods on Mars in the past (Fig. 44).

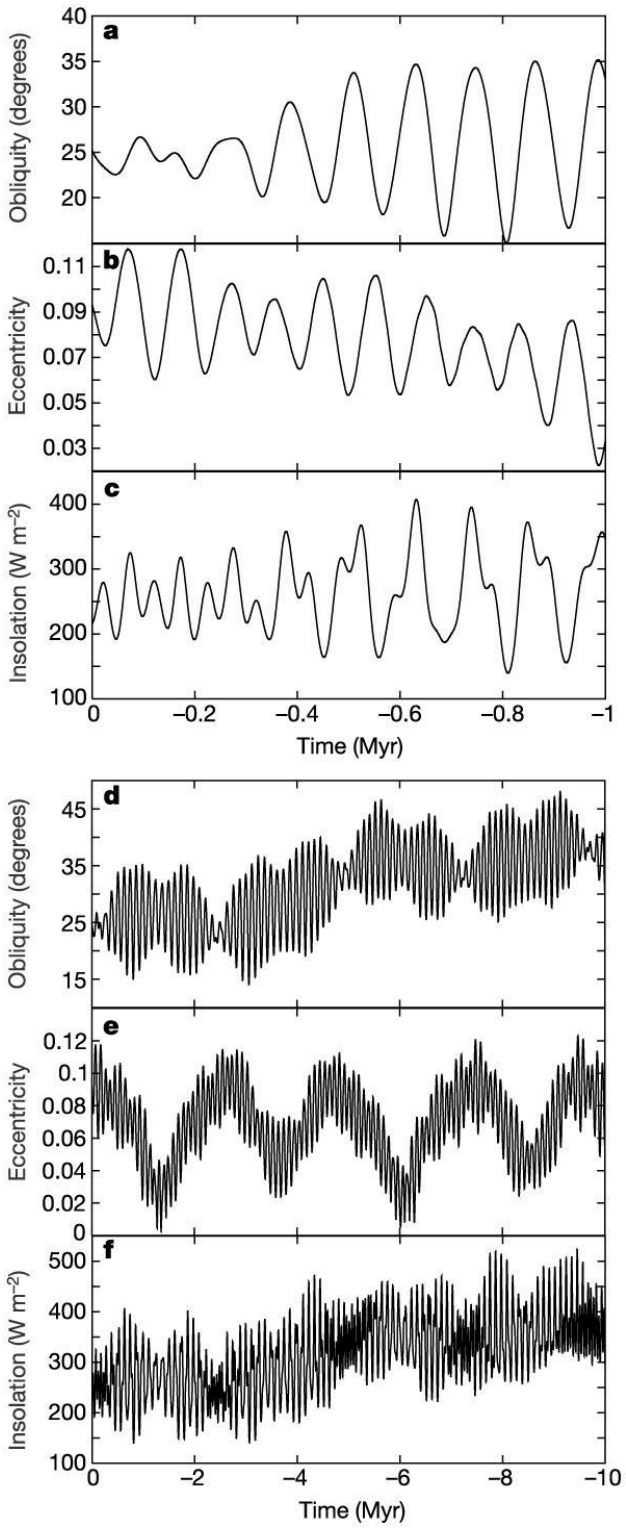

Figure 44. Insolation, eccentricity, and obliquity of Martian polar region over two time scales. From Lasker (2002).

The eccentricity of the Martian orbit ranges from 0.004 to 0.141 (0 to 14%) and today is currently at 0.093. This change in shape is interwoven into a 95 to 99 k.y. cycle with a longer 2.4 m.y. resonance (Ward 1974). Precession of Mars constitutes a cycle of 175 k.y. years (Head et al. 2003). The Martian obliquity cycle is 120 k.y. with a longer 1.2 m.y. resonance. The present obliquity is 25º and has a rather wide range of 18° to 48º compared to the smaller change of 21.5º to 24.5º for the Earth. Obliquity is the most important of the three cycles because it directly determines the amount of sunlight that reaches the poles. Periods of high obliquity correspond with removal of ice at the polar cap and redeposition at lower latitudes (Phillips et al. 2008). This period - referred to as an "ice age" - would result in a possible buildup of dust/sediment in the polar region (Fig. 45).

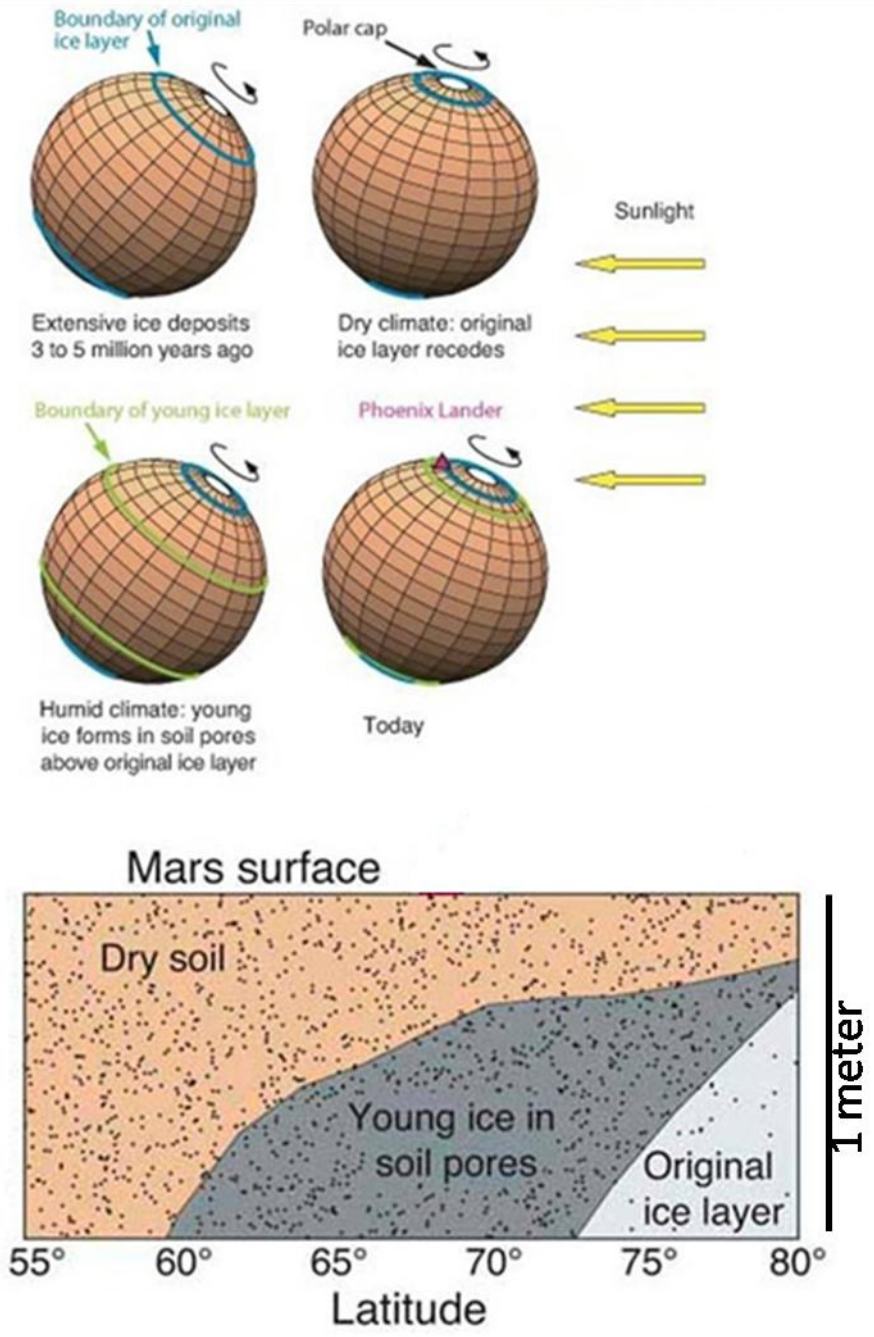

Figure 45. Movement of ices on the Martian surface through time. Modified from Schörghofer (2007).

The continued fluctuations in the Martian seasons and obliquity can cause massive transport of ice from polar to lower latitudes or inversely from lower latitudes to the polar region. The additional accretion of interbedded ice and soil followed by the sublimation

of ices would give rise a constantly changing landscape. Evidence of this process can be seen in the northern fretted region. Possible glacial evidence may be present in the form of moraines (Fig. 46).

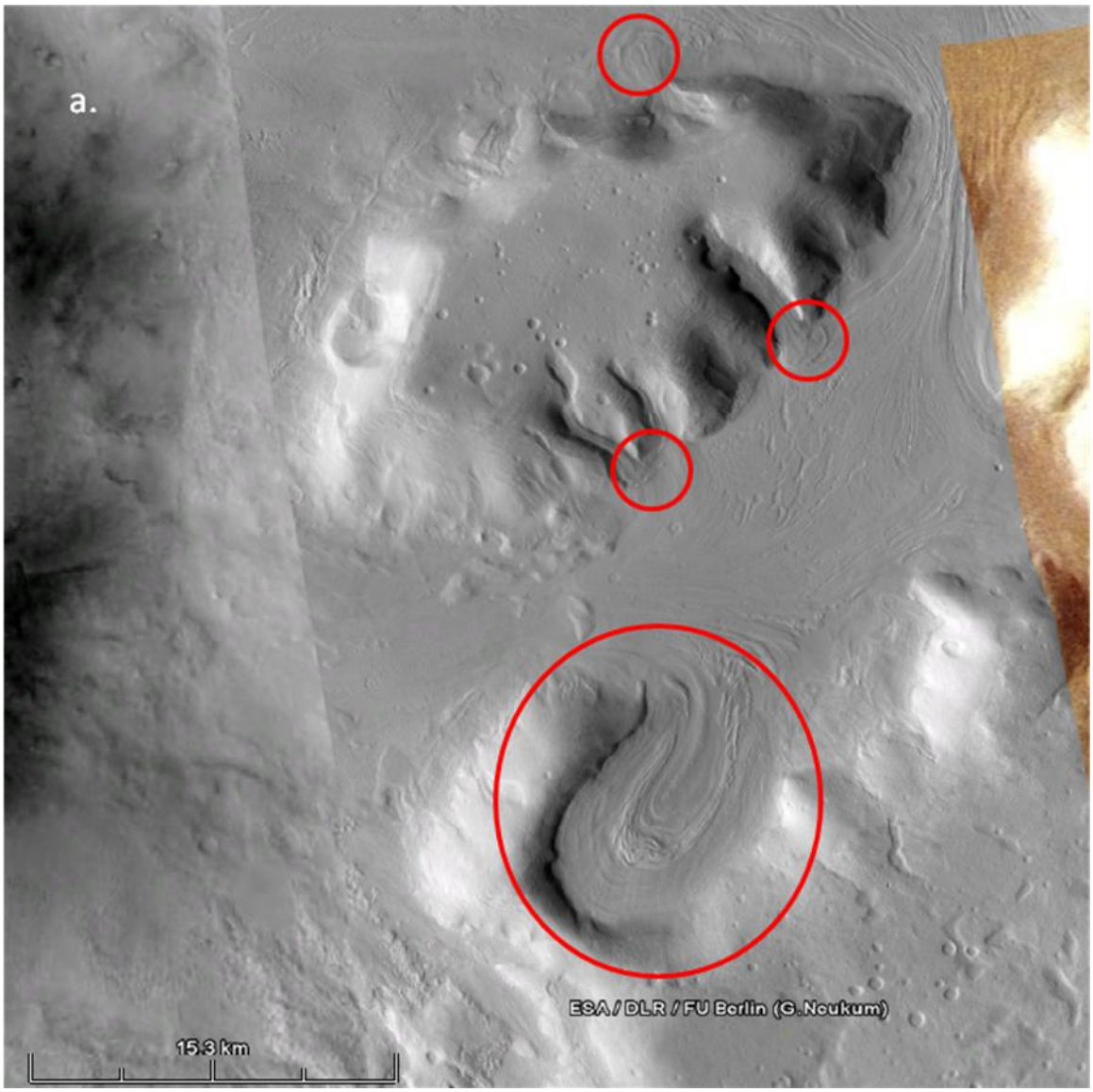

Figure 46 a. Wide field view of CTX image P01_001570_2213_XI_41N305W in Google Earth with possible ice induced movement highlighted in red circles. Image from Arizona State University, Context images (2006).

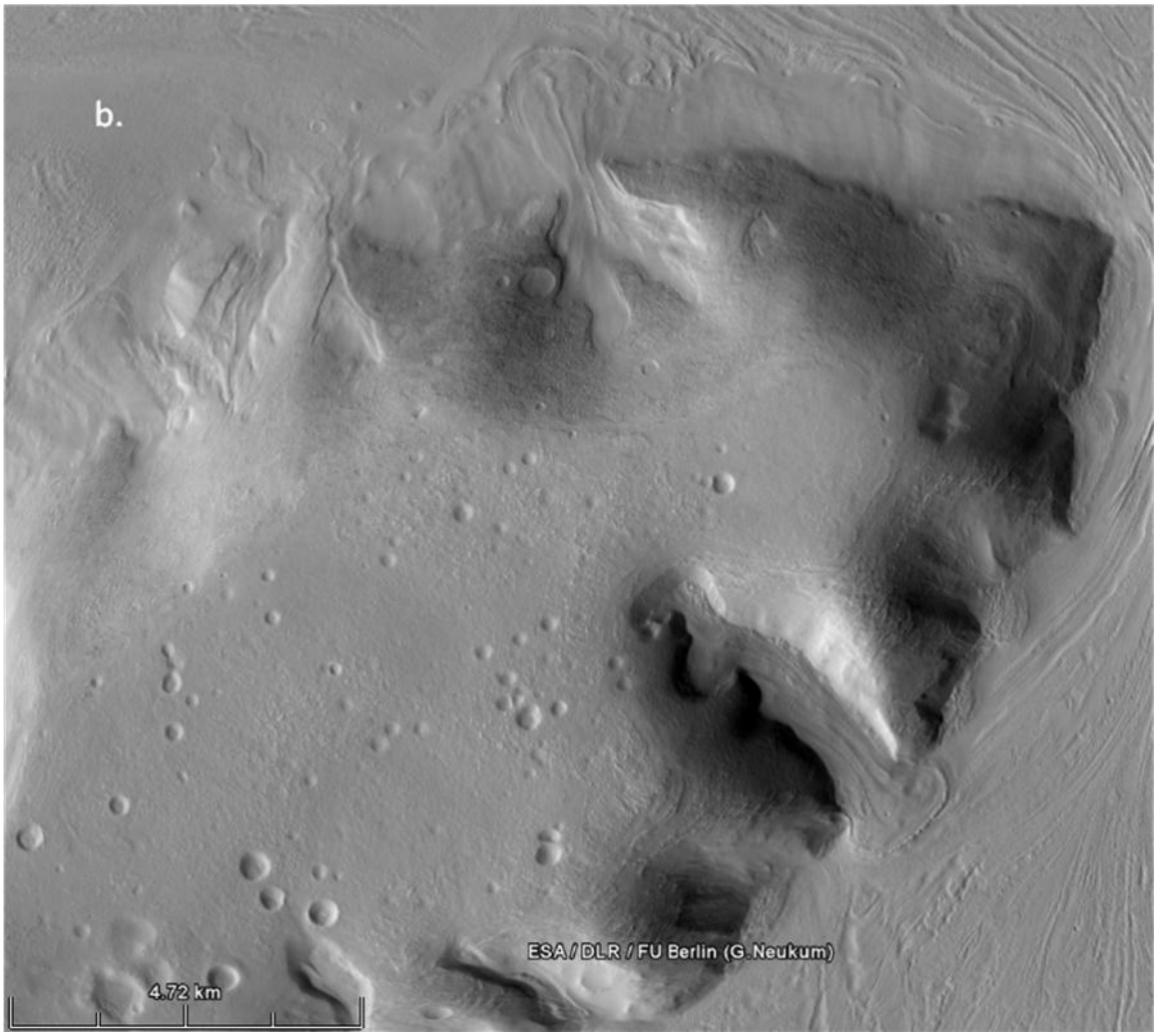

Figure 46 b. Overhead close up view of CTX image P01_001570_2213_XI_41N305W in Google Earth with possible end moraines at margin of a fretted block. Image from Arizona State University, Context images (2006).

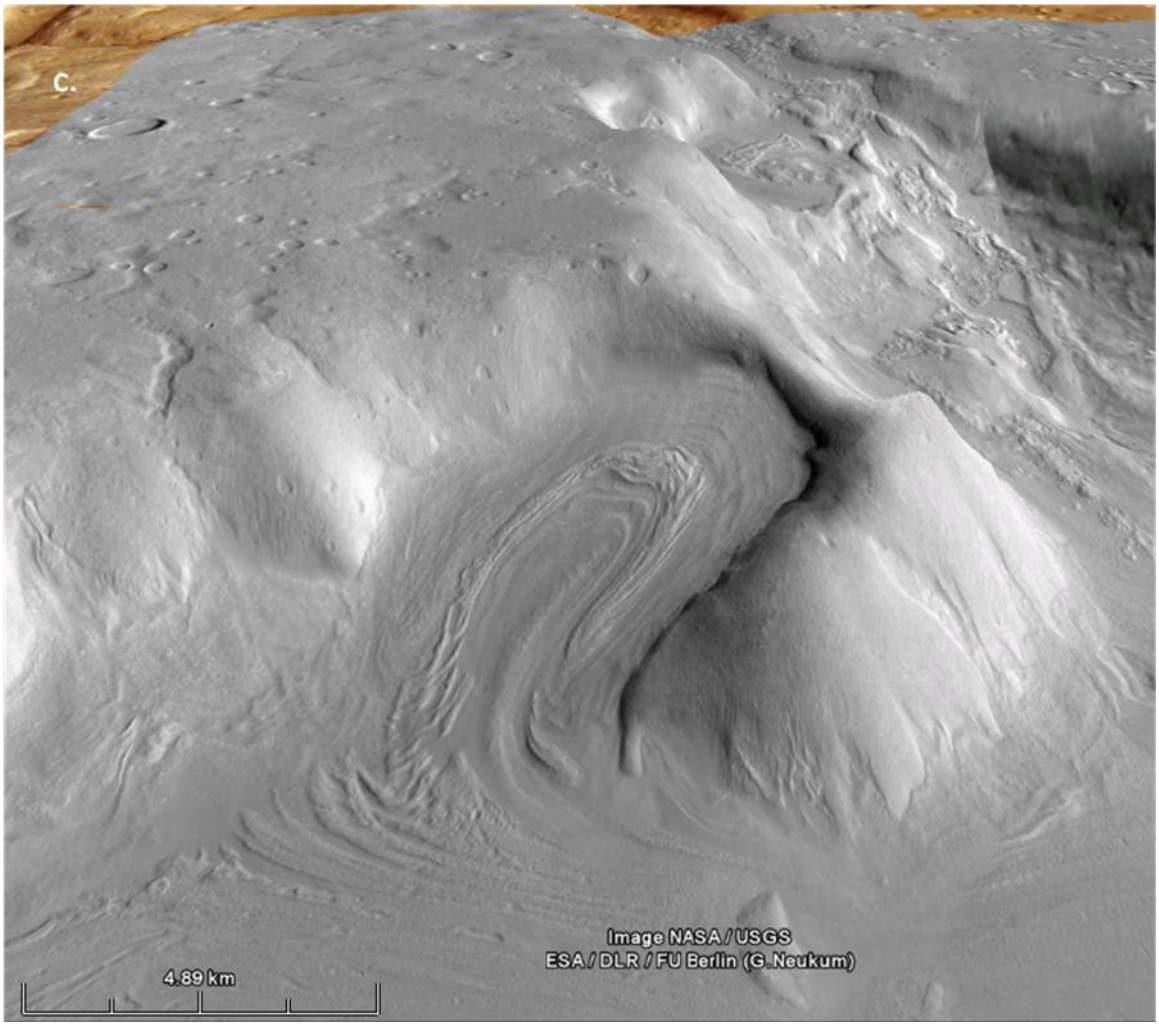

Figure 46 c. Cirque-like feature with end moraines viewed at 60ºfrom horizontal in Google Earth. Vertical exaggeration 3:1. Image from Arizona State University, Context images (2006).

It is important to note that there is no evidence of these features found south of 30º. More recent sublimation activity can be seen in the northern low fretted terrain. With the abundance of ice found in the vicinity of the surface, it may be safe to assume that some type of cryogenic karst modification would be present. An example of this can be found in the form of ice wedge polygons which resemble Earth-like features found in arctic regions (see Figs. 13 and 47).

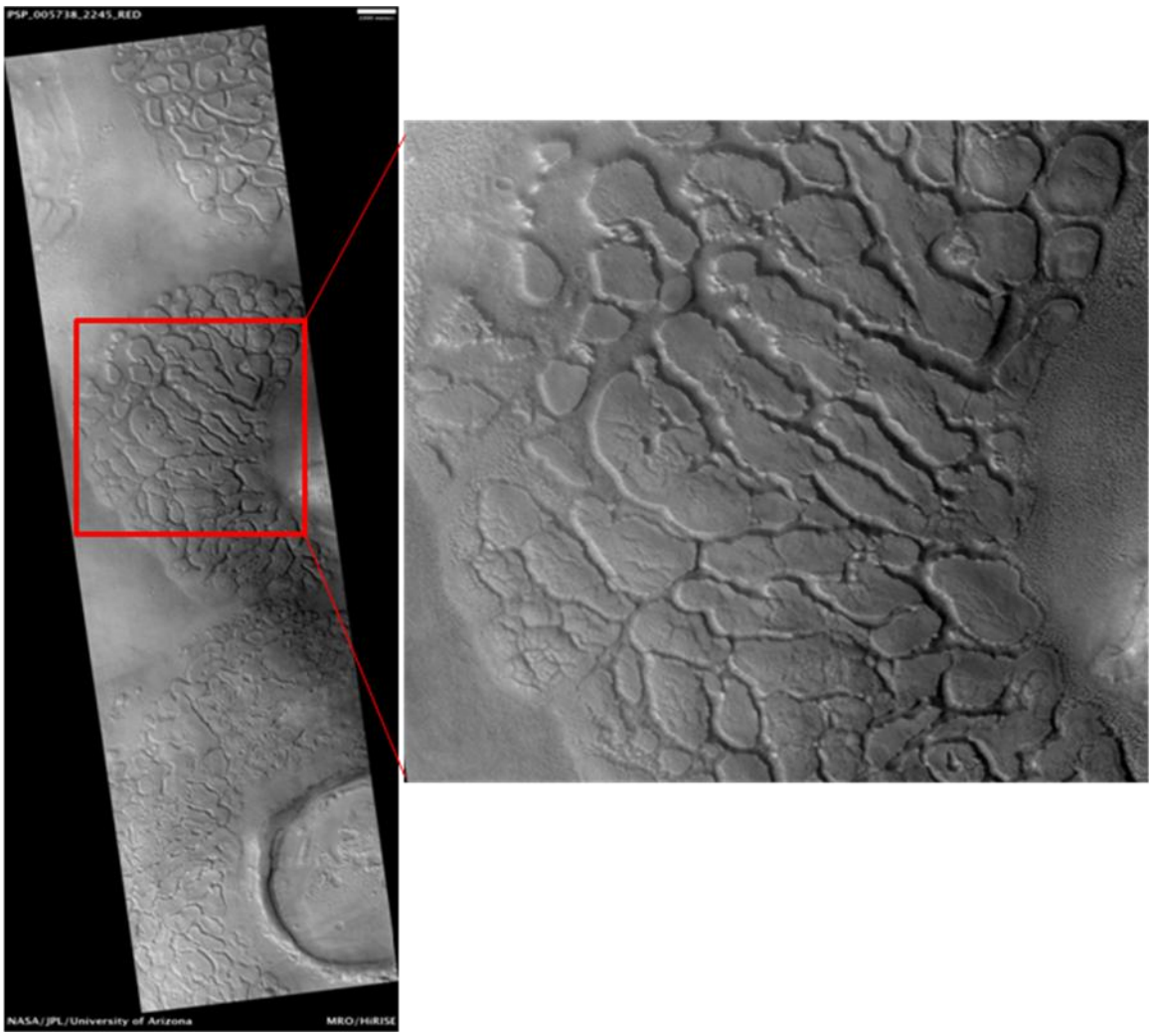

Figure 47. HiRISE image PSP_005738_2245RED showing possible cryogenic karst alteration found in the northern low fretted terrain. Image from Arizona State University, HiRISE database (2007).

CONCLUSION AND FURTHER WORK

Investigations show that Mars has been tectonically and hydrologically active throughout the past 4.5 billion years. Of all the planets, Martian geomorphology bears the closest resemblance to what we see on Earth. Whether the global escarpment was formed by internal or external force does not change the fact that it is one of the most impressive structures found in the solar system.

Discrepancies arise with any of the processes thought to have formed the Martian dichotomy. While advanced modeling techniques using internal heat flow have helped address some of the mega-features on the Martian surface, many assumptions have to be considered in assessing the outcome of these models. Early in the formation of Mars, energy in the interior would have been sufficient enough to cause a degree-1 mantle plume. Troubles emerge with the initial cooling rate of the planet to form a stagnant lid of sufficient thickness and incorporation of a mantle/core boundary with viscosity deviance greater than 100 fold. Plate tectonics can explain many observations, but the lack of a relic subduction zone and no mountain chains along the escarpment provide problems with this theory as well. Multiple impacts can account for the irregular shape of the escarpment, but crustal thickness models and the biased assumption of many large impacts in a single hemisphere is unlikely. With the research and data acquired during this project, a single mega-impact can answer most of the underlying questions about the escarpment and account for the fretted terrain as a consequence. The shape of the

Borealis basin is not circular/elliptical today but, models extracting the Tharsis rise and more than 4 billion years of modification can more than account these irregularities. The northern fretted terrain may be the possible remnant of a ring structure and could account for much of the apparent material loss for the region due to crustal contraction. The northern low fretted terrain is most likely contractional blocks and younger, smaller crater rims. The two fretted terrain regions have both been modified by both fluvial and aeolian processes in the past, but the transport of material by the fretting process is the dominant regime of geomorphologic change today. The examination of data in this paper tends to encourage the single impact theory as the most plausible outcome for the formation of the global escarpment and fretted terrain. This does not rule out any of the other postulated theories, but sheds insight into further investigation on the matter.

Further work would be invaluable in confining the formational and evolutional processes of the Martian dichotomy. The release of new images can provide more data for analysis. The SHARAD imagery database of ground penetrating radar would also help in interpretations of the shallow subsurface. New and improved modeling techniques can help explain the internal workings of a planet the size of Mars.

REFERENCES

Aharonson O., Zuber M. T., Smith, D. E., Neumann, G. A., Feldman, W. C., Prettyman, T. H. 2004. *Journal of Geophysical Research* 109(E05004), DOI:10.1029/2003JE002223.

Andrews-Hanna J. C., Zuber M. T., Banerdt W. B. 2008. The Borealis Basin and the Origin of the Martian Crustal Dichotomy. *Nature* 453:1212-1216.

Arizona State University Mars Global Data Sets Database 2010 <http://www.mars.asu.edu/data/> (Accessed 24 October 2009).

Baker V. R. 2001. Water and the Martian landscape. *Nature* 412:228–236.

Baker V. R., Strom R. G., Gulick V. C., Kargel J. S., Komatsu G., Kale V. S. 1991. Ancient oceans, ice sheets and the hydrological cycle on Mars. *Nature* 392:589-594.

Bibring J. P., Langevin Y., Mustard J. F., Francois P., Arvidson R., Gendrin A., Gondet B., Mangold N., Pinet P., Forget F., the OMEGA team. 2006. Global Mineralogical and Aqueous Mars History Derived from OMEGA/Mars Express Data. *Science* 312:400-404.

Baratoux D., N. Mangold C. Delacourt P. Allemand 2002. Evidence of liquid water in recent debris avalanche on Mars. *Geophysical Research Letter* 29:(GL014155).

Bell J. 2008. The Martian Surface: composition, mineralogy, and physical properties. Cambridge University press, United Kingdom, p. 169-395.

Bercovici D. 2003. The generation of plate tectonics from mantle convection**.** *Earth and Planetary Science Letters* 205 (3-4):107-121.

Bertka C. M., Fei Y. 1998 Density profile of an SNC model Martian interior the moment-of-inertia factors of Mars. *Earth and Planetary Science Letters* 157:79-88.

Bertka C. M., Fei Y. 1998. Constraints on the mineralogy of an iron-rich Martian mantle form high pressure experiments. *Planetary and Space Science* 44(11):1269-1273.

Bogard D. D., Nyquist L. E., Johnson P. 1984. Noble gas contents of shergottites and implications for the Martian origin of SNC meteorites. *Geochemica et Cosmochimica Acta* 48:1723- 1739.

Boyce J. M. 2002. *Mars.* Smithsonian Institute Press, Washington and London, p. 5-200.

Breed S. C., McCauley J. F., Groiler M. J. 1982. Relict drainage, conical hills, and the eolian veneer in Southern Egypt- Applications to Mars. *Journal of Geophysical Research* 87:9929-9950.

Breuer D., Zhou H., Yuen D. A., Spohn T. 1996. Phase transitions in the Martian mantle: implications for planet's volcanic history. *Journal of Geophysical Research* 101:7531-7542.

Carr, M. H. 1996. *Water on Mars*. Oxford University Press, New York, p. 1-145.

Carr M. H. 2001. Mars Global Surveyor Observations of Martian Fretted Terrain. *Journal of Geophysical Research* 106:23,571-23,593.

Cattermole P. 2001. *Mars: The Mystery Unfolds*. Oxford University Press, New York, p. 29-160.

Christiansen E. H. 1995. *Exploring the Planets*. Prentice-Hall, Inc, Brigham Young University, p. 140-197.

Christensen P. R., Bandfiewld J. L., Hamilton V. E., Ruff S. W., Kieffer H. H., Titus T. N., Malin M. C., Morris R. V., Lane M. D., Clark R. L., Jakosky B. M., Mellon M. T., Pearl J. C., Conrath B. J., Smith M. D., Clancy R. T., Kuzmin R. O., Roush T., Mehall G. L., Gorelick N., Bender K., Murray K., Dason S., Greene E., Silverman S., Greenfield M. 2001. Mars Global Surveyor Thermal Emission Spectrometer experiment: Investigation description and surface science results. *Journal of Geophysical Research* 106(E10):23,823,871.

Christensen P. R., Jakosky B. M., Kieffer H. H., Malin M. C., McSween H. Y. jr., Nealson K., Mehall G. L., Silverman S. S., Ferry S., Caplinger M., Ravine, M. 2004. The Thermal Emission Imaging System (THEMIS) for the Mars 2001 Odyssey Mission. *Space Science Reviews* 110:85-110.

Dallas S. S. 1996. *Mars Global Survey Mission*. Jet Propulsion Laboratory, Pasadena CA, p. 173-189.

Elkins-Tanton L. T., Parmentier E. M., Hess P. C. 2003. A model for Martian magma ocean crystallization and overturn. *Meteoritics and Planetary Science* 38:1753–1772.

ET Spatial Techniques 2010. ET GeoTools for ArcGIS <http://www.ian-ko.com/> (Accessed: 8 Sept, 2009).

Freitas R. Jr., Valdes F. 1980. A Search for Natural or Artificial Objects Located at the Earth-Moon Libration Points. *Icarus* 42:442-447.

Frey H. 2006. Impact constraints on the age and origin of the lowlands of Mars. *Geophysical Research Letter* 33: L08S91.

Frey H. 2004. A timescale for major events in the early Martian crustal evolution. *Lunar and Planetary Science Conference XXXV* abstr. 1382.

Frey H., Sakimoto S. E., Roark J. H. 1998. The MOLA topographic signature at the crustal dichotomy boundary zone on Mars. *Geophysical Research Letter* 25: 4409–4412.

Frey H., Schultz R. A. 1988. Large impact basins and the mega-impact origin for the crustal dichotomy on Mars. *Geophysical Research Letter*15:229–232.

Gangale T. 2007. *Geologic Time Scales of the Earth, Moon, and Mars.* <http://pweb.jps.net/~tgangale/mars/mst/GeologicTimeScales.htm.> (Accessed: 18 Oct. 2008).

Golombek M. P. and 54 co-authors 1999. Overview of the Mars pathfinder mission: launch through landing, surface operations, data sets, and science results. *Journal of Geophysical Research* 104:8523-8555.

Gomes R., Levison H. F., Tsiganis K., Morbidelli A. 2005. Origin of the cataclysmic Late Heavy Bombardment period of the terrestrial planets. *Nature* 425:466-469.

Graf J. E., Zurek R. W., Eisen H. J., Jai B., Johnston M. D., DePaula R. 2005. The Mars Reconnaissance Orbiter Mission. *Acta Astronautica* 57(2-8):566-578.

Grieve R. A. F. 1987. Terrestrial impact structures. *Annual review of Earth and Planetary Science* 15:245-270.

Hager B., Richards M. 1989. Long wavelength variations in Earth's geoid: Physical models and dynamic implications. *Philosophical Transactions of the Royal Society of London, Series A* 328:309-327.

Halliday A. N., Wanke H., Birck J. L., Clayton R. N. 2004. The accretion, composition, and early differentiation of Mars. *Space Science Reviews* 96(1-4):197-230.

Harder H., Christensen U. 1996. A one plume model of Martian mantle convection. *Nature* 380:507-509.

Hart S. H., Nimmo F., Korycansky, D., Agnor C. 2007. Probing the giant impact hypothesis of the Martian crustal dichotomy. *Proc. of 7th International Conference of Mars* abstr. 3332

Hartmann W.K., Cruikshank D.P., Degewij J., Capps R.W. 1981. Surface materials on unusual planetary object Chiron. *Icarus* 47:333-341.

Hartmann W. K., Neukum G. 2001. Cratering chronology and the evolution of Mars. *Space Science Review* 96:165-94.

Head J. W. 1974. Orientale multiringed basin interior and implications for the petrogenesis of lunar highland samples. *Moon* 11:327-356.

Head J. W., Hiesinger H., Ivanov M. A., Kreslavsky M. A., Pratt S., Thomsom B. J. 1999. Possible Ancient Oceans on Mars: evidence from Mars Orbital Laser Altimeter Data. *Science* 286:2134-2140.

Head J. W., Mustard J. F., Kreslavsky M. A., Milliken R. E., Marchant D. R. 2003. Recent Ice Ages on Mars. *Nature* 426:797-802.

Irwin R. P. III, Watters T. R. 2004. Sedimentary resurfacing and fretted terrain development along the crustal dichotomy boundary, Aeolis Mensae, Mars. *Journal of Geophysical Research* 106:(E09011).

Jagoutz E. 1989 Sr and Nd isotopic systematics in ALHA 77005: Age of shock metamorphism in shergottites and magmatic differentiation on Mars. *Geochimica et Cosmochimica Acta* 52(9):2429-2441.

Ke Y, Solomatov V. S. 2006. Early Transient Superplumes and the Origin of the Martian Crustal Dichotomy. *Journal of Geophysical Research* 100:E10001.

Kiefer W. S. 2008. Forming the Martian Great Divide. *Nature* 453:1191-1192.

Kominami J., Ida S. 2002. The Effect of Tidal Interaction with a Gas Disk on Formation of Terrestrial Planets. *Icarus* 157:43-56.

Lasker J., Levrard B., Mustard J.F., 2002. Orbital forcing of the Martian polar layered deposits. *Nature* 419:375-377.

Lenardic A., Nimmo F., Moresi L. 2004. Growth of the hemispheric dichotomy and the cessation of plate tectonics on Mars. *Journal of Geophysical Research* 109:E02003.

Lucchitta B. K. 1980. Mars and Earth: Comparison of Cold-Climate Features. U.S. Geological Survey. *Icarus* 45:264-303.

Lucchitta, B. K. 1984. Ice and debris in the Fretted terrain, Mars. *Journal of Geophysical Research* 89:409-418.

Malin Space Science Systems 2010. Mars Global Surveyor and Mars Orbital Camera <http://www.msss.com/mgs/moc/index.html> (Accessed: 5 Jun, 2009).

Marinova M. M., Aharonson O., Asphaug E. 2008. Mega-impact formation of the Mars hemispheric dichotomy. *Nature* 453:1216-1219.

McGill G. E., Dimitriou A. M. 1990. Origin of the Martian global dichotomy by crustal thinning in the Late Noachian or Early Hesperian. *Journal of Geophysical Research* 95:12595–12605.

McGill G. E., Squyres S. W. 1991. Origin of the Martian crustal dichotomy: evaluating the hypothesis. *Icarus* 93:386-393.

McGovern P. J., Solomon S. C., Smith D. E., Zuber M. T., Simons M., et al. 2002. Localized gravity/topography admittance and correlation spectra on Mars: implications for regional and global evolution. *Journal of Geophysical Research* 107:5136.

Melosh H. J. 1989. Impact cratering: A geologic process Oxford University Press, New York.

Melosh H. J., McKinnon W. B. 1978. The mechanics of ringed basin formation. *Geophysical Research Letter* 5:985-988.

Melosh H .J. 1982. A simple mechanical model of Valhalla basin, Callisto. *Journal of Geophysical Research* 87:1880-1890.

Morgan J. V., Warner M. R., Collins G. S., Melosh H. J., Christeson G. L. 2000. Peak-ring formation in large impact craters: geophysical constraints from Chicxulub. *Earth and Planetary Science Letters* 183:347-354.

Mottana A., Crespi R., Liborio G., 1977. *Simon and Schuster's Guide to Rocks and Minerals.* Simon and Schuster Inc., Rockefeller Center, New York, p. 52-248.

Murchie S. L., Arvidson R. E., Bedini P., Beisser K., Bibring J. 2004. CRISM (Compact Reconnaissance Imaging Spectrometer for Mars) on MRO (Mars Reconnaissance Orbiter). *Proc. SPIE* 5660:DOI:10.1117/12.578976.

NASA 1999. Mars Orbital Laser Altimeter <http://mars.jpl.nasa.gov/mgs/sci/mola/mola-may99.html> (Accessed: 5 Jun, 2009).

NASA 2010a. Mars Global Surveyor <http://mars.jpl.nasa.gov/mgs/overview> (Accessed: 5 Jun, 2009).

NASA 2010b. NASA's Mars Exploration Project <http://mars.jpl.nasa.gov/odyssey/overview> (Accessed: 5 Jun, 2009).

NASA 2010c. Scientific Visualization Studio <http://svs.gsfc.nasa.gov/vis/a000000/a002200/a002291/index.html> (Accessed: 7 Feb 2010).

NASA 2010d. Mars Reconnaissance Orbiter <http://mars.jpl.nasa.gov/gallery/spacecraft/index.html> (Accessed: 14 June 2009).

NASA 2010e. Planetary Data System (PDS) <http://pds.jpl.nasa.gov/> (Accessed: 6 Nov 2008).

Nimmo F., Stevenson D. 2001. Estimates of Martian crustal thickness from viscous relaxation of topography. *Journal of Geophysical Research* 106:5085–5098.

Nimmo F., Tanaka K. 2005. Early Crustal Evolution of Mars. *Annual Review of Earth and Planetary Science* 33:133-61.

Parker T. J., Gorsline D. S., Saunders R. S., Pieri D. C., Schneeberger D. M. 1993. Coastal Geomorphology of the Martian Northern Plains. *Journal of Geophysical Research* 98:11061-11078.

Phillips R. J., Zuber M. T., Smrekar S. E., Mellon M. T., Head J. W., Tanaka K. L., Putzig N. E., Milkovich S. M., Campbell B. A., Plaut J. J., Safaeinili A., Seu R., BiccarD., Carter L.M., Picardi G., Orosei R., Mohit P.S., Heggy E., Zurek R.W., Egan A. F., Giacomoni E., Russo F., Cutigni M., Pettinelli E., Holt J. W., Leuschen C. J., and Marinangeli, L. 2008. Mars Northern Polar Deposits: Stratigraphy, Age, and Geodynamical Response. *Science* 320:1182-1185.

Phillips R. J., Zuber M. T., Solomon S. C., Golombek M. P., Jakosky B. M., Banerdt W. B., Smith D. E., Williams R. M. E., Hynek B. M., Aharonson O., Hauck S. A. II 2001. Ancient Geodynamics and Global-Scale Hydrology on Mars. *Science* 281: 2587-2591.

Pruitt E. 1960. ONR's geographic research program. *Naval Research Reviews* 1–9.

Rieder R., Economou T., Wenke H., Turkevich A., Crisp J., Bruckner J., Dreibus G., McSween H. 1997. The chemical Composition of Rocks and Soils Returned by the Mobile Alpha Proton X-ray Spectrometer: Preliminary Results from the X-ray Mode. *Science* 278:1771-1773.

Roberts J. H. 2004. Degree-1 mantle convection as a process for generating the Martian hemispheric dichotomy. *Workshop on Martian Hemispheres* 4028.pdf.

Roberts J. H., Zhong S. 2006. Degree-1 mantle convection in the Martian mantle and the origin of the hemispheric dichotomy. *Journal of Geophysical Research* 111:E06013.

Rubin, A. E. 2002. Disturbing the solar system: impacts, close encounters and coming attractions. *Princeton University Press* p. 1-384.

Schörghofer N. 2007. Dynamics of ice ages on Mars. *Nature* 449:192-194.

Schultz P. H., Schultz R. A., Rogers J. 1982. The structure and evolution of Ancient impact basins on Mars. *Journal of Geophysical Research* 87:9803-9820.

Schultz R. A., Frey H. V. 1990. A New Survey of Multi-ring Impact Basins on Mars. *Journal of Geophysical Research* 95:(14)175-14,189.

Scienceray 2010, Great discoveries in the field of Earth science. <http://scienceray.com/earth-sciences/great-discoveries-in-the-field-of-earth-sciences/>(Accessed: 24 May 2010).

Scott D. H., Carr M. H. 1978. *Geologic Map of Mars*. Unites States Geological Survey, Department of Interior.

Scott D. H., Tanaka K. L., Greeley R., Guest J. E. 1987. Geologic Maps of the Western Equatorial, Eastern Equatorial and Polar Regions of Mars, Maps. I-1802-A, B and C, Miscellaneous Investigation Series, 1986-1987, *U.S. Geological Survey,* Flagstaff.

Sharp R. P. 1973. Mars: fretted and chaotic terrains. *Journal of Geophysical Research* 78: 4073–4083.

Short D. A., Mengel J. G., Crowley T. J., Hyde W. T., Northern G. R. 1991. Filtering of Milankovitch cycles by Earth's geography. *Science Digest* 35(2):157-173.

Sleep N. H. 1994. Martian plate tectonics. *Journal of Geophysical Research* 99:5639–5655.

Smith D. E., Zuber M. T., Solomon S. C., Phillips R. J. Head J. W., Garvin J. B., Banerdt W. B. Muhleman D. O., Pettengill G. H., Neumann G. A., Lemoine F. G., Abshire J. B., Aharonson O., Brown C. D., Hauck S. A., Ivanov A. B., McGovern P. J., Zwally H. J., Duxbury T. C. 1999. The Global Topography of Mars and Implications for Surface Evolution. *Science* 284:1495.

Smith P. H., Tamppari L. K., Arvidson R. E., Bass D., Blaney D., Boynton W. V., Carswell A., Catling D. C., Clark B. C., Duck T., DeJong E., Fisher D., Goetz W., Gunnlaugsson H. P., Hecht M. H., Hipkin V., Hoffman J., Hviid S. F., Keller H. U., Kounaves S. P., Lange C. F., Lemmon M. T., Madsen M. B., Markiewicz W. J., Marshall J., McKay C. P., Mellon M. T., Ming D. W., Morris R. V., Pike W. T., Renno N., Staufer U., Stoker C., Taylor P., Whiteway J. A., Zent A. P. 2009. H_2O at the Phoenix Landing Site. *Science* 325:68-71.

Sohl F., Spohn T. 1997. The internal structure of Mars: Implications from the SNC meteorite. *Journal of Geophysical Research* 102:1613-1635.

Squyres S. W., 1978. Martian fretted terrain: Flow of erosional debris. *Icarus* 34:600–613.

Stevenson D. J. 2001. Mars core and magnetism. *Nature* 412:214-219.

Stevenson D. J. 2003. Planetary magnetic fields. *Earth and Planetary Science Letters* 208:1-11.

Tanaka K. L. 1986. The stratigraphy of Mars. *Journal of Geophysical Research* 91: E139–158.

Tanaka K. L., Skinner J. A. Jr., Hare T. M., Joyal T., Wenker A., 2003, Resurfacing history of the northern plains of Mars based on geologic mapping of Mars Global Surveyor data. *Journal of Geophysical Research* 108(E4):24-1– 24-32, 8043, DOI: 10.1029/2002JE001908.

Tseung J-M., Soare R. J. 2006. Thermokarst and Related Landforms in Western Utopia Planitia, Mars: Implications for Near-surface Excess Ice. *Lunar and Planetary Science* XXXVII:1414.

Toulmin P., Baird A. K., Clack B.C. 1977. Geochemical and Mineralogical Interpretations of the Viking Chemical Results. *Journal of Geophysical Research* 82: 4625-4634.

USGS 2007a. Mars general image viewer <http://webgis.wr.usgs.gov/website/mars_html/viewer.htm> (Accessed: 14 Oct. 2008).

USGS 2007b. U.S.G.S Planetary GIS Web Server <http://webgis.wr.usgs.gov/pigwad/maps/index.html> (Accessed: 11 Sept, 2008).

USGS 2010a. Gazetteer of Planetary Nomenclature (IAU) <http://planetarynames.wr.usgs.gov/> (Accessed: 7 Feb, 2010).

USGS 2010b. U.S.G.S Planetary GIS Web Server <fttp://pdsimage2.wr.usgs.gov/pub/pigpen/mars/mola/> (Accessed: 14 Sept, 2008).

Vermeesch P. M., Morgan J. V. 2008. Structural uplift beneath the Chicxulub impact structure. *Journal of Geophysical Research* 113: B07103.

Ward A. W. 1974. Climate Variations on Mars: astronomical theory of insulation. *Journal of Geophysical Research* 84:7934-7939.

Watters T. R., McGovern P. J., Irwin R. P. 2007. Hemispheres Apart: The Crustal Dichotomy of Mars. *Annual Review of Earth and Planetary Sciences* 25: 621-652.

Wilhelms D. E. 1987. Geologic History of the Moon. U.S. *Geological Survey Professional Paper* 1348.

Wilhelms D. E., Squyres S. W. 1984. The Martian hemispheric dichotomy may be due to a giant impact. *Nature* 309:138-140.

Williams J., Nimmo F. 2004. Thermal evolution of the Martian core: Implications of an early dynamo. *Geology* 32(2):97-100.

Wise D. U., Golombek M. P., Mcgill G. E. 1979a. Tharsis Province of Mars: geologic sequence, geometry, and a deformation mechanism. *Icarus* 38:456-472.

Wise D. U., Golombek, M. P., Mcgill G. E. 1979b. Tectonic evolution of Mars. *Journal of Geophysical Research* 84:7934-7939.

Zhong S., Zuber M. T. 2001. Degree-1 Mantle Convection and the Crustal Dichotomy on Mars. *Earth and Planetary Science Letter* 189:75-84.

Zuber M. T. 2001. The crust and mantle of Mars. *Nature* 412:220-227.

Zuber M. T., Smith D.E., Solomon S.C., Muhleman D.O., Head J.W., Garvin J.B., Abshire J.B., Bufton J.L. 1992. The Mars Observer Laser Altimeter Investigation. *Journal of Geophysical Research* 97:7781-7797.

Zuber M. T., Solomon S. C., Phillips R. J., Smith D. E., Tyler G. L., et al. 2000. Internal structure and early thermal evolution of Mars from Mars Global Surveyor topography and gravity. *Science* 287:1788–1793.

APPENDIX

ArcMap 9.2

Application	Source
Retrieve missing File (!)	right click on file>>repair source>>file
Checking application Insertion	click on view>>tool bar or right click on file
Georeferencing	add data, then select data>>right click>>zoom to layer (set layer that will be referenced 1st in the appropriate tool bar) then click and add control points
Updating Georeferenced map	click on georeference drop down>>update georeferencing
Transparency	right click on layer>>display>>change transparency
Source for a Particular layer	click on source at bottom of map layers box
Creating a new Coordinate system	click on view>>data frame properties>>coordinate system>>new>>projected coordinate system>>Mars 2000
Changing color On an existing map	right click on layer>>properties>>symbology>>color ramp
Attributes table	right click on layer>>open attributes table
Reclassification	right click on layer>>symbology>>classified>>select number of classes or arc tool box>>spatial analyst tools>>surface>>reclassify or arc tool box>>3D analyst tools>> raster reclass
Saving layers	right click on layer>>save layer as
Saving maps	file>>save map

Slope	arc tool box>>spatial analyst tools>>surface>>slope or click on 3D analyst>>surface analysis>>slope
Aspect	arc tool box>>spatial analyst tools>>surface>>aspect or click on 3D analyst>>surface analysis>>aspect
Contour lines	arc tool box>>spatial analyst tools>>surface>>contour or click on 3D analyst>>surface analysis>>contour
Interpolation	arc tool box>>spatial analyst tools>>surface>>kringing
Clipping an image	arc tool box>>analysis tools>>extract>>clip
Intersecting two items	arc tool box>>analysis tools>>overlay>>intersect
Union of Two items	arc tool box>>analysis tools>>overlay>>union
Buffering	arc tool box>>analysis tools>>proximity>>buffer
Selecting a feature	click on the select feature tool>>then click on feature
Identifying a feature	click on the identify feature tool>>them click on feature
Creating Topographic profiles	click on 3D analyst>>surface analysis>>contour then right click on interpolate line tool, draw line click on profile graph to open cross section
Exporting tables	file>>right click>>attribute table>>export>>text file when opening in excel you must change the comma to a column for file to be read
Exporting cross sections	right click on line>>right click on profile>>export>>save as a jpeg
Adding fields to attribute tables	file>>right click>>attribute table>>options>>add field
Adding tools	file>>right click>>attribute table>>right click on field calculator>>left click load>>tool

ArcCatalog 9.2

Application	Source
Creating a geodatabase	right click on contents>>new>>personal geodatabase>>double click to open
Creating feature	right click on contents>>new>>feature data set data set
Creating feature class	right click on contents>>new>>feature class
Exporting tables	right click on layer>>attributes>>export

List of images addressed in this project.

CTX

P02_001844_1738_XN_06S214W-
P02_001857_1750_XN_05S209W-
P02_001989_1756_XN_04S213W-
P03_002112_2208_XN_40N337W-
P03_002138_2194_XN_39N327W-
P04_002635_1727_XN_07S210W-
P05_002886_1798_XN_00S223W-
P05_002913_1859_XN_05N241W-
P06_003310_2082_XI_28N282W-
P06_003479_1745_XN_05S212W-
P07_003624_1726_XN_07S210W-
P07_003704_1825_XN_02N235W-
P07_003835_1736_XN_06S211W-
P08_004218_1748_XI_05S227W-
P10_005062_1794_XN_00S230W-
P11_005247_1885_XN_08N242W-
P11_005378_1755_XN_04S217W-
P11_005407_2129_XN_32N293W-
P11_005460_2151_XI_35N300W-
P12_005697_2134_XI_33N291W-
P13_005946_1888_XN_08N245W-
P13_006160_2252_XN_45N334W-
P13_006198_2095_XN_29N289W-
P13_006223_1919_XN_11N249W-
P13_006238_2219_XN_41N303W-
P13_006252_2208_XN_40N325W-
P13_006264_2147_XN_34N292W-
P13_006278_2246_XN_44N315W-
P13_006288_1785_XN_01S222W-
P13_006290_2056_XN_25N280W-
P14_006473_1823_XI_02N234W-
P14_006582_2214_XN_41N335W-
P14_006635_2267_XN_46N343W-
P14_006660_2233_XN_43N305W-
P15_006713_2212_XN_41N312W-
P15_006724_1908_XN_10N248W-
P15_006737_1901_XN_10N243W-
P15_006858_2226_XN_42N311W-
P15_006925_2229_XN_42N340W-
P15_006961_1823_XN_02N238W-
P15_006989_2137_XN_33N287W-
P02_001831_1768_XN_03S220W
P02_001847_2152_XN_35N302W
P02_001923_1746_XN_05S211W
P03_002032_2220_XN_42N313W
P03_002135_1861_XN_06N241W
P03_002345_1759_XI_04S213W
P04_002717_2128_XN_32N293W
P05_002899_1759_XI_04S218W
P05_002925_1730_XN_07S207W
P06_003466_1757_XI_04S217W
P07_003585_1772_XN_02S226W
P07_003651_1763_XN_03S228W
P07_003769_1742_XN_05S209W
P08_003980_1727_XI_07S210W
P09_004693_1820_XN_02N236W
P10_005115_1821_XN_02N237W
P11_005273_1814_XN_01N231W
P11_005392_1879_XN_07N240W
P11_005420_2108_XI_30N287W
P12_005615_1742_XI_05S207W
P12_005787_1779_XN_02S223W
P13_006157_1906_XN_10N247W
P13_006185_2116_XN_31N294W
P13_006199_2245_XN_44N318W
P13_006236_1892_XN_09N244W
P13_006249_1841_XN_04N238W
P13_006262_1824_XN_02N233W
P13_006265_2271_XN_47N321W
P13_006279_2234_XN_43N342W
P13_006289_1919_XN_11N251W
P14_006460_1859_XN_05N239W
P14_006475_2149_XN_34N293W
P14_006595_2269_XN_46N331W
P14_006658_1895_XN_09N246W
P14_006699_2135_XN_33N288W
P15_006714_2256_XI_45N340W
P15_006726_2245_XN_44N307W
P15_006806_2202_XN_40N330W
P15_006885_2269_XN_46N329W
P15_006937_2222_XN_42N308W
P15_006974_1862_XN_06N233W

P15_007003_2246_XN_44N310W-
P15_007002_2107_XN_30N281W
P15_007040_1818_XI_01N234W-
P15_007082_2245_XN_44N308W
P16_007132_1766_XN_03S226W-
P16_007145_1783_XN_01S221W
P16_007161_2209_XN_40N304W-
P16_007162_2263_XN_46N332W
P16_007174_2154_XN_35N299W-
P16_007198_1805_XN_00N229W
P16_007201_2257_XN_45N316W-
P16_007213_2065_XN_26N282W
P16_007214_2257_XN_45N312W-
P16_007215_2254_XN_45N339W
P16_007359_2220_XN_42N311W-
P16_007360_2244_XN_44N338W
P16_007372_2232_XN_43N306W-
P16_007383_1897_XN_09N242W
P16_007385_2149_XN_34N300W-
P16_007396_1826_XN_02N236W
P16_007398_2166_XN_36N295W-
P16_007425_2220_XN_42N313W
P16_007426_2266_XN_46N341W-
P16_007464_2124_XN_32N296W
P17_007490_2095_XN_29N286W-
P17_007514_1755_XN_04S217W
P17_007530_2149_XN_34N299W-
P17_007541_1822_XN_02N235W
P17_007543_2162_XN_36N294W-
P17_007569_2143_XN_34N284W
P17_007557_2256_XN_45N318W-
P17_007581_1911_XN_11N248W
P17_007571_2200_XN_40N340W-
P17_007593_1739_XN_06S214W
P17_007583_2216_XN_41N307W-
P17_007676_2208_XN_40N327W
P17_007623_2271_XI_47N320W-
P17_007701_2091_XN_29N287W
P17_007689_2259_XI_45N322W-
P17_007715_2232_XN_43N312W
P17_007702_2245_XN_44N317W-
P17_007725_1765_XN_03S219W
P17_007716_2203_XN_40N339W-
P17_007729_2250_XN_45N334W
P17_007728_2207_XN_40N306W-
P17_007742_2239_XI_43N329W
P17_007738_1759_XN_04S214W-
P17_007752_1832_XN_03N237W
P17_007751_1710_XN_09S209W-
P17_007781_2256_XN_45N314W
P17_007755_2249_XN_44N324W-
P17_007808_2210_XN_41N331W
P17_007782_2219_XN_41N341W-
P17_007861_2192_XN_39N338W
P17_007831_1787_XI_01S233W-
P18_007900_2237_XN_43N324W
P17_007873_2242_XN_44N306W-
P18_007913_2244_XN_44N319W
P18_007912_2142_XN_34N290W-
P18_008068_1757_XN_04S225W
P18_007979_2264_XN_46N321W-
P18_008173_1736_XI_06S211W
P18_008085_2256_XN_45N335W-
P19_008266_1793_XI_00S232W
P18_008243_2219_XI_41N329W-
P19_008309_2265_XI_46N332W
P19_008292_1746_XI_05S220W-
P19_008533_2261_XI_46N330W
P19_008441_2247_XN_44N337W-
P19_008545_2123_XI_32N295W
P19_008542_1710_XN_09S208W-
P20_008714_1791_XN_00S226W
P19_008573_2263_XI_46N342W-
P20_008743_2173_XN_37N303W
P20_008731_2218_XN_41N336W-
P20_008912_1821_XN_02N233W
P20_008902_2209_XN_40N325W-
P21_009281_1762_XN_03S227W
P21_009087_2196_XN_39N336W-
P22_009611_1823_XN_02N237W
P22_009584_1746_XI_05S220W-
P22_009652_2099_XN_29N280W
P22_009639_2114_XN_31N285W-
P22_009799_2205_XN_40N336W
P22_009653_2224_XN_42N309W-

CRISM

FRT0000AA76_07_IF167L_IRA1
FRT0000AA76_07_IF167S_TRU1
FRT0000A81C_07_IF167L_IRA1
FRT0000A81C_07_IF167S_TRU1
FRT0000AD27_07_IF167L_IRA1
FRT0000AD27_07_IF167L_MAF1
FRT0000AD27_07_IF167S_TRU1
FRT0000BCE2_07_IF166L_IRA1
FRT0000BCE2_07_IF166L_PHY1
FRT0000BCE2_07_IF166S_TRU1
FRT00009A07_07_IF167L_IRA1
FRT00009A07_07_IF167S_TRU1
FRT000099C1_07_IF167L_IRA1
FRT000099C1_07_IF167S_TRU1
HRL0000B1B8_07_IF184L_IRA1
HRL0000B1B8_07_IF184S_TRU1
FRT0000A0D8_07_IF164L_MAF1
FRT0000A0D8_07_IF164S_TRU1
FRT0000A10D_07_IF165L_MAF1
FRT0000A10D_07_IF165S_TRU1
FRT0000A26C_07_IF167L_MAF1
FRT0000A26C_07_IF167S_TRU1
FRT0000A53E_07_IF165L_MAF1
FRT0000A53E_07_IF165S_TRU1
FRT0000A230_07_IF167L_MAF1
FRT0000A230_07_IF167S_TRU1
FRT0000AD16_07_IF165L_MAF1
FRT0000AD16_07_IF165S_TRU1
FRT0000B2BE_07_IF165L_MAF1
FRT0000B2BE_07_IF165S_FEM1
FRT0000B2BE_07_IF165S_TRU1
FRT00005DBD_07_IF166L_HYD1
FRT00005DBD_07_IF166L_PHY1
FRT00005DBD_07_IF166S_FEM1
FRT00005DBD_07_IF166S_TRU1
FRT00007FCC_07_IF164L_MAF1
FRT00007FCC_07_IF164S_TRU1
FRT00009B3D_07_IF165L_MAF1
FRT00009B3D_07_IF165S_TRU1
FRT00009BF7_07_IF166L_MAF1
FRT00009BF7_07_IF166S_TRU1
FRT00009DA4_07_IF167L_MAF1
FRT00009DA4_07_IF167S_TRU1
FRT00009DD6_07_IF165L_MAF1
FRT00009DD6_07_IF165S_TRU1
FRT00009DEC_07_IF167L_MAF1
FRT00009DEC_07_IF167S_TRU1
FRT000049FF_07_IF167L_MAF1
FRT000049FF_07_IF167S_FEM1
FRT000049FF_07_IF167S_TRU1
FRT000060A3_07_IF164L_MAF1
FRT000060A3_07_IF164S_TRU1
FRT000063A8_07_IF165L_MAF1
FRT000063A8_07_IF165S_FEM1
FRT000063A8_07_IF165S_TRU1
FRT000080ED_07_IF165L_MAF1
FRT000080ED_07_IF165S_TRU1
FRT0000887C_07_IF167L_MAF1
FRT0000887C_07_IF167S_TRU1
FRT0000952C_07_IF165L_MAF1
FRT0000952C_07_IF165S_TRU1
FRT00005840_07_IF165L_MAF1
FRT00005840_07_IF165S_TRU1
FRT00005905_07_IF165L_MAF1
FRT00005905_07_IF165S_TRU1
FRT00008986_07_IF167L_HYD1
FRT00008986_07_IF167L_MAF1
FRT00008986_07_IF167S_FEM1
FRT00008986_07_IF167S_TRU1
FRT00009213_07_IF167L_MAF1
FRT00009213_07_IF167S_TRU1
FRT00009486_07_IF167L_MAF1
FRT00009486_07_IF167S_TRU1
FRT00009605_07_IF167L_MAF1
FRT00009605_07_IF167S_TRU1
FRT00009652_07_IF165L_MAF1
HRL0000AC07_07_IF183S_FEM1
HRL0000AC07_07_IF183L_PHY1
HRL0000AC07_07_IF183L_MAF1
HRL0000AC07_07_IF183L_HYD1
HRL0000A8EC_07_IF183S_TRU1
HRL0000A8EC_07_IF183S_FEM1
HRL0000A8EC_07_IF183L_PHY1
HRL0000A8EC_07_IF183L_MAF1
HRL0000A8EC_07_IF183L_HYD1
HRL0000A5EA_07_IF184S_TRU1
HRL0000A5EA_07_IF184L_MAF1
FRT00009652_07_IF165S_TRU1

HRL0000AC07_07_IF183S_TRU1
HRL0000B29B_07_IF184S_TRU1
HRL0000BEF4_07_IF184S_TRU1
HRL00009C2A_07_IF182L_MAF1
HRL00002852_07_IF183L_MAF1
HRL00006408_07_IF183L_HYD1
HRL00006408_07_IF183L_PHY1
HRL00006408_07_IF183S_TRU1
HRS0000AC76_07_IF174S_TRU1
HRS00004A28_07_IF174S_TRU1
HRS00004130_07_IF176S_TRU1
HRL0000BF50_07_IF185S_TRU1
HRS0000AB71_07_IF176L_IRA1
HRS0000AB6E_07_IF176S_TRU1
HRS00004130_07_IF176S_TRU1
HRL0000B29B_07_IF184L_MAF1
HRL0000BEF4_07_IF184L_MAF1
HRL00009BC1_07_IF181S_TRU1
HRL00009C2A_07_IF182S_TRU1
HRL00002852_07_IF183S_TRU1
HRL00006408_07_IF183L_MAF1
HRL00006408_07_IF183S_FEM1
HRS0000AC76_07_IF174L_MAF1
HRS00004A28_07_IF174L_MAF1
HRS00004130_07_IF176L_MAF1
HRL0000BF50_07_IF185L_IRA1
HRS0000AB71_07_IF176S_TRU1
HRS0000AB6E_07_IF176L_IRA1
HRS00004130_07_IF176L_IRA1

MOC

E0400822
E0102224
E0300614
E0500922
E0600246
E1000302
E1100381
E1103584
E1200557
E1201645
E1401008
E1900085
M0803907
R1701197
S0901040
S1402845
E0400822
E1000765
E1600085
R0901181
S0301332
E0101704
E0200611
E0400806
E0503373
E1000163
E1004234
E1103458
E1104301
E1201400
E1400813
E1501662
E1900278
R0502519
S0200044
S1201657
S1500446
E0902578
E1100398
E1800777
R1301892
S1901131

HiRISE

PSP_007424_2080_RED_abrowse	PSP_003694_2205_RED_abrowse
PSP_005738_2245_RED_abrowse	PSP_005857_2225_RED_abrowse
PSP_006147_2250_RED_abrowse	PSP_007096_2215_RED_abrowse
PSP_007215_2255_RED_abrowse	PSP_007360_2245_RED_abrowse
PSP_007834_2250_RED_abrowse	PSP_008598_2155_RED_thumb
PSP_009733_2240_RED_abrowse	PSP_001570_2215_RED_thumb
PSP_005737_2185_RED_abrowse	PSP_005843_2260_RED_abrowse
PSP_006251_2125_RED_abrowse	PSP_007082_2245_RED_abrowse
PSP_007451_2225_RED_abrowse	PSP_007531_2195_RED_abrowse
PSP_007781_2255_RED_abrowse	PSP_008190_2255_RED_abrowse
PSP_008611_2125_RED_abrowse	PSP_008810_2225_RED_abrowse
PSP_009020_2210_RED_abrowse	PSP_009363_2240_RED_abrowse
PSP_009455_2215_RED_abrowse	PSP_009719_2230_RED_abrowse